



MINISTÉRIO DA CIÊNCIA, TECNOLOGIA, INOVAÇÕES E COMUNICAÇÕES
INSTITUTO NACIONAL DE PESQUISAS ESPACIAIS

sid.inpe.br/mtc-m21b/2017/01.25.17.13-TDI

**SIMULATION AND EXPERIMENTAL
CHARACTERIZATION OF GYROMAGNETIC
NONLINEAR TRANSMISSION LINES FOR
PROSPECTIVE AEROSPACE APPLICATIONS**

Fernanda Sayuri Yamasaki

Doctorate Thesis of the Graduate
Course in Engineering and
Management of Space System,
guided by Drs. José Osvaldo Rossi,
Joaquim José Barroso de Castro
and Edl Schamiloglu, approved in
February 16, 2017.

URL of the original document:
[<http://urlib.net/8JMKD3MGP3W34P/3N92GBH>](http://urlib.net/8JMKD3MGP3W34P/3N92GBH)

INPE
São José dos Campos
2017

PUBLISHED BY:

Instituto Nacional de Pesquisas Espaciais - INPE
Gabinete do Diretor (GB)
Serviço de Informação e Documentação (SID)
Caixa Postal 515 - CEP 12.245-970
São José dos Campos - SP - Brasil
Tel.:(012) 3208-6923/6921
Fax: (012) 3208-6919
E-mail: pubtc@inpe.br

**COMMISSION OF BOARD OF PUBLISHING AND PRESERVATION
OF INPE INTELLECTUAL PRODUCTION (DE/DIR-544):**

Chairperson:

Maria do Carmo de Andrade Nono - Conselho de Pós-Graduação (CPG)

Members:

Dr. Plínio Carlos Alvalá - Centro de Ciência do Sistema Terrestre (CST)

Dr. André de Castro Milone - Coordenação de Ciências Espaciais e Atmosféricas (CEA)

Dra. Carina de Barros Melo - Coordenação de Laboratórios Associados (CTE)

Dr. Evandro Marconi Rocco - Coordenação de Engenharia e Tecnologia Espacial (ETE)

Dr. Hermann Johann Heinrich Kux - Coordenação de Observação da Terra (OBT)

Dr. Marley Cavalcante de Lima Moscati - Centro de Previsão de Tempo e Estudos Climáticos (CPT)

Silvia Castro Marcelino - Serviço de Informação e Documentação (SID) **DIGITAL LIBRARY:**

Dr. Gerald Jean Francis Banon

Clayton Martins Pereira - Serviço de Informação e Documentação (SID)

DOCUMENT REVIEW:

Simone Angélica Del Ducca Barbedo - Serviço de Informação e Documentação (SID)

Yolanda Ribeiro da Silva Souza - Serviço de Informação e Documentação (SID)

ELECTRONIC EDITING:

Marcelo de Castro Pazos - Serviço de Informação e Documentação (SID)

André Luis Dias Fernandes - Serviço de Informação e Documentação (SID)



MINISTÉRIO DA CIÊNCIA, TECNOLOGIA, INOVAÇÕES E COMUNICAÇÕES
INSTITUTO NACIONAL DE PESQUISAS ESPACIAIS

sid.inpe.br/mtc-m21b/2017/01.25.17.13-TDI

**SIMULATION AND EXPERIMENTAL
CHARACTERIZATION OF GYROMAGNETIC
NONLINEAR TRANSMISSION LINES FOR
PROSPECTIVE AEROSPACE APPLICATIONS**

Fernanda Sayuri Yamasaki

Doctorate Thesis of the Graduate
Course in Engineering and
Management of Space System,
guided by Drs. José Osvaldo Rossi,
Joaquim José Barroso de Castro
and Edl Schamiloglu, approved in
February 16, 2017.

URL of the original document:
[<http://urlib.net/8JMKD3MGP3W34P/3N92GBH>](http://urlib.net/8JMKD3MGP3W34P/3N92GBH)

INPE
São José dos Campos
2017

Cataloging in Publication Data

Yamasaki, Fernanda Sayuri.

Ya14s Simulation and experimental characterization of gyromagnetic nonlinear transmission lines for prospective aerospace applications / Fernanda Sayuri Yamasaki. – São José dos Campos : INPE, 2017.

xxxii + 164 p. ; (sid.inpe.br/mtc-m21b/2017/01.25.17.13-TDI)

Thesis (Doctorate in Engineering and Management of Space System) – Instituto Nacional de Pesquisas Espaciais, São José dos Campos, 2017.

Guiding : Drs. José Osvaldo Rossi, Joaquim José Barroso de Castro and Edl Schamiloglu.

1. Gyromagnetic lines. 2. Ferrite. 3. NLTL. 4. RF generation.
5. Space applications. I.Title.

CDU 621.3.052:629.78



Esta obra foi licenciada sob uma Licença Creative Commons Atribuição-NãoComercial 3.0 Não Adaptada.

This work is licensed under a Creative Commons Attribution-NonCommercial 3.0 Unported License.

Aluno (a): **Fernanda Sayuri Yamasaki**

Título: "SIMULATION AND EXPERIMENTAL CHARACTERIZATION OF GYROMAGNETIC
NONLINEAR TRANSMISSION LINES FOR PROSPECTIVE AEROSPACE
APPLICATIONS".

Aprovado (a) pela Banca Examinadora
em cumprimento ao requisito exigido para
obtenção do Título de **Doutor(a)** em
Engenharia e Tecnologia Espaciais/Eng.
Gerenc. de Sistemas Espaciais

Dr. **Walter Abrahão dos Santos**


Presidente / INPE / São José dos Campos - SP

Dr. **José Osvaldo Rossi**


Orientador(a) / INPE / São José dos Campos - SP

Dr. **Joaquim José Barroso de Castro**


Orientador(a) / INPE / SJCampos - SP

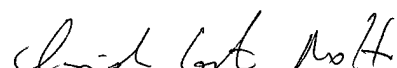
Dr. **Edl Schamiloglu**


Orientador(a) / Univ. of New Mexico / México - EUA

Dra. **Elizete Gonçalves Lopes Rangel**


Membro da Banca / INPE / São José dos Campos - SP

Dr. **Cláudio Costa Motta**


Convidado(a) / USP / São Paulo - SP

Dr. **André Franceschi de Angelis**


Convidado(a) / UNICAMP / Limeira - SP

Este trabalho foi aprovado por:

maioria simples

unanimidade

“Adversa effectus eliciendi talenta latuisset quiescit in rebus prosperis.”
Horace

(Adversity has the effect of eliciting talents, which in prosperous circumstances would have lain dormant.)

This thesis is dedicated to my parents Rosângela de Azevedo Pinto Yamasaki and Vicente Yosihara Yamasaki, my biggest supporters, my inspiration and safe place.

ACKNOWLEDGEMENTS

To my mother Rosângela for pushing me in all aspects of my life and teaching me that what I don't know, I can learn. You are my biggest example of strength and persistence. To my father, Vicente for caring so much. Your demonstration of protection makes me feel safe. Both of you are the necessary opposites in my life, the perfect balance to move on.

To my supervisor, Professor Dr. Jose Osvaldo Rossi for the seven years of teaching, dedication, professionalism and patience. I will always be grateful for your encouragement and confidence deposited that contributed decisively for the accomplishment of this thesis.

To my supervisor, Professor Dr. Joaquim Jose Barroso de Castro for his great detailed technical contribution to this work, as well as for his time spent on reviewing the material for publications.

To my supervisor, Professor Dr. Edl Schamiloglu for the great opportunity given by him to work as an international visitor student at UNM, for his contribution on this thesis and also his time spent on reviewing my English.

To my closest friends, for understanding my absence on several occasions during all these years and for always being by my side when needed.

To my colleagues from INPE, for the coffee breaks and so many talks, which are essential and needed when sharing the office. I special would like to thank Carla, Samantha and Lauro for the advices and contribution to the work related to this thesis.

To the staff from the laboratory workshop, in special to Paulo, for the care and quality of the mechanical devices built for my experimental work.

To the Coordination for the Improvement of Higher Education Personnel (CAPES) for the scholarship provided to support my 6-month stay as an international student visitor at the University of New Mexico, Albuquerque, NM, USA as part of my doctorate program.

To the National Counsel of Technological and Scientific Development (CNPQ) for the scholarship to support my 4-year doctorate program developed at LAP/INPE.

To the Southern Office of Aerospace Research and Development (SOARD) for funding our research program under the last contract nº FA9550-14-1-0133.

To the National Institute of Space Research (INPE) and the Associated Plasma Laboratory (LAP) for their financial support, equipment and facilities given for the development of this doctorate program.

Finally, my sincere thanks to all who contributed in some way to make this work possible.

ABSTRACT

A great interest has been devoted to the study of nonlinear transmission lines (NLTLs) for radiofrequency (RF) generation since they have been used with great success in RF generation by producing a train of oscillatory waves along the line and at its output. There are two configurations of NLTLs. The first one is a dispersive line consisting of LC sections with nonlinear components, and the second one is a continuous ferrite loaded non-dispersive line generally biased by an axial magnetic field, known as gyromagnetic line. In this thesis, the focus of the study is on the second one, since gyromagnetic lines can operate in a broader frequency range (0.4 up to 2.0 GHz) with higher conversion efficiency (20.0 %) when compared to lumped NLTLs limited up to 300.0 MHz with less than 10.0 % of efficiency, because of their dielectric losses and stray impedances on line structure. Different models have been used along the years by several authors with different approaches to study the gyromagnetic phenomenon by means of numerical simulations based on analytical models to predict the precession movement of the electron magnetic dipole of the ferrimagnetic material. Thus, the goal of this thesis is to analyze the gyromagnetic NLTL behavior through the effects on the line operation by changing its parameters. The novelty herein is to use Spice simulations based on LC lumped line models to study continuous gyromagnetic NLTLs in addition to numerical simulations usually employed, focusing on the pulse rise time compression and RF generation caused by magnetic dipole precession. Different models are studied by comparing Spice simulations with corresponding results from numerical simulations and experiments found in the literature. Finally, an experimental set-up is described for a 20-cm gyromagnetic line loaded with NiZn ferrite beads to validate with data the proposed method based on Spice simulations. Finally, it is expected that such Spice techniques can be used in the design of these continuous lines for RF applications in space and mobile defense platforms of compact size.

Keywords: Gyromagnetic lines. Ferrite. NLTL. RF generation. Space applications.

SIMULAÇÃO E CARACTERIZAÇÃO EXPERIMENTAL DE LINHAS DE TRANSMISSÃO NÃO LINEARES GIROMAGNÉTICAS PARA PROSPECTIVA APLICAÇÃO AEROESPACIAL

RESUMO

Um grande interesse tem sido dedicado ao estudo de Linhas de Transmissão Não Lineares (LTNLs) para geração de radiofrequência (RF), uma vez que têm sido utilizadas com grande sucesso na geração de RF produzindo um trem de ondas oscilatórias ao longo da linha e em sua saída. Existem duas configurações de LTNLs, a primeira é uma linha dispersiva constituída por seções LC com componentes não lineares, e a segunda é uma linha não dispersiva e contínua, utilizando ferritas geralmente polarizadas por um campo magnético axial, conhecida como giromagnética. Nesta tese, o foco do estudo é na segunda linha, uma vez que ela pode operar em uma faixa de frequência mais ampla (0,4 a 2,0 GHz) com maior eficiência de conversão (20,0 %) quando comparada a LTNLs discreta que é limitada a 300,0 MHz com menos de 10,0 % de eficiência, por causa de suas perdas dielétricas e impedâncias parasitas na estrutura da linha. Diferentes modelos têm sido utilizados ao longo dos anos por vários autores com diferentes abordagens para estudar o fenômeno giromagnético por meio de simulações numéricas baseadas em modelos analíticos para prever o movimento de precessão. Assim, o objetivo desta tese é analisar o comportamento de LTNLs giromagnéticas através dos efeitos na operação da linha mudando seus parâmetros. A novidade aqui é usar simulações Spice com base em modelos de linha LC para estudar as linhas giromagnéticas contínuas, além de simulações numéricas normalmente empregadas, com foco na compressão do tempo de subida de pulso e geração de RF causada pela precessão do campo magnético. Diferentes modelos são estudados comparando-se simulações Spice com resultados correspondentes de simulações numéricas e com experimentos encontrados na literatura. Finalmente, um arranjo experimental para uma linha giromagnética de 20,0 cm usando contas de ferrita NiZn foi implementado para validar com dados experimentais o método proposto baseado em simulações Spice. Finalmente, espera-se que tais técnicas de simulação Spice possam ser usadas na conceção destas linhas contínuas para aplicações de RF no espaço e em plataformas móveis de defesa de tamanho compacto.

Palavras chave: Linhas giromagnéticas. Ferrita. LTNL. Geração de RF. Aplicações Espaciais.

LIST OF FIGURES

| | Page |
|---------------------------------------------------------------------------------------------------------------------------------------------------------------------------------------------------------------------------|------|
| Figure 3.1. Gyromagnetic line output signals showing better performance between 0 and 100°C..... | 10 |
| Figure 3.2. Bragg's frequency response to different temperatures..... | 10 |
| Figure 3.3. Traveling wave Tube a) Inner/structure view b) Outside view. | 16 |
| Figure 3.4. Input pulse and output waveform on a dispersive NLTL..... | 18 |
| Figure 3.5. The different possible settings for the discrete nonlinear LC line a) Capacitive line for low voltage operation, b) Capacitive line for high voltage operation, c) Inductive line, d) Hybrid line. | 19 |
| Figure 3.6. Compression of the output pulse in a NLTL. | 21 |
| Figure 3.7. Soliton formation. | 22 |
| Figure 3.8. Solitons collision and conservation of the waves showing normalized amplitudes as function of position at given normalized times. | 24 |
| Figure 3.9. B-H curve of a magnetic material. | 26 |
| Figure 3.10. Types of bias a) azimuthal and b) axial. | 27 |
| Figure 3.11. Continuous line with magnetic material used for pulse compression. | 28 |
| Figure 3.12. Precession of the magnetic moment M in ferrites..... | 29 |
| Figure 3.13. Alignment of (a) Ferromagnetic and (b) Ferrimagnetic materials. 30 | 30 |
| Figure 3.14. Spin magnetic dipole moment and angular momentum vectors for a spinning electron. | 31 |
| Figure 3.15. The dynamics described by the LLG equation, in which the magnetization M precesses around H with damping. | 33 |

| | |
|----------------------------------------------------------------------------------------------------------------------------------------------------------------------|----|
| Figure 3.16. Propagating front showing the reverse transition region moving along the line..... | 40 |
| Figure 3.17. Equivalent circuit of the ferrite line proposed by Weiner..... | 40 |
| Figure 3.18. Gyromagnetic line showing the a) Ferrite bead shape used in the b) Coaxial Line. | 43 |
| Figure 3.19. Model used by Pouladian-Kari to simulate the pulse compression in gyromagnetic lines. | 46 |
| Figure 3.20. Complete Pouladian-Kari's model including the magnetic precession effect with constant magnetic bias. | 47 |
| Figure 3.21. Complete Pouladian-Kari and Shapland's model including the magnetic precession effect..... | 48 |
| Figure 3.22. Model proposed by Dolan for simulation of the gyromagnetic line. | 50 |
| Figure 3.23. Simulation of $L \times I$ curve of a nonlinear inductor using a) hyperbolic function and b) exponential function..... | 51 |
| Figure 3.24. Basic schematic for numerical analysis system..... | 52 |
| Figure 4.1. Ferrite beads | 61 |
| Figure 4.2. Construction steps of the coaxial line. a) copper wire inside the ferrite beads, b) insulating tape layer, c) solder wire layer, d) welded tin line..... | 62 |
| Figure 4.3. Expanded view of the coaxial line assembly with solenoid..... | 63 |
| Figure 4.4. Final steps of the expanded view of the coaxial line assembly with permanent magnets. | 63 |
| Figure 4.5. Teste set-up of gyromagnetic line (a) biases with permanent magnets (b) biased with a solenoid | 64 |
| Figure 4.6. Scheme employed to test the gyromagnetic line with axial and azimuthal bias. | 65 |

| | |
|----------------------------------------------------------------------------------------------------------------------------------------------------------------------------------------------------------------------------|----|
| Figure 4.7. Generator signal on a 50Ω load termination..... | 66 |
| Figure 5.1. LT-Spice schematic circuit used to reproduce Weiner's model | 68 |
| Figure 5.2. Experimental output voltage from the loaded ferrite line obtained from (a) Weiner's experiment varying azimuthal magnetic bias and (b) corresponding LTSpice simulations for several values of R_f ... | 69 |
| Figure 5.3. LT-Spice basic schematic circuit for Pouladian-Kari's model. | 71 |
| Figure 5.4. Comparison of Pouladian-Kari's results. | 72 |
| Figure 5.5. LT-Spice simulation results using Pouladian-Kari's model for 11.0 pF, 62.0 pF, 91.0 pF and 270.0 pF linear capacitors, respectively. | 74 |
| Figure 5.6. LT-Spice simulation results using Pouladian-Kari's model for resistive loads of 5.0Ω , 50.0Ω , $1.0 k\Omega$ and $50.0 k\Omega$ | 75 |
| Figure 5.7. LT-Spice simulation results using Pouladian-Kari's model for 10, 20, 30 and 40 sections | 76 |
| Figure 5.8. LT-Spice simulation results using Pouladian-Kari's model for saturation inductance of 0.8 nH, 0.5 nH, 0.2 nH and 0.1 nH, respectively. | 78 |
| Figure 5.9. LT-Spice simulation circuit model for a line with a linearly graded magnetic bias. | 80 |
| Figure 5.10. Constant and linearly graded bias a) Original b) Reproduced..... | 82 |
| Figure 5.11. Circuit basic scheme of LT-Spice for Dolan's model. | 83 |
| Figure 5.12. Response of Dolan's model a) Original b) Reproduced | 84 |
| Figure 5.13. Output Fast Fourier Transform from simulated Dolan's model.... | 84 |
| Figure 5.14. Dolan's results reproduced a) Numerical analysis model using Mathematica software, and b) Circuit simulation model using LT- Spice. | 85 |
| Figure 5.15. LT-Spice simulation schematic with reactive load. | 86 |

| | |
|-------------------------------------------------------------------------------------------------------------------------------------------------------------------------------------|-----|
| Figure 5.16. Input and output of the model with reactive load. | 87 |
| Figure 5.17. Output pulse FFT of the simulation with reactive load..... | 88 |
| Figure 5.18. Simulation schematic with resistive load. | 88 |
| Figure 5.19. Input and output of the model with resistive load..... | 89 |
| Figure 5.20. Output pulse FFT of the simulation with resistive load. | 90 |
| Figure 5.21. Assembly for coaxial line characterization (a) Case 1: Azimuthal bias, (b) Case 2: Bias with magnets, and (c) Case 3: Axial bias. ... | 92 |
| Figure 5.22. L x I curves for (a) Case 1: Azimuthal bias, (b) Case 2: Bias with magnets, and (c) Case 3: Axial bias. | 94 |
| Figure 5.23. Input and output of the coaxial line without magnets. | 95 |
| Figure 5.24. Several magnets placed along the coaxial line (on top). | 96 |
| Figure 5.25. Input and output pulse using permanent magnets as external bias. | 96 |
| Figure 5.26. Spice scheme used to simulate the gyromagnetic line with magnets..... | 97 |
| Figure 5.27. Comparison between experimental result using magnets and Spice circuit model. | 98 |
| Figure 5.28. Experimental assembly with axial and azimuthal bias for low voltage operation..... | 99 |
| Figure 5.29. Experimental results of the line with axial and azimuthal biases at low voltage operation (a) Input pulse, (b) output pulse and (c) both pulses on shorter scale. | 100 |
| Figure 5.30. Output FFT spectrum of the NLTL at low voltage operation. | 101 |
| Figure 5.31. Different configurations of magnetic biasing showing four possible combinations for directions of the axial field H_0 and bias current I_0 | 102 |

| | |
|-------------------------------------------------------------------------------------------------------|-----|
| Figure 5.32. Output pulse of the NLTL operating at low voltage in four different configurations | 103 |
| Figure 5.33. Line output pulse with axial and azimuthal bias at high voltage operation. | 105 |
| Figure 5.34. FFT spectrum of the output pulse for line operation at high voltage. | 106 |

LIST OF TABLES

| | Page |
|-----------------------------------------------------------------------------------------------------------------------------------------------------------------------------------|-------------|
| Table 2.1. Summary of the models used in this thesis. | 6 |
| Table 3.1. Frequency range for satellite application [24]. | 13 |
| Table 3.2. Frequency spectrum classification..... | 14 |
| Table 3.3. Comparison of LC lumped dielectric and gyromagnetic lines. | 55 |
| Table 3.4. Recent publications on Gyromagnetic Nonlinear Transmission Lines | 57 |
| Table 5.1. Main parameters of Weiner's model. | 68 |
| Table 5.2. Main parameters of Pouladian's basic model. | 71 |
| Table 5.3. Basic values for the varying parameters of Pouladian-Kari's model | 73 |
| Table 5.4. Comparison between the varying parameters | 79 |
| Table 5.5. Main parameters of Pouladian / Shapland's model. | 81 |
| Table 5.6. Main parameters of Dolan's model. | 83 |
| Table 5.7. Values of the inductance varying according to the applied current for (a) Case 1: Azimuthal bias, (b) Case 2: Bias with magnets, and (c) Case 3: Axial bias..... | 93 |
| Table 5.8. Axial and azimuthal biases at low voltage operation. | 100 |
| Table C.1. Summary of the works published and presented at conferences during the development of this thesis. | 153 |

LIST OF ABBREVIATIONS

| | |
|-------|-----------------------------------------|
| NLTL | Nonlinear Transmission Lines |
| NLETL | Nonlinear Electrical Transmission Line |
| RF | Radiofrequency |
| LLG | Landau-Lifshitz-Gilbert |
| LL | Landau-Lifshitz |
| MKS | Meter-Kilogram-Second |
| LC | Inductor-Capacitor |
| RLC | Resistor-Inductor-Capacitor |
| R | Resistor |
| L | Inductor |
| C | Capacitor |
| PFN | Pulse Forming Network |
| NLIL | Nonlinear Inductive Line |
| VMD | Voltage Modulation Depth |
| TWT | Traveling wave tubes |
| ITU | International Telecommunication Union |
| MSS | Mobile Satellite Service |
| UHF | Ultra-High Frequency |
| SHF | Super High Frequency |
| EHF | Extremely High Frequency |
| DARS | Digital Audio Radio Service |
| FSS | Fixed Satellite Service |
| BSS | Broadcast Satellite Service |
| LMDS | Local Multichannel Distribution Service |
| ISL | Intersatellite links |
| HPM | High power microwave |
| PRF | Pulse repetition frequency |
| SAR | Synthetic Aperture Radar |

LIST OF SYMBOLS

| | |
|------------|--------------------------------------|
| pF | Pico farad (10^{-12}) |
| mA | Mili ampere (10^{-3}) |
| L | Inductor value, henry (H) |
| C | Capacitor value, coulomb (C) |
| f_{c0} | Bragg cutoff frequency |
| V | Voltage, volt (V) |
| μ | Magnetic permeability |
| t_{ri} | Input rise time (ns) |
| t_{ro} | Output rise time (ns) |
| φ | Magnetic flux |
| B | Magnetic flux density |
| H | External axial magnetic field, henry |
| L_o | Initial Inductance (H) |
| L_f | Final Inductance (H) |
| I_s | Saturation Current (A) |
| GHz | Giga hertz |
| MHz | Mega hertz |
| MW | Megawatt |
| t | Time |
| kHz | Kilo hertz |
| F | Farad |
| nH | Nano henry |
| f | Frequency |
| Hz | Hertz |
| T | Period |
| GND | Ground |
| R_{gen} | Generator resistance (ohm) |
| R_{load} | Resistive load (ohm) |
| μH | Micro henry |
| Ω | Ohm |

| | |
|--------------|------------------------------------------------|
| $k\Omega$ | Kilo ohm |
| Z_0 | Line impedance (ohm) |
| Z | Output impedance (ohm) |
| \tanh | Hyperbolic tangent |
| kV | Kilo volts |
| DC | Direct Current |
| AC | Alternating current |
| ϵ | Electrical permittivity |
| ΔT | Rise time reduction |
| c | Speed of light in vacuum |
| L_{sat} | Saturated inductance of the coaxial line |
| M | Magnetic moment |
| I | Current Pulse |
| α | Damping factor |
| M_s | Saturation magnetizing |
| S | Switching constant |
| H_C | Coercive field |
| τ | Switching time |
| NiZn | Nickel-Zinc |
| μ_0 | Permeability of free space |
| b | Ferrite outer radius |
| a | Ferrite inner radius |
| l | Magnetic average path |
| R_f | Distributed resistance in the line |
| Δz | Length increase used to make the line discrete |
| l_c | Length of the coaxial line |
| n | Number of sections |
| ω | Oscillation frequency |
| MnZi | Manganese-Zinc |
| Oe | Oersted |
| t_{on} | Bandwidth |
| ϵ_0 | Permittivity of free space |

| | |
|----------|-------------------------------------------------------|
| di | Inner diameter of the coaxial conductor |
| do | Outer diameter of the coaxial conductor |
| RR | Resistance of the RLC branch |
| LR | Inductance of the RLC branch |
| CR | Capacitance of the RLC branch |
| V_{pt} | Oscillation amplitude between the peak and the valley |
| j | Number of cycles |

CONTENTS

| | Page |
|----------------------------------------------------|-------------|
| 1. INTRODUCTION | 1 |
| 2. OBJECTIVES..... | 5 |
| 3. THEORETICAL BACKGROUND | 7 |
| 3.1. Satellite Specifications | 7 |
| 3.1.2. Telecommunications Subsystem..... | 11 |
| 3.2. Radiofrequencies for Telecommunications | 12 |
| 3.2.1. Synthetic Aperture Radar | 14 |
| 3.3. Traveling Wave Tubes | 15 |
| 3.4. Nonlinear Transmission Lines..... | 16 |
| 3.4.1. Nonlinear Discrete LC lines | 17 |
| 3.4.1.1. Solitons | 23 |
| 3.4.2. Basic Concepts of Gyromagnetic Lines..... | 24 |
| 3.4.2.1. Types of Bias..... | 26 |
| 3.4.2.2. Basics of Ferrimagnetism..... | 29 |
| 3.4.2.3. LLG equation..... | 32 |
| 3.5. Models to be Studied | 38 |
| 3.5.1. Weiner's Model..... | 39 |
| 3.5.2. Pouladian-Kari et al.'s Model..... | 45 |
| 3.5.3. Pouladian-Kari / Shapland's Model | 47 |
| 3.5.4. Dolan's Model..... | 48 |
| 3.6. Spice Circuit Simulations | 50 |
| 3.7. Numerical Analysis | 52 |

| | | |
|----------|---------------------------------------------------------------------------------------------------------|-----|
| 3.8. | Advantages of using Gyromagnetics Lines | 54 |
| 3.9. | State of the Art..... | 55 |
| 4. | METHODOLOGY | 59 |
| 4.1. | Spice and Numerical Simulations | 59 |
| 4.2. | Line Design and Experimental Set-up..... | 61 |
| 5. | RESULTS AND DISCUSSIONS | 67 |
| 5.1. | Weiner's Results Reproduced..... | 67 |
| 5.2. | Pouladian-Kari et al.'s Results Reproduced..... | 70 |
| 5.2.1. | Basic Model..... | 70 |
| 5.2.1.1. | Case A: Varying the Capacitor Values | 73 |
| 5.2.1.2. | Case B: Varying the Load Resistance | 75 |
| 5.2.1.3. | Case C: Varying the Number of Sections | 76 |
| 5.2.1.4. | Case D: Varying the Saturation Inductance..... | 77 |
| 5.2.2. | Pouladian-Kari / Shapland's Results Reproduced..... | 80 |
| 5.3. | Dolan's Results Reproduced..... | 82 |
| 5.4. | Numerical Analysis | 85 |
| 5.5. | Our Proposal of a New Topology Based on a Reactive Load | 86 |
| 5.6. | Experimental Validation | 90 |
| 5.6.1. | Characterization of L x I Curves | 91 |
| 5.6.2. | Experimental Line Operation without Bias..... | 95 |
| 5.6.3. | Experimental Line Operation with Permanent Magnets | 95 |
| 5.6.4. | Experimental Line Tests with Axial and Azimuthal Bias at Low Voltage Operation | 98 |
| 5.6.4.1. | Different Configurations of Magnetic Biases for the Gyromagnetic NLTL at Low Voltage Operation | 102 |

| | |
|----------------------------------------------------------------------------------------|-----|
| 5.6.5. Experimental Line with Axial and Azimuthal Bias for High Voltage Operation..... | 104 |
| 6. CONCLUSIONS..... | 107 |
| 7. FUTURE WORK | 111 |
| REFERENCES..... | 113 |
| APPENDIX A: DEVELOPMENT OF EQUATIONS | 125 |
| A.1. Linear Capacitance | 125 |
| A.2. Relation between LLG and LL Equations..... | 126 |
| A.3. Formulation in Cartesian Coordinates..... | 128 |
| A.4. Calculation of the Parameters of Weiner's Model | 131 |
| A.5. Calculation of the Parameters of the Pouladian-Kari and Shapland's Model | 135 |
| A.6. Pouladian-Kari et al.'s Discrepancies..... | 138 |
| A.7. Calculation of the Precession Frequency at High Voltage Operation..... | 141 |
| APPENDIX B: MATHEMATICA CODE | 143 |
| APPENDIX C: PUBLISHED WORKS AND PARTICIPATION IN EVENTS | 149 |
| C.1. Journals | 149 |
| C.2. International Conferences..... | 150 |
| C.3. National Conferences | 152 |
| APPENDIX D: TEACHING INTERNSHIP..... | 155 |
| APPENDIX E: AWARD | 157 |
| APPENDIX F: SANDWICH PROGRAM | 159 |
| APPENDIX G: PROJECT SUPPORTERS | 161 |
| ANNEX A: MAIN DATASHEETS..... | 163 |
| A.1. Ferrite bead FB-43201 | 163 |

| | |
|------------------------|-----|
| A.2. Diode BYW56 | 164 |
|------------------------|-----|

1. INTRODUCTION

The cost of satellite launching has a direct relation with its weight (heavier, more expensive the effective cost), and consequently, the emerging of new technologies and materials used in satellite design supports the development of compact and more reliable materials, driving to more efficient and cheaper systems [1]. Nowadays, to establish communication between a satellite and a ground station, electronic tubes (such as Traveling Wave Tubes - TWTs) are used as final amplifiers in the communication link, with excellent results so far [2].

A great interest has been devoted to the study of Nonlinear Transmission Lines (NLTLs) for RF generation and radiation. The two well-known configurations of NLTLs are dispersive lines consisting of sections with nonlinear components, and a continuous non-dispersive line known as the gyromagnetic line. Both configurations have the same principle of operation based on the sharpening of the input pulse, related to the dielectric permittivity variation with voltage for discrete lines and the magnetic permeability dependence on current for the gyromagnetic lines.

The LC discrete lines and continuous non-dispersive lines are conceptually different. Gyromagnetic NLTLs can produce a very broad frequency spectrum, with RF conversion efficiency of about 20% starting from 400 MHz and exceeding frequencies of 2.0 GHz [3], [4], [5], [6] and [7] for potential applications in satellite communications, which require operating frequencies at least in the S-band range. On the other hand, nonlinear LC lines operate at lower frequencies around 1.0 GHz [8] in the case of inductive lines with saturated inductors, being even worse with ceramic dielectrics, which limit their application in frequencies up to 250-300 MHz [9], [10]. Although Seddon [8] has achieved efficiencies of the order of 20% with LC inductive lines at 1.0 GHz, surely the efficiency of capacitive LC lines is far less than 10% because of dielectric losses.

The focus of this thesis is on gyromagnetic lines since this line is capable of generating stronger pulse oscillations at higher frequencies than the discrete lines, in addition to having higher RF conversion efficiency. Another advantage of the gyromagnetic lines in relation to the dispersive dielectric NLTs is the stronger nonlinearity of the ferrite-based inductance when compared to the nonlinearity of the nonlinear ceramic capacitance or reverse-biased varactor diodes [11].

Katayev in 1966 [12] gave a basic mathematical description of the pulse sharpening effect on ferrite-loaded lines, and was the first to explain the phenomenon extensively. Later after Katayev's publication, Weiner in 1981 [13] published a paper describing a simplified theory of sharpening based on Katayev's explanations. In 1991, Pouladian-Kari et al. [14] used an inductive nonlinear discrete LC transmission line to model continuous gyromagnetic lines. Such a model was used to calculate the reduction on the rise time at the output of the line caused by the decrease of the ferrite magnetic permeability. Pouladian-Kari et al. [15] also developed a frequency-enhanced model and compared it with Katayev's [12] and Weiner's [13] to obtain an improved configuration for predicting the rise time compression on the output pulse in a loaded coaxial transmission line. The main difference between Weiner's [13] and Pouladian-Kari et al.'s [14], [15] models is that in the latter RLC branches are added in parallel with the line capacitance of the LC ladder network model to include the precession of the magnetic moment caused by the presence of the magnetic axial bias in this case. Dolan [16] pointed out that the model proposed by Pouladian-Kari et al. [14], [15] is incomplete, since the addition of RLC resonant branches does not include the direct representation of the magnetic precession of the ferrite and the values are selected arbitrarily, being an ad-hoc solution. So far, the best way to simulate these lines seems to be through the method proposed by Dolan [16] in 2000, since he used it to simulate the output response of a line with azimuthal and axial biases. In this model, the authors used an equivalent circuit based on elements of a discrete

LC transmission line in series with instantaneous voltage sources determined by the change in the magnetization flux of the ferrite. In this model, the sources represent the induced voltages along the line during the magnetization phase due to the change in the magnetic moment. Thus, Dolan's model is more complete, since it correctly takes into account the effect of ferrite magnetic precession caused by the presence of the axial bias.

This thesis explores and quantifies the characteristics of gyromagnetic NLTLs based on previous work, to achieve in the future a RF generation system of compact size, which will be also efficient and cheaper. For this, experimental analysis will be performed and compared with the circuit simulations for validation of the method and interpretation of the results, aiming at a new approach to model the gyromagnetic line. In summary, the models available in the literature study the gyromagnetic line by means of experimental results or numerical analysis, reinforcing the contribution of this thesis since, for the first time, a model for simulating gyromagnetic nonlinear transmission lines in the Spice platform is proposed. This technology also presents great prospects for space and defense applications (satellites, aircrafts, etc.).

2. OBJECTIVES

In this thesis, the study of gyromagnetic nonlinear transmission lines using simulations is proposed to verify the feasibility of the equivalent LC circuit models, in order to design and build an experimental line. The main contribution of this thesis is the simulation of this type of transmission line using LT-Spice simulation models for the first time.

The specific goals of the work proposed are given below:

- Spice and numerical simulations of the gyromagnetic NLTL based on the models proposed by Weiner [13], Pouladian-Kari [14], Pouladian-Kari/Shapland [15] and Dolan [16].
- The use for the first time of graphical interface programs in the Windows environment, such as LT-Spice that eases the circuit simulation of the equivalent models for the gyromagnetic line.
- Comparison of the simulation results obtained with those found in references [13], [14], [15] and [16], already mentioned.
- Determination of which computational method (numerical or Spice) is more efficient considering handling, accuracy, and simulation time.
- Evaluating which model better represents the magnetic precession phenomenon of ferrites, considering its effect on the output rise time and oscillation frequency.
- Validation of computer methods by comparison between experimental and simulation results when the gyromagnetic effect takes place.

A summary of the models used as the basis for comparing results and the method of validation of this thesis are shown in Table 2.1.

Table 2.1. Summary of the models used in this thesis.

| Reference | Author | Year | Contribution |
|------------------|------------------------|-------------|-------------------------------------------------------------------------------------------|
| [13] | Weiner | 1981 | Described a simplified theory of sharpening based on Katayev's explanations. |
| [14] | Pouladian | 1989 | RLC branches added in parallel with the capacitor to simulate the precession oscillation. |
| [15] | Pouladian/ Shapland | 1991 | RLC branches with varying values along the line (linearly graded bias). |
| [16] | Dolan | 2000 | Voltages sources in series with the linear inductor (axial bias). |

Source: Author's production.

It is expected that this thesis offers a suitable solution for simulating gyromagnetic lines using Spice software (LT) of easier manipulation to predict the operation device rather than numerical solution to differential equations of the electrical network.

3. THEORETICAL BACKGROUND

This chapter gives the principle of operation of NLTs and describes their main properties for applications in space systems. For this, satellite and its telecommunication subsystem will be discussed and, next, the radiofrequency spectrum and Traveling Wave Tubes (TWTs) will be presented. Nonlinear transmission lines are also presented showing the two types, the lumped LC and the gyromagnetic continuous lines. Circuit models will be analyzed and studied. In particular there will be explained the numerical analysis and spice model concepts, since both methods are used for validation of the results. Finally, the advantages of using gyromagnetic lines will be shown, to justify the focus of our research on this subject by ending with the state of the art of the main studies about gyromagnetic lines in recent years.

3.1. Satellite Specifications

The satellite is one of numerous devices designed with the purpose to explore space. These vehicles are designed considering their objective and the environment where they have to operate, that is, depending on their purpose their specifications will change completely from one mission to another. Spacecraft are conceptually divided into two parts: the payload and the platform, which includes the necessary parts to carry out the launching and to manage the payload operation [1].

The platform of artificial satellites is divided into several subsystems for the engineering design work, assembly and testing. Usually the subsystems are divided as [1], [17], [18], [19], [20], [21] and [22]:

- Attitude and orbit control: controls the pointing of the satellite in space;
- Power supply: provides the energy required for the subsystems;

- Telecommunication: sends and receives data allowing monitoring of the operation and the command of the satellite;
- Board management: processes the satellite internal data, the information received on Earth and sent to the ground stations;
- Structures and mechanisms: provide the mechanical and movement support for the parts of the satellite. They also offer protection against vibration during the launching and against radiation in orbit;
- Thermal control: keeps the equipment within its nominal range of temperature;
- Propulsion: provides the thrust needed to control the attitude and orbit of the satellite.

Some factors that affect the satellite specification should be considered such as [1], [17], [18], [19], [20], [21] and [22]:

- Size and weight: usually proportional to the requirements associated with the payload and life of the mission (mostly related to the fuel and electric power).
- Required power: proportional to the demand of the payload, being limited by weight and size;
- Data transfer rate: associated with the mission, being limited by the power processing, on-board data storage, and system capability of ground transmission;
- Communication systems: associated with the payload and mission, being limited by the availability of ground stations;
- Pointing: also associated with the payload and mission, being limited by cost and mass;

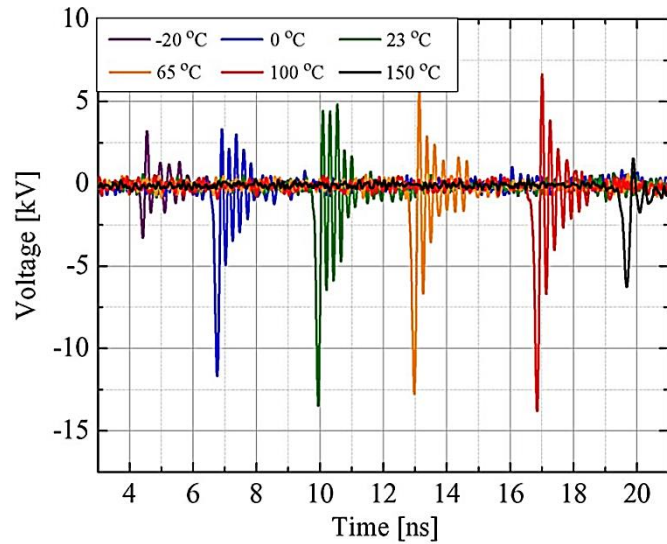
- Number of satellites: associated with the mission, revisiting requirements and is limited by cost;
- Altitude: associated with the payload and mission and limited by the launcher and the mass of the satellite;
- Coverage: associated with the mission and limited by the orbit and the range field of the payload;
- Schedule of the passes around the globe: associated with the mission;
- Operations: associated with the level of autonomy of the satellite, being limited by the availability of communication, personnel and cost.

3.1.1. Temperature Effects

One of the important factors that needs to be taken into account is the NLTL response when subjected to extremes of temperature in order to understand operational performance of transmission lines in the space environment. Bragg [23] performed several tests of a coaxial line using ferrites considering possible operational values, i.e. varying the temperature from -20.0°C to 150°C to check output signal at high voltage operation. These tests considered shots with incident pulse amplitudes of 40 kV for a 19 kA/m axial magnetic bias using a 30-cm line length.

Figure 3.1 [23] shows the output pulse amplitude, frequency and number of oscillations varying in the -20 °C/150°C temperature range. For extreme values at -20.0°C and 150°C, the pulse amplitude was highly impaired demonstrating the poor precession operation (low number of oscillations and VMD), while at other temperatures within this range, the pulse peak amplitude, number of oscillations and VMD have higher values demonstrating better performance.

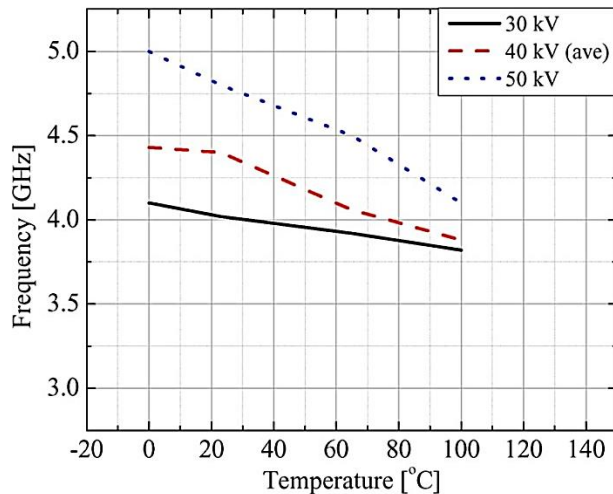
Figure 3.1. Gyromagnetic line output signals showing better performance between 0 and 100°C.



Source: [23].

In Figure 3.2 Bragg demonstrated that the frequency decays with the increase in temperature for different incident pulse amplitudes (30 kV, 40 kV and 50 kV).

Figure 3.2. Bragg's frequency response to different temperatures.



Source:[23].

From these results, ferrites demonstrate strong temperature dependence, influencing the precession movement that induces frequency oscillations on the output pulse. High temperatures make difficult the precession movement of the electron spin because of the magnetic domains agitation and, therefore the oscillations tend to stop. Elevated temperature in the ferrites can occur due to the heating generated by the pulse repetition rate and resistive losses in the solenoid. This observation is important as in space applications temperature is a critical parameter. For instance, satellites receive solar radiation at certain periods (reaching extremely high temperatures) and at other ones are eclipsed (reaching very low temperatures). The system should be able to support abrupt temperature changes without affecting the reliability of the signal transmitted.

3.1.2. Telecommunications Subsystem

Telecommunications subsystems must ensure information exchange between ground stations and space vehicles through the following functions:

- Tracking: determines the position and the motion of the satellite by using data about their angular positions and speed;
- Telemetry: encodes the measurement of the sensors for digital data transmission;
- Command: receives, verifies and executes commands for remote control of functions, configuration and motion of the satellite.

The basics concepts for this subsystem are: determination of the satellite state by telemetry transmitted via RF, acting on the satellite through telecommands transmitted by the ground segment. Determination of the orbit by the ranging of the distance between the satellite and the station, calculating the satellite radial velocity related to the station, and the orientation of the antenna. Determination of the satellite attitude, that is, the orientation of the satellite in space obtained

from onboard sensor data (part of the Attitude Control Subsystem) [1], [17], [18], [19], [20], [21], and [22].

The RF range is allocated for space operation for instance in the S band (Telecommand in 2025-2120 MHz and Telemetry in 2200-2300 MHz) according to the ITU (International Telecommunication Union) [24].

3.2. Radiofrequencies for Telecommunications

In the last decade, the number of satellites in orbit has increased considerably as a result of the advance of technologies to the design of space vehicles. Hence, in order to meet the mission requirements nowadays a broader frequency range is needed. As a consequence, the spectrum usage is a very important requirement, so that the interference with other bands like military, commercial, etc. can be avoided. In this case, the frequency range of interest is between 300.0 MHz and 30.0 GHz, and its classification is shown in Table 3.1 [24].

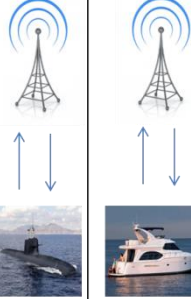
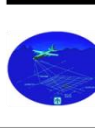
The radiofrequency part of the electromagnetic spectrum, located between 3.0 kHz and 300.0 GHz (see Table 3.2), has been used mainly in civilian telecommunications (radio, TV, mobile phone), military, and satellite communications. The bands used are UHF (Ultra High Frequency), SHF (Super High Frequency) and EHF (Extremely High Frequency). Other devices operate at these frequencies range, for example industrial and medical systems, microwave ovens, etc. [24]. The application, classification and its abbreviation, and the spectrum used are shown in Table 3.2, where LC discrete lines generally operate in VHF for radar application for example, and gyromagnetic lines in UHF for some satellite applications.

Table 3.1. Frequency range for satellite application [24].

| Radar Bands | Frequency | Application |
|-------------|---------------------|------------------------------------------------------------------------------------------------------------|
| P | 300.0 MHz – 1.0 GHz | Radar application (SAR) |
| L | 1.0 – 2.0GHz | Mobile Satellite Service (MSS), UHF TV, terrestrial microwave and studio television links, cellular phone. |
| S | 2.0 – 4.0 GHz | MSS, Digital Audio Radio Service (DARS) and deep space research. |
| C | 4.0 – 8.0 GHz | Fixed Satellite Service (FSS), fixed service terrestrial microwave. |
| X | 8.0 – 12.5 GHz | FSS, military communication, DARS feeder links, terrestrial fixed service, Earth observation satellites. |
| Ku | 12.5 – 18.0 GHz | FSS, Broadcast Satellite Service (BSS) microwave terrestrial fixed service. |
| K | 18.0 – 26.5 GHz | BSS, FSS, microwave terrestrial fixed service, local multichannel distribution service (LMDS) |
| Ka | 26.5 – 40.0 GHz | FSS, microwave terrestrial fixed service, LMDS, Intersatellite links (ISL), satellite imaging. |

Source: Author's production.

Table 3.2. Frequency spectrum classification.

| | | | | | | | | |
|-----------------------------------------------------------------------------------|-----------------------------------------------------------------------------------|-----------------------------------------------------------------------------------|--------------------------|-----------------------------------------------------------------------------------|-----------------------------------------------------------------------------------|------------------------------------------------------------------------------------|-------------------------------------------------------------------------------------|-------------------------------------------------------------------------------------|
|  |  |  | |  |  |  |  |  |
| Application | Submarine, navigation | Boats orientation | AM radio, aviation radio | Shortwave radio | VHF TV, FM radio | UHF TV, Mobile phone, GPS, Wi-Fi, 4G | Satellite communication, Wi-Fi | Satellite communication, Radio astronomy |
| Spectrum | 3 – 30 kHz | 30 – 300 kHz | 300 – 3000 kHz | 3 – 30 MHz | 30 – 300 MHz | 300 – 3000 MHz | 3 – 30 GHz | 30 – 300 GHz |
| Abbreviation | VLF | LF | MF | HF | VHF | UHF | SHF | EHF |
| Classification | Very Low Frequency | Low Frequency | Medium Frequency | High Frequency | Very High Frequency | Ultra High Frequency | Super High Frequency | Extremely High Frequency |

Source: Author's production.

3.2.1. Synthetic Aperture Radar

Radar satellites are used in remote sensing to provide data and information for different applications as for example climate change, deforestation detection, development of urban areas, mobility, forecast of natural disasters (hurricanes, tsunamis, volcanoes, etc.) and in the military area [25], [26] and [27]. Its operation is based on radar which comprises basically a transmitter, receiver, antenna and electronic system to process and record data. The transmitter generates a succession of pulses in the microwave range in a regular interval, transmitted by an antenna directed for a specific target. When the target is reached by this electromagnetic wave, part of the wave is absorbed and part is reflected. The portion that is reflected back to the antenna has different return and time intensities, which depend on the type of target and its distance in relation to the antenna. The frequency range used for SAR pulse emission is in

the microwave range, which occupies a large band in the frequency spectrum from 300.0 MHz to 300.0 GHz.

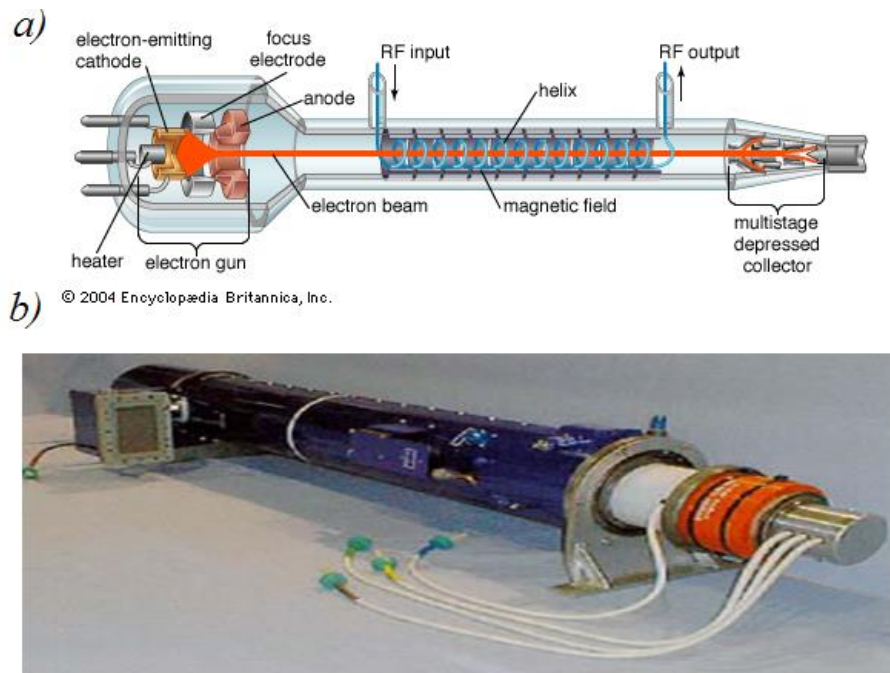
3.3. Traveling Wave Tubes

Traveling Wave Tubes (TWTs) are used in the frequency range 300.0 MHz – 50.0 GHz, and with a capability of power generation from watts to megawatts. Their application can be very wide, as for example radars, final high power amplifiers in electronic warfare with the goal of transmitting RF pulses and as drivers for other devices such as crossed-field amplifiers. In particular, TWTs are largely used as final amplifiers in satellite communications [2]. One example of the great reliability of this device is the X-band TWT implemented on the Voyager I satellite, which was designed as a backup device in case of failure of the solid-state amplifier. The failure occurred and the X-band TWT is still in operation after 28 years in space [28]. TWTs are amplifiers and they need a low power RF seed source. The schematic of a traveling wave tube with the most important components is shown in Figure 3.3 a) and b). Conceptually, the electron gun, electron beam, and collector have the similar designs for all TWTs. However, there are substantial differences in the RF circuits. Despite these differences, the TWTs operate under the same working principle [28].

An alternative way of reaching the same RF generation produced by the TWTs¹ to establish communication between the ground station and satellite, could be the use of NLTLs (explained in the next subsection) as gyromagnetic lines are all solid-state and of compact size not requiring heating filament and vacuum.

¹ In this thesis, TWTs are used as comparison basis instead of Solid State Amplifiers (SSA) because the power generated by SSA devices is very low (tens of watts) while TWTs and gyromagnetic lines operate at tens of kilowatts.

Figure 3.3. Traveling wave Tube a) Inner/structure view b) Outside view.



Source: [30], [31].

3.4. Nonlinear Transmission Lines

Nonlinear Transmission Lines (NLTLs) have been used with success to produce High Power Microwave (HPM) oscillations in recent years [32]. These lines are interesting due to their compact structures, with high power at high frequency operation [33]. The main property of NLTLs is the nonlinear material employed in the device as nonlinear dielectrics [34] or magnetic [35] medium where the latter has been shown to be more efficient [36] to-date. A brief description using both dielectric and magnetic materials is given in the next subsections (3.4.1 and 3.4.2).

To understand the nonlinear effect of the line when an input pulse is injected onto the line, to a first approximation the dispersive effect is disregarded [37],

[38]. When the input pulse is injected, it propagates along the line length with a velocity defined by

$$v = \frac{1}{\sqrt{\mu\epsilon}} \quad (3.1)$$

where μ is the magnetic permeability and ϵ is the electrical permittivity. However, if the dielectric of the line is nonlinear, for example, ceramic materials, during the pulse propagation in this medium, the higher portion of the voltage pulse will travel faster than the leading edge since ϵ decreases as the voltage increases. Then, the line delay is bigger for the parts of the pulse of lower intensity [39]. Analogously, this same compression effect can be obtained by the use of nonlinear magnetic materials, since the permeability (μ) of these materials decreases with the current increase, as for ferrite for example [40].

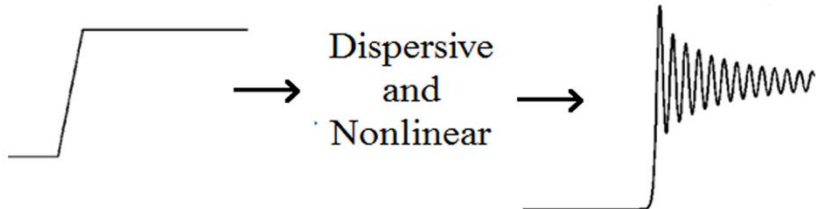
Each one of these methods can be used for generation of very fast output pulses with high power levels [41], [42].

3.4.1. Nonlinear Discrete LC lines

The discrete LC lines also referred to as a Nonlinear Lumped Element Transmission Line (NLET), consists of periodic sections of nonlinear inductors and/or capacitors, where a square input pulse injected onto the line will be submitted to the dispersion effect, and subsequently modulated and decomposed into a series of solitons (oscillatory pulses – see Figure 3.4). The reason for this is due to the NLTL working principle based on a balance between two characteristic line properties: dispersion and nonlinearity. Transmission lines built with discrete elements are responsible for the dispersion effect and the elements used as varicap diodes, ceramic capacitors

and/or saturated inductors are responsible for the characteristic of nonlinearity of the line [42]. Generally, as variable capacitors a network of varactor diodes is used (because of the excellent nonlinear characteristic of the junction capacitances) [44] or ceramic capacitors (whose capacitance have an inverse relation with the voltage) [45]. Another possibility is the construction of an inductive line with variable L as reported by Seddon et al. [8], using cross-link capacitors between the sections to help the compensation of the dispersive effect by the line nonlinearity. The properties of the line lead to the characteristic formation of a soliton. Nonlinearity and dispersion act together to provide the high-frequency oscillations along the line, which can be used to irradiate RF through an antenna matched to the line output. As illustrated in Figure 3.4, a NLETL can be used to convert a rectangular input pulse into a train of oscillatory pulses [9], [46], [47], [48].

Figure 3.4. Input pulse and output waveform on a dispersive NLTL.

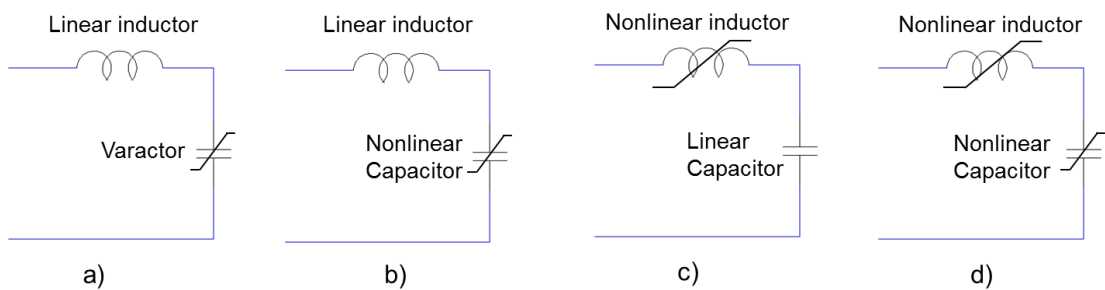


Source: Author's production.

For the nonlinear effect, the line needs at least one of the components with nonlinear behavior (capacitors with the capacitance varying with the applied voltage $C(V)$ or inductors whose inductance varies with the current $L(I)$). For dispersion, the line periodicity provides this effect [49], [50], [51]. The line schematic is a cascade network of LC sections that can be implemented according to four different settings as shown in Figure 3.5.

The first two settings in Figure 3.5 are capacitive lines, and the difference between them is that the first Figure 3.5 (a) built with varactor diodes is suitable only for low voltage operation, while the second one Figure 3.5 (b) built with ceramic capacitors is for high voltage operation. The third configuration Figure 3.5 (c) is an inductive line, and in this case nonlinear inductors are used. The last one Figure 3.5 (d) is a hybrid line, where both nonlinear components $L(I)$ and $C(V)$ are used.

Figure 3.5. The different possible settings for the discrete nonlinear LC line
a) Capacitive line for low voltage operation, b) Capacitive line for high voltage operation, c) Inductive line, d) Hybrid line.



Source: Author's production.

To induce soliton formation (further explained in 3.4.1.1) along the line, a nonlinear dielectric dispersive lumped line is used, where the phase velocity is:

$$v_{ph} = \frac{1}{\sqrt{LC(V_{max})}} \quad (3.2)$$

where L and $C(V_{max})$ are respectively the linear inductance per section and the nonlinear capacitance per section. As the line is dispersive the rise time will be

limited approximately by the inverse of the line Bragg cutoff frequency given by [52]:

$$f_{c0} = \frac{1}{\pi\sqrt{LC(V_{max})}}. \quad (3.3)$$

The accurate calculation of the pulse rise time reduction at the output is difficult to achieve due to the line nonlinearity and the dependence of the phase velocity on frequency in dispersive lines. However, an estimate can be made by calculating the difference between the propagation times of the portion of the pulse with lower amplitude and its peak. Therefore, for the lower portion of an input pulse propagating along a linear line, the delay is given approximately by:

$$\delta_1 = n \sqrt{LC_0}, \quad (3.4)$$

where n is the number of sections of the line. While for the peak of the propagating pulse the delay is equivalent to:

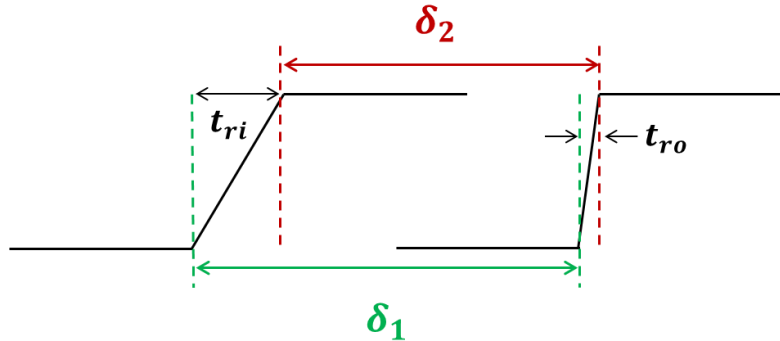
$$\delta_2 = n \sqrt{LC(V_{max})}, \quad (3.5)$$

and therefore, according to Figure 3.6 the rise time reduction of the output pulse is given by [52]:

$$\Delta T = \delta_1 - \delta_2 = t_{ri} - t_{ro} = n(\sqrt{LC_0} - \sqrt{LC(V_{max})}) \quad (3.6)$$

where t_{ri} and t_{ro} are the input and output rise times, respectively.

Figure 3.6. Compression of the output pulse in a NLT.



Source: Author's production.

From the parameters t_{ri} and t_{ro} in Figure 3.6, the following relations can be derived:

$$t_{ri} + \delta_2 = t_{ro} + \delta_1, \quad (3.7)$$

which gives:

$$t_{ro} = t_{ri} - \Delta T \quad (3.8)$$

when $t_{ri} > \Delta T$, there occurs the output pulse compression. On the other hand, when $t_{ri} \leq \Delta T$, the shock wave rise time cannot drop to zero, since in this case

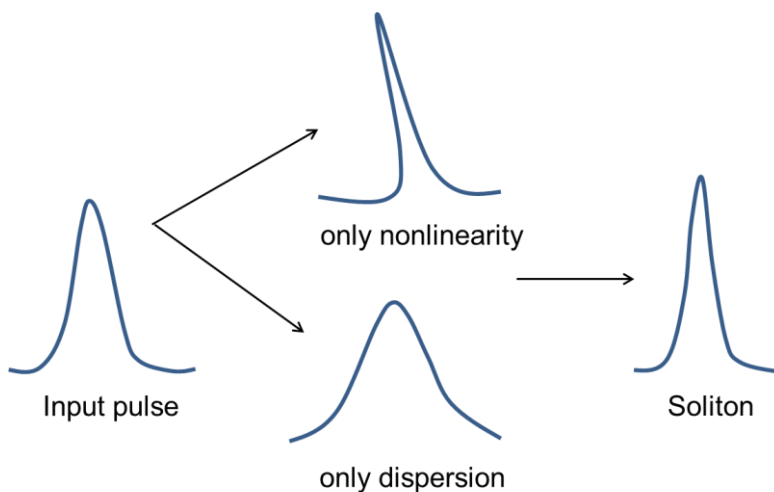
it is limited by the line cutoff frequency f_{c0} because of the lumped line dispersions and, thus $t_{ro(min)} \cong \frac{1}{f_{c0}} = \pi\sqrt{LC(V_{max})}$ (see (3.3)). Therefore, above this frequency the energy cannot propagate, generating a series of narrow pulses (solitary waves) along the line and at its output, as the output pulse can no longer be compressed.

Thus, with relation to the ΔT and t_{ri} parameters:

- $t_{ri} \leq \Delta T$: the dispersion compensates the nonlinearity (soliton formation);
- $t_{ri} > \Delta T$: the nonlinearity overcomes the dispersion (output pulse sharpening).

The properties of the line corresponding to the characteristics of soliton formation (nonlinearity and dispersion) acting together allows the appearance of high frequency oscillations along the line as shown in Figure 3.7.

Figure 3.7. Soliton formation.



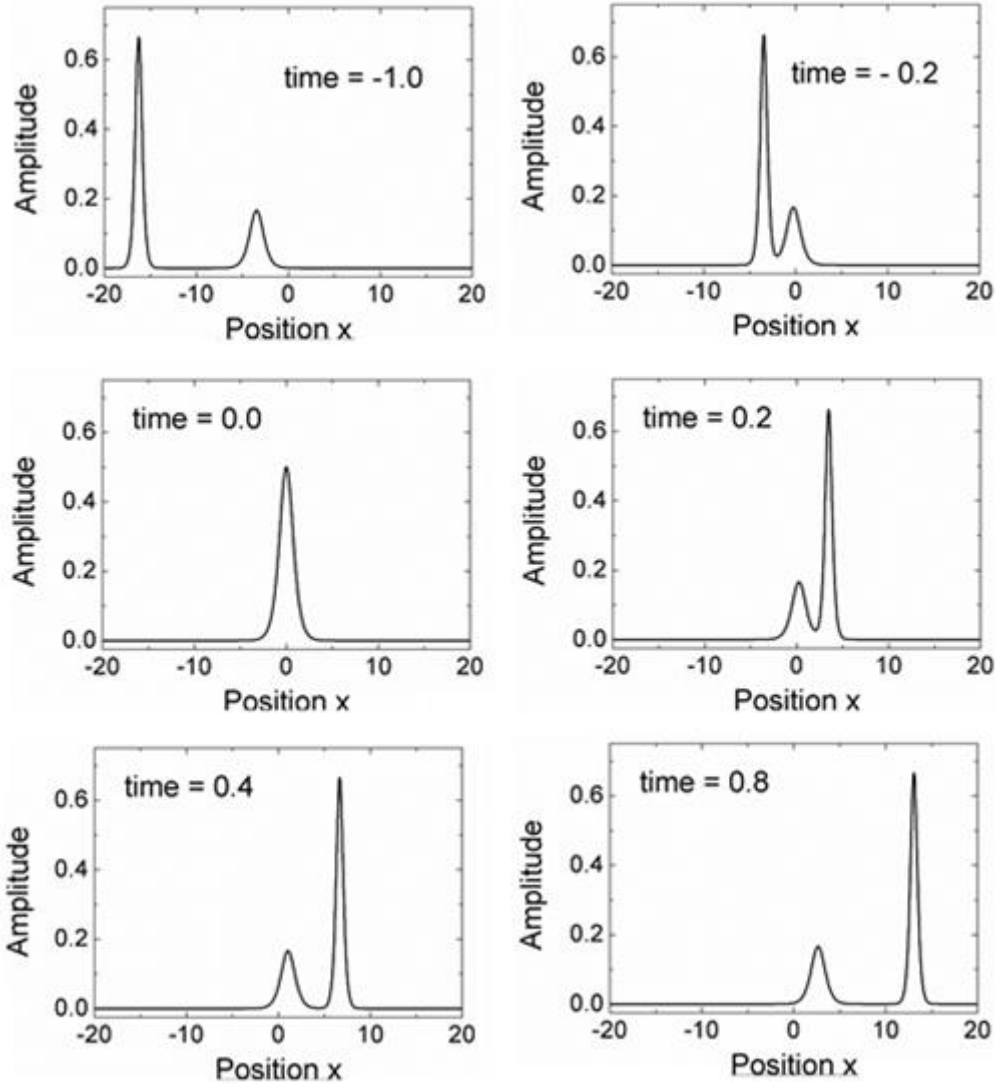
Source: Author's production.

3.4.1.1. Solitons

Solitons are solitary waves that propagate in the medium without changing its shape and velocity over a long period and distance. They were noticed for the first time by John Scott Russell in 1834, while he was observing a boat in an Edinburgh (Scotland) channel. He verified that, when the boat was suddenly stopped, there appeared a big wave with rounded and well defined shape that propagated with constant velocity through the channel. After this observation, Russell performed several laboratory experiences generating solitary waves by plunging a weight on one end of a long receptacle filled with water that simulated shallow channels, as in his first observations of solitary waves. During these experiments, Russell observed that the larger the wave amplitude, the larger the propagation velocity. In Figure 3.8 are shown six different times during the propagation of two solitary waves in the same medium [51]. It is possible to observe that the solitary wave with smaller peak is slower and overpassed by the one with higher peak that is also faster, which is in agreement with Russell's observations [53], [54], [55].

Another fact observed by Russell in 1844 is that in collisions, solitary waves retain their characteristics (see Figure 3.8, where two waves collide and, after the shock, keep propagating with the same shape before the interaction). In the same way demonstrated in Figure 3.8, in one of his experiments Russell created two solitary waves with different velocities and observed that the faster wave reached, interacted and exceeded the slower wave in such a way that after the process, both remained intact [53].

Figure 3.8. Solitons collision and conservation of the waves showing normalized amplitudes as function of position at given normalized times.



Source: [51].

3.4.2. Basic Concepts of Gyromagnetic Lines

Gyromagnetic NLTLs generate microwaves induced by the damped gyromagnetic precession of the magnetic moments in the ferromagnetic material, and thus, are used as compact, solid-state, RF sources [56]. The output frequency of a NLTL can be adjusted by controlling the bias magnetic field applied externally and by the amplitude of incident voltage pulse [57]. The

output power is determined by the intrinsic properties of the ferromagnetic material and by the transmission line dimension [36].

The principle of operation of the gyromagnetic line is based on the sharpening of the output pulse in relation to the input pulse, caused by the dependence of the magnetic permeability of the material on the current applied [58]. As the current pulse propagates down the line the magnetic permeability decreases with the current amplitude. Thus, the crest of the pulse will travel faster than its portion of lower amplitude since the propagation velocity in a nonlinear magnetic medium is given by:

$$v_p = \frac{c}{\sqrt{\epsilon_r \mu_r(I)}}, \quad (3.9)$$

where c is the speed of light in vacuum, $\mu_r(I)$ is the relative magnetic permeability that varies with the current I and ϵ_r is the relative electrical permittivity.

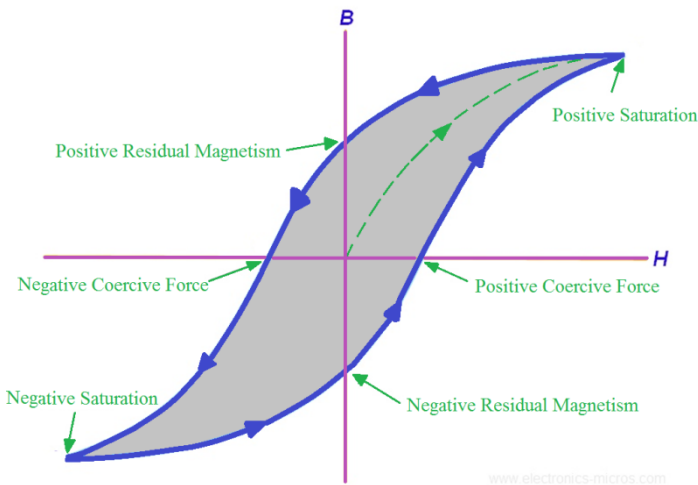
As the leading edge of the input pulse with higher amplitude travels faster than the portion of smaller amplitude, the emerging output pulse is sharpened. In this case, the pulse rise-time reduction at line output can be estimated as [51]:

$$\Delta T = \pi(\sqrt{LC} - \sqrt{L_{sat}C}) \quad (3.10)$$

where L is the coaxial line inductance far from saturation, L_{sat} is the saturated inductance of the coaxial line, and C is the coaxial line capacitance.

The pulse rise time reduction is limited by the switching characteristics of the ferrite due to the time it takes to switch from one state to another on the B-H curve (see Figure 3.9) of the material, which is related to the relaxation frequency of the magnetic material [11].

Figure 3.9. B-H curve of a magnetic material.



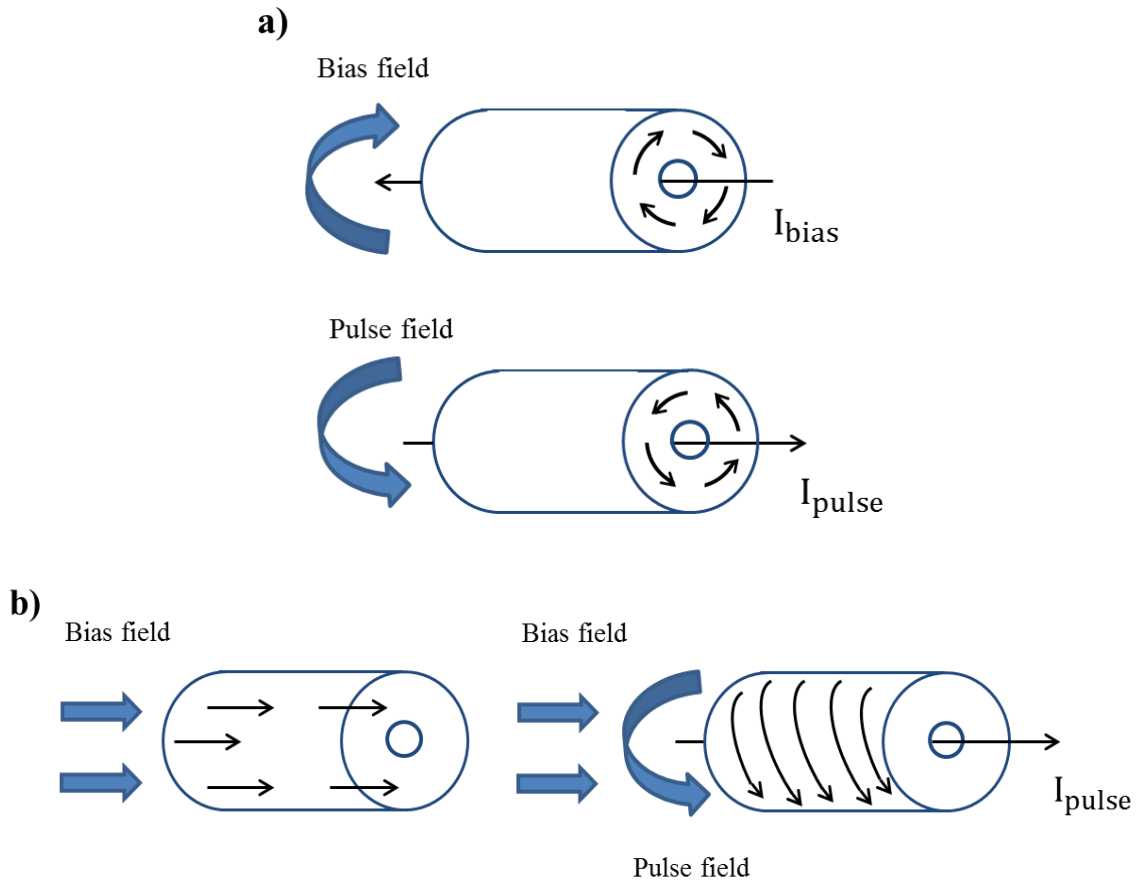
Source: Author's production.

3.4.2.1. Types of Bias

The coaxial line can be biased in two different ways, using azimuthal bias (as seen in Figure 3.10 (a)) for pulse compression or axial bias (as seen in Figure 3.10 (b)) for efficient RF generation from magnetic precession. For pulse compression, the line is biased by a DC current flowing through the inner conductor so that the ferrites are saturated in the opposite direction to that when a current pulse is injected onto the line, also known as azimuthal bias shown in Figure 3.10 (a). Indeed, pulse compression occurs even if the lines are not biased, as long as a reset pulse is applied to degauss the line before the arrival of the next current pulse. For RF generation the axial bias is used as in Figure

3.10 (b) where the total effective field is twisted as the azimuthal field generated by the current pulse injected onto the line is superimposed on the axial field.

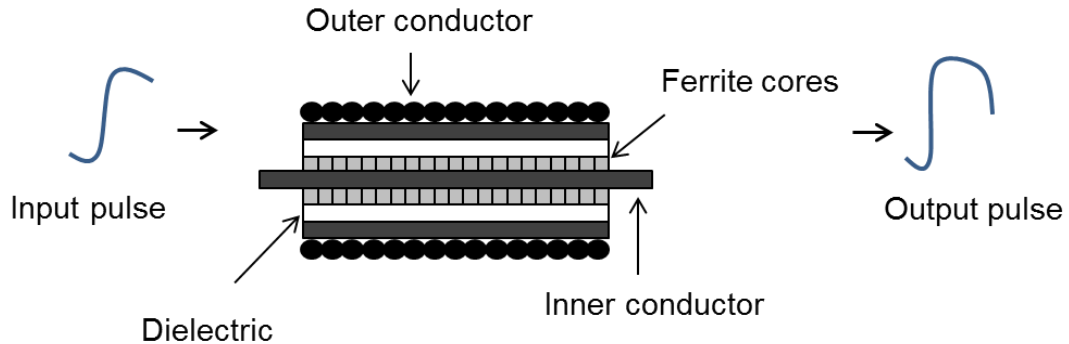
Figure 3.10. Types of bias a) azimuthal and b) axial.



Source: Author's production.

Another way of improving the pulse compression with a rise time smaller than 1.0 ns consists of biasing the line by an axial field as shown in Figure 3.10 (b) produced with the use of permanent magnets or a solenoid, as demonstrated in Figure 3.11.

Figure 3.11. Continuous line with magnetic material used for pulse compression.

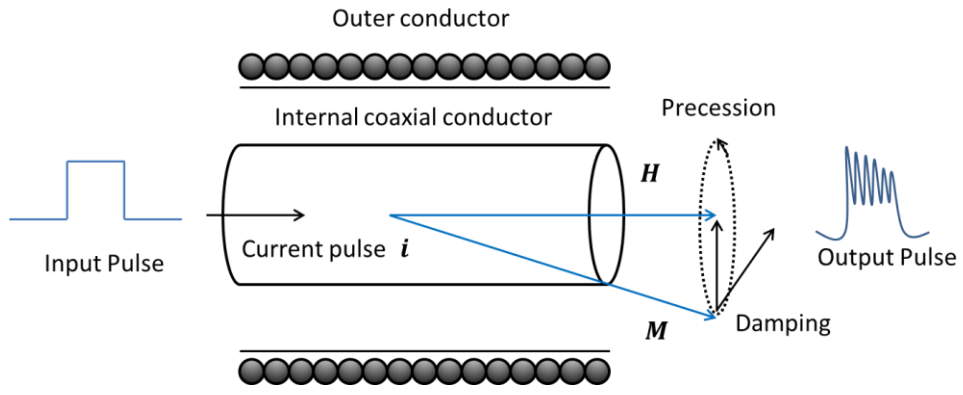


Source: Author's production.

By introducing axial bias into the line, the precession effect of the magnetic moments in the ferrite must be considered, since it causes oscillations in the amplitude of the output pulse [59]. On the other hand, for azimuthal bias, this effect is neglected. A detailed explanation for this precession effect is also illustrated in Figure 3.12.

As shown in Figure 3.12, assuming that the line is immersed in an axial magnetic field H , as soon as a current pulse I is injected, the magnetic moment M of the ferrite, initially aligned along the axis, interacts with the azimuthal field generated around the conductor, saturating and leading to pulse compression. At the same time, because of the magnetic torque, a precessional motion of the magnetic moment in high frequency with a damping factor α occurs which depends on the characteristics of the ferrite.

Figure 3.12. Precession of the magnetic moment M in ferrites.



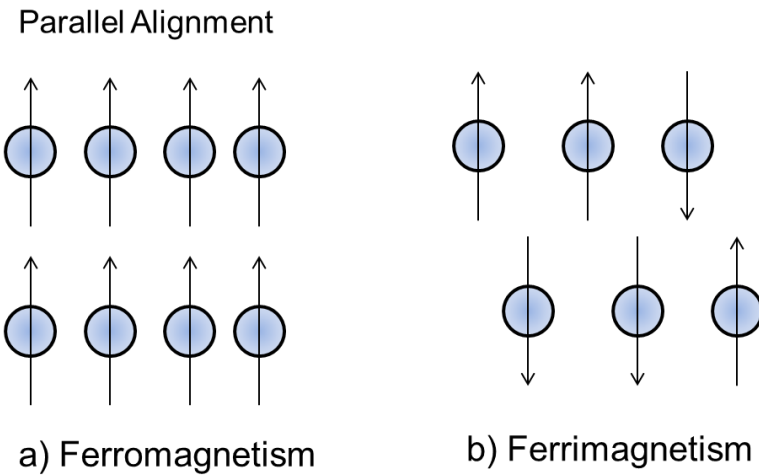
Source: Author's production.

The magnetic precession motion in ferrites takes place along the line as soon as the current pulse propagates, inducing high-frequency oscillations. These oscillations appear superimposed on the amplitude of the output pulse with a similar shape to that of the input pulse, but with a reduced rise time.

3.4.2.2. Basics of Ferrimagnetism

Magnetism is a result of the alignment of regions in the material known as magnetic domains. Ferromagnetic materials exhibit parallel alignment of moments resulting in the magnetization even in the absence of an externally applied magnetic field. In these elements, the magnetic moments are aligned in the same direction to produce strong permanent magnets (see Figure 3.13 (a)). On the other hand, for ferrimagnetic materials the magnetic moments are in opposite directions as shown in Figure 3.13 (b) and they can be magnetized with the influence of an external magnetic field [60].

Figure 3.13. Alignment of (a) Ferromagnetic and (b) Ferrimagnetic materials.



Source: Author's production.

The magnetic properties of a material are related to the existence of magnetic dipole moments, which arise primarily from the electron spin. The magnetic dipole moment of an electron due to its spin is given by:

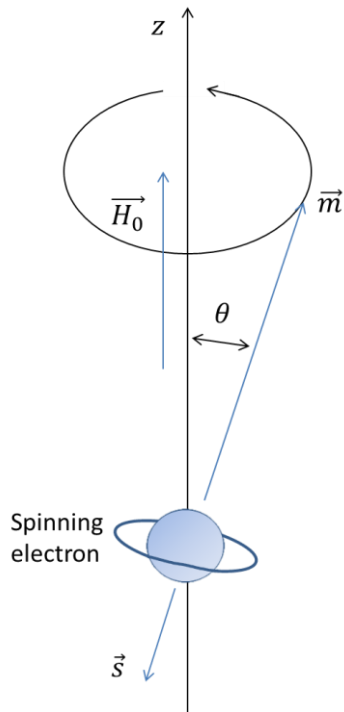
$$\vec{m} = \frac{q\hbar}{2m_e} = 9.27 \times 10^{-24} A - m^2 \quad (3.11)$$

where \hbar is Planck's constant divided by 2π , q is the electron charge, and m_e is the mass of the electron [60]. Considering that an electron has a spin angular momentum given in terms of Planck's constant as:

$$s = \frac{\hbar}{2} \quad (3.12)$$

and the vector direction of the angular momentum \vec{s} is opposite to the direction of the spin magnetic dipole moment \vec{m} as shown in Figure 3.14.

Figure 3.14. Spin magnetic dipole moment and angular momentum vectors for a spinning electron.



Source: [60].

The ratio of the spin magnetic moment to the spin angular momentum is a constant known as the gyromagnetic ratio:

$$\gamma = \frac{m}{s} = \frac{q}{m_e} = 1.759 \times \frac{10^{11} C}{kg}. \quad (3.13)$$

Then, the vector relation between the magnetic moment and the angular momentum is

$$\vec{m} = -\gamma \vec{s}, \quad (3.14)$$

where the negative sign is due to the fact that these vectors are oppositely directed. When a magnetic bias field $\vec{H}_0 = \hat{z}H_0$ is present, a torque occurs on the magnetic dipole:

$$\vec{T} = \vec{m} \times \vec{B}_0 = \mu_0 \vec{m} \times \vec{H}_0 = -\mu_0 \gamma \vec{s} \times \vec{H}_0. \quad (3.15)$$

Since torque is equal to the time rate of change of angular momentum

$$\frac{d\vec{s}}{dt} = \frac{-1}{\gamma} \frac{d\vec{m}}{dt} = \vec{T} = \mu_0 \vec{m} \times \vec{H}_0. \quad (3.16)$$

Finally, the motion of the magnetic dipole moment \vec{m} is given by

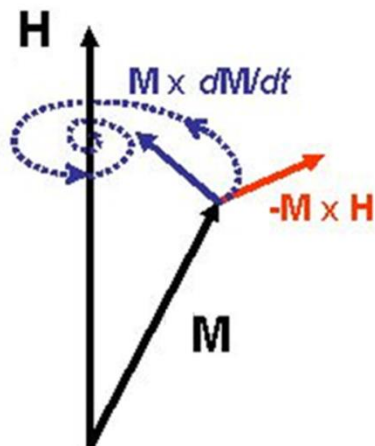
$$\frac{d\vec{m}}{dt} = -\mu_0 \gamma \vec{m} \times \vec{H}_0. \quad (3.17)$$

3.4.2.3. LLG equation

The Landau Lifshitz Gilbert equation, better known as the LLG equation since 1954 is the modified version of the original Landau-Lifshitz equation dated from

1935 that describes the precession movement of the magnetization M in ferrites [61], [62]. This equation is used to model the behavior in the time domain of magnetic elements due to the presence of a magnetic field. The LLG equation describes the rotation of the magnetization in response to torques. Figure 3.15 illustrates its working principle where the damped magnetic motion of precession is given by the dashed trajectory [63].

Figure 3.15. The dynamics described by the LLG equation, in which the magnetization M precesses around H with damping.



Source: [63].

The vectors $\vec{M} \times \vec{H}$ in red, and $\vec{M} \times \frac{\partial \vec{M}}{\partial t}$ in blue stand, separately, for the magnetic precession and damped motion, respectively, which combined give the dashed trajectory in Figure 3.15. The trajectory of the spiral magnetization is drawn under the simplified assumption that the field H is a combination of the bias field plus the field generated by a current pulse through the NLTL in the r, θ, z directions. The movement of the magnetization vector \vec{M} is described by the LLG equation as [64]:

$$\frac{\partial \vec{M}}{\partial t} = \gamma \mu_0 \vec{M} \times \vec{H} - \frac{\alpha}{M_s} \mu_0 \vec{M} \times \frac{\partial \vec{M}}{\partial t} \quad (3.18)$$

where H is the axial magnetic field vector, M_s the saturation magnetization, μ_0 is the magnetic permeability of vacuum, $\gamma = 1.76 \times 10^{11} (\text{rad s}^{-1} \text{T}^{-1})$ is the gyromagnetic ratio of the electron, and α is the precession damping constant, which depends on the material. The first term on the right of the LLG equation represents the precessional motion, while the second one represents the dissipative factor of the oscillating movement. This equation is in the form proposed by Gilbert, whose dissipative term differs from the original expression described by Landau and Lifshitz (LL) as

$$\frac{\partial \vec{M}}{\partial t} = \gamma \mu_0 \vec{M} \times \vec{H} - \frac{\alpha \gamma \mu_0}{M_s} \vec{M} \times (\vec{M} \times \vec{H}). \quad (3.19)$$

As demonstrated in Appendix A.2 when the dissipation coefficient becomes $\alpha \ll 1$, equations (3.18) and (3.19) become equivalent.

Thus, considering only the dissipative term in (3.19), this equation reduces to (see Appendix A.2):

$$\frac{\partial \vec{M}}{\partial t} \cong -\frac{\gamma \mu_0}{(1+\alpha^2) M_s} \frac{\alpha}{M_s} [\vec{M} \times (\vec{M} \times \vec{H})]. \quad (3.20)$$

Using the vector identities below:

$$\mathbf{a} \times (\mathbf{b} \times \mathbf{c}) = \mathbf{b}(\mathbf{a} \cdot \mathbf{c}) - \mathbf{c}(\mathbf{a} \cdot \mathbf{b}), \quad (3.21)$$

and noting that $\vec{M} \cdot \vec{M} = M^2$ and $\vec{M} \times \vec{H}$ in Figure 3.15 is in the azimuthal direction (3.20) can be simplified as:

$$\frac{\partial \vec{M}}{\partial t} \cong -\frac{\gamma \mu_0}{1+\alpha^2} \frac{\alpha}{M_s} [\vec{M}(\vec{M} \cdot \vec{H}) - \vec{H}(\vec{M} \cdot \vec{M})] \quad (3.22)$$

$$\frac{\partial \vec{M}}{\partial t} = -\frac{\gamma \mu_0 \alpha}{(1+\alpha^2)M_s} [(\vec{M}(\vec{M} \cdot \vec{H}) - \vec{H}M^2)]. \quad (3.23)$$

By using cylindrical coordinate, the rate of change of azimuthal magnetization is recast in the form:

$$\frac{dM_\theta}{dt} = \frac{\gamma \mu_0 \alpha}{1+\alpha^2} M_s \left(1 - \frac{M_\theta^2}{M_s^2}\right) H_\theta = \frac{M_s}{S} \mu_0 \left(1 - \frac{M_\theta^2}{M^2}\right) H_\theta, \quad (3.24)$$

where $|\vec{M}| = M_\theta$ and $|\vec{H}| = H_\theta$ are respectively the magnetic moment and the magnetic field applied in the azimuthal direction, where the switching constant, S, in (3.24) is expressed as a function of the gyromagnetic ratio and the damping factor by:

$$S = \frac{1+\alpha^2}{\alpha} \gamma^{-1} = \left(\frac{1}{\alpha} + \alpha\right) \gamma^{-1}. \quad (3.25)$$

The demagnetizing field due to the application of the current pulse I cancels the initial magnetic moment during the switching interval in the reverse transition of the ferrite magnetization, passing from $-M_s$ to $+M_s$. This switching interval depends on the applied magnetic field H and on the switching constant S which in turn derives from the ferrite characteristics such as:

$$\tau = \frac{S}{(H - H_c)}, \quad (3.26)$$

where H_c is the coercive field (Figure 3.7). The switching time τ can reach less than 1.0 ns (in the range of hundreds of ps) depending on the intensity of the applied field and on the constant S . Equation (3.26) assumes that magnetic switching time is inversely proportional to the magnetic field applied onto ferrites with azimuthal bias only.

On the other hand, with axial bias, magnetic precession takes place and calculation of the precession frequency becomes a key issue when designing gyromagnetic NLTs. One way of doing that is to simplify the original equation (3.19) by neglecting the dissipation term, which transforms into

$$\frac{\partial \vec{M}}{\partial t} = \gamma \mu_0 \vec{M} \times \vec{H}. \quad (3.27)$$

By assuming transverse electromagnetic mode (TEM) propagation in the gyromagnetic coaxial line, the set of telegraphist equations along axis z for the voltage V and current I can be written as

$$\frac{dI}{dz} = -C_o \frac{dV}{dt} \quad (3.28)$$

$$\frac{dV}{dz} = -\frac{d\Phi}{dt} = -\frac{d(LI)}{dt} \quad (3.29)$$

where Φ is the flux, C_0 is the line capacitance per meter, and L is the total line inductance per meter. Coupling the LLG magnetization to the TEM mode equation (3.29) becomes:

$$\frac{dV}{dz} = -L_0 \frac{dI}{dt} - \mu_0(b - a) \frac{dM}{dt} \quad (3.30)$$

where L_0 is the air or saturated line inductance per meter and b and a are respectively the outer and inner radii of the ferrite. The magnetic field H is a sum of two components: the azimuthal component H_θ generated by the current pulse I and the axial z -component ($H_z = H_0$) associated with the external bias and with the gyromagnetic resonant frequency ($\omega_0 = \gamma H_0$). The azimuthal field can be calculated as a function of the current pulse amplitude such as $H_\theta = I/\pi(b - a)$ and the magnetization variation in the transverse direction z can also be neglected such that $dM/dt = dM_\theta/dt$. Using these three equations and supposing that the azimuthal magnetic field produced by the high voltage pulse applied does not change the magnitude of the magnetization but only its direction because of rotational movement around H (that is, $|\vec{M}| = M_s$ for a saturated ferrite), Romanchenko reported in [64] that the center frequency of oscillations superimposed on the amplitude of the pulse voltage propagating along the line can be given by:

$$f_c = \frac{\gamma}{4\pi} \mu_0 H_\theta \sqrt{1 + \frac{\chi M_s}{\mu_0 \sqrt{H_\theta^2 + H_z^2}}}, \quad (3.31)$$

where χ is the ferrite filling factor of the NLTL. Neglecting the first term “1” in the square root as the second is normally much bigger and for $H_z \gg H_\theta$ one obtains:

$$f_c \approx \frac{\gamma}{4\pi} \mu_0 H_\theta \sqrt{\frac{\chi M_s}{\mu_0 H_z}}. \quad (3.32)$$

Equation (3.32) shows that the gyromagnetic NLTL strongly depends on the amplitude of the incident pulse and on the static magnetic bias. As it can be confirmed in several papers [64],[65] the NLTL performance trend indicates that the center frequency decreases with the static magnetic field and increases with the input pulse amplitude because of the azimuthal field produced, which is also according to (3.32). The explanation for this phenomenon is due to the TEM mode wave that propagates down the coaxial line coupled to the azimuthal magnetic field generated by the incident pulse. If the static magnetic bias increases, the rotating azimuthal M field component decreases, lowering the frequency of oscillations. On the contrary, if the incident pulse increases the azimuthal M contribution increases, raising the frequency.

3.5. Models to be Studied

The existing theories behind the pulse sharpening effect in ferrite-loaded lines were first explained extensively by Katayev [12] in 1966, who gave a basic mathematical description of the concept. Three decades later, Weiner [13] in 1989 produced an article describing a simplified theory based on Katayev's

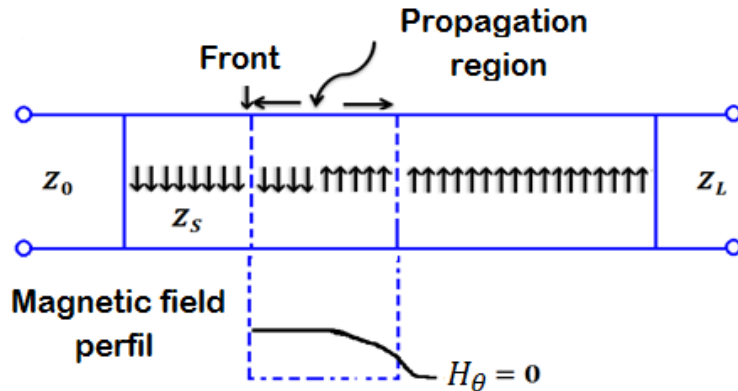
explanations. In 1989, Pouladian-Kari et al. [14] developed a frequency-enhanced model to improve the model for the rise time compression of the output pulse proposed by Weiner to predict the magnetic precession in ferrites. Then, Pouladian-Kari and Shapland [15] in 1991 used this model to compare with experimental results using two different settings of axial bias field (constant and linearly graded). Finally, Dolan [16] in 2000 proposed a better model than from Pouladian for simulating the pulse compression precession effect, using a linear transmission model with voltages sources in series with the line linear inductor.

3.5.1. Weiner's Model

Weiner [13] used a ferrite transmission line, which is uniformly magnetized in the transverse direction to the propagation path. A transmission line without ferrite, with impedance Z_0 , is connected to the input terminals of the ferrite line. A pulse with rise time t_r is incident onto the ferrite line. The polarity of the pulse magnetic field is opposite to that of the magnetization. As a result, a spin reversal process will be initiated, and the pulse will see large RF line impedance Z_f with high inductance as well as a resistive component caused by dissipation in ferrite. However, the ferrite line will not continually appear with large impedance, as the line goes into saturation with the shock wave front caused by the current pulse. As shown in Figure 3.16, as this process continues, the spin saturation front propagates along the length of the ferrite.

Weiner's model was the first one to be studied and analyzed in this thesis. For the calculation of the distributed parameter of ferrite coaxial line, Weiner [13] used an analytical model that considers the effect of the shock wave propagating along the line, showing the reversal region of the magnetic moment in the ferrite, which evolves according to Figure 3.16.

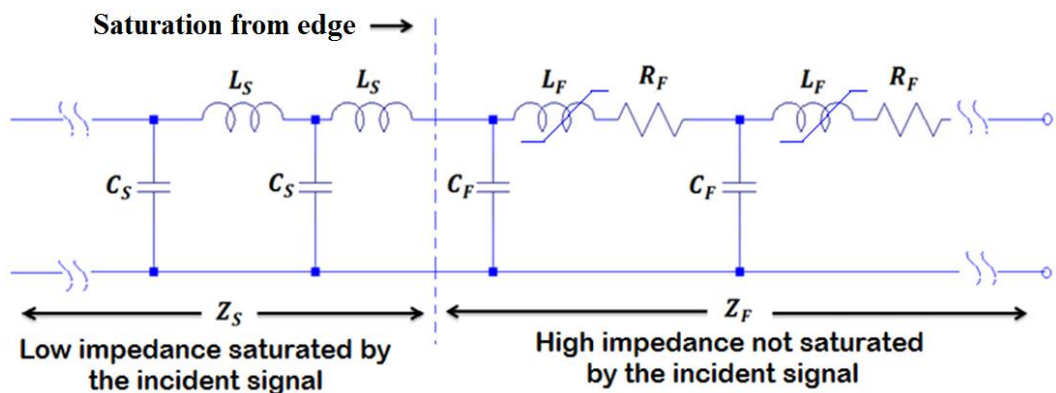
Figure 3.16. Propagating front showing the reverse transition region moving along the line.



Source: Author's production.

Figure 3.17 shows the equivalent circuit of the transmission line according to the proposed model. Eventually, the initial part of the ferrite line will reach saturation. When this happens, the high impedance suddenly drops to the saturated impedance, chosen equal to Z_0 , the input impedance according to Weiner's model [13].

Figure 3.17. Equivalent circuit of the ferrite line proposed by Weiner.



Source: Author's production.

Based on the conventional theory of transmission lines and the flow relations in the ferrite, the magnetic flux per meter in the transmission line is increased substantially by the nonlinear term of magnetization M_θ as:

$$\Phi = L_0 I + \mu_0 \int_a^b M_\theta(r) dr, \quad (3.33)$$

where $\mu_0 = 4\pi \times 10^{-7} H/m$ is the magnetic permeability of vacuum, and b and a are the ferrite outer and inner radii. If the difference between a and b is not large (see Figure 3.18), it can be assumed that the magnetization is not dependent on ferrite radius and (3.33) can be given by:

$$\Phi = L_0 I + \mu_0(b - a)M_\theta, \quad (3.34)$$

where L_0 is the linear inductance of the line in H/m, which for a coaxial line is:

$$L_0 = \frac{\mu_0}{2\pi} \ln \left(\frac{b}{a} \right). \quad (3.35)$$

From (3.34) the corresponding flux variation is given by:

$$\Delta\Phi = \frac{L_0\Delta I}{\Delta I} + \frac{\mu_0(b-a)\Delta M_\theta}{\Delta I} = L_0\Delta I + L_f\Delta I, \quad (3.36)$$

where L_f is the contribution to the inductance of the line arising from the reverse transition during the magnetization phase. Since the magnetic moment $\Delta M_\theta = 2M_s$ in gauss, the inductance L_f obtained from (3.36) must be adjusted by the factor 4π as:

$$L_f = \frac{\mu_0(b-a)\Delta M_\theta}{\Delta I}, \quad (3.37)$$

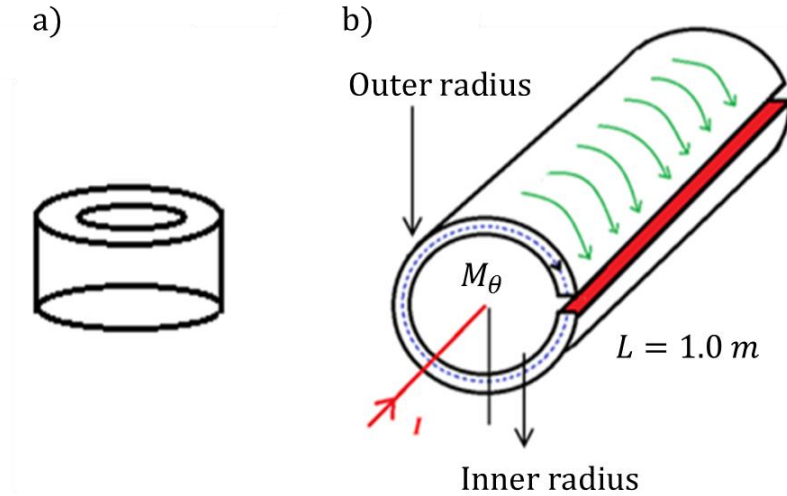
where $\Delta M_\theta = 8\pi M_s$ (gauss), then

$$L_f = \frac{32\pi^2(b-a)M_s}{\Delta I} \times 10^{-7} H/m, \quad (3.38)$$

where $\pi(b + a) = l$ is the average magnetic path. Equation (3.38) can be written as $L_f = \frac{32\pi^2(b-a)M_s}{H_\theta l} \times 10^{-7} H/m$. The radii a and b are given in meter. Since H_θ is the circumferential field caused by the current pulse I as:

$$H_\theta = \frac{\Delta I}{l} = \frac{I}{\pi(b+a)}. \quad (3.39)$$

Figure 3.18. Gyromagnetic line showing the a) Ferrite bead shape used in the b) Coaxial Line.



Source: Author's production.

The distributed resistance in the line during the magnetization phase can be calculated as:

$$^2R_f = \frac{\Delta\Phi_m/\Delta t}{\Delta I} = \frac{32\pi^2(b-a)M_s}{\tau\Delta I} \times 10^{-7}. \quad (3.40)$$

Using (3.26), (3.40) becomes:

² Taking into account that $\tau = \frac{s}{(H-H_c)}$, when $H_c \ll H$, than $\tau = \frac{s}{H_\theta}$, where $H_\theta = \frac{\Delta I}{\pi(b+a)} = \frac{\Delta I}{l}$. Replacing these values in the R_f equation, we have that $R_f = \frac{32\pi^2(b-a)M_s}{\frac{s}{H_\theta}H_\theta l}$. Once one includes the average magnetic path l in both parts of the fraction $R_f = \frac{32\pi^2(b-a)M_s l}{\frac{s}{H_\theta}H_\theta l^2}$. Thus, considering that $l = \pi(b+a)$, $R_f = \frac{32\pi^3(b-a)(b+a)M_s}{Sl^2}$.

$${}^3R_f = \frac{32\pi^3(b^2-a^2)M_s}{Sl^2} \times 10^{-7} \quad \Omega/m. \quad (3.41)$$

In the model proposed by Weiner [13] (3.38) and (3.41) represent the main equations, together with the linear inductance expression (given by (3.35)) and the linear capacitance given by:

$$C_0 = \frac{2\pi\varepsilon_0}{\ln\left(\frac{b}{a}\right)}, \quad (3.42)$$

where the linear capacitance is assumed to be constant during the reverse phase transition.

On the other hand, with initial axial magnetic bias field, it is possible to analyze in the LL [49] equation the magnetization vector in Cartesian coordinates, which provides:

$$\frac{\partial M_x}{\partial t} = \frac{\gamma}{1+\alpha^2} \mu_0 \left[M_y H_z - \frac{\alpha}{M_s} M_z H_z M_x \right] \quad (3.43)$$

$$\frac{\partial M_y}{\partial t} = \frac{\gamma}{1+\alpha^2} \mu_0 \left[-M_x H_z - \frac{\alpha}{M_s} M_z H_z M_y \right] \quad (3.44)$$

³ See in Appendix A.3 the detailed derivation of the Landau-Lifshitz equation in Cartesian coordinates.

$$\frac{\partial M_z}{\partial t} = \frac{\gamma}{1+\alpha^2} \mu_0 \left[-\frac{\alpha}{M_s} M_z^2 H_z + \alpha M H_z \right]. \quad (3.45)$$

The Z-component of the magnetic moment equation can be rewritten as:

$$\frac{\partial M_z}{\partial t} = -\frac{\gamma\alpha}{1+\alpha^2} M_s \mu_0 \left[1 - \frac{M_z^2}{M_s^2} \right] H_z \quad (3.46)$$

which has the same form of the magnetic moment in the circumferential magnetic bias given by (3.24).

3.5.2. Pouladian-Kari et al.'s Model

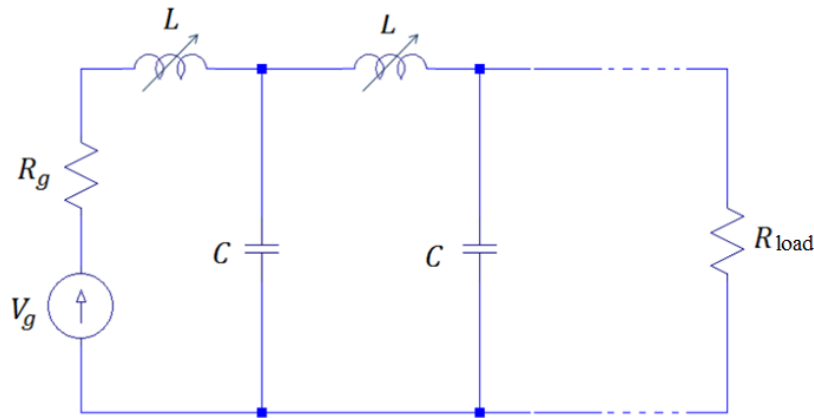
In 1989 a LC inductive nonlinear transmission discrete line was developed to model distributed gyromagnetic lines with reasonable success by Pouladian-Kari [14]. This model was used to calculate the reduction of the output pulse rise time caused by the permeability decrease in the line inductance. Figure 3.19 shows the equivalent circuit of this model, where the inductor is modeled by a nonlinear polynomial function (although other forms of modelling may be used such as exponential or hyperbolic tangent functions):

$$L(I) = L_0 - L_1 I - L_2 I^2 \dots . \quad (3.47)$$

However, due to the magnetic precession of the magnetic moment in ferrites, this model is not accurate as noted by Pouladian-Kari [14], because the exact

calculation of the compressed pulse rise time is affected when high-frequency oscillations (RF) generated by the magnetic precession are observed at the output of the line.

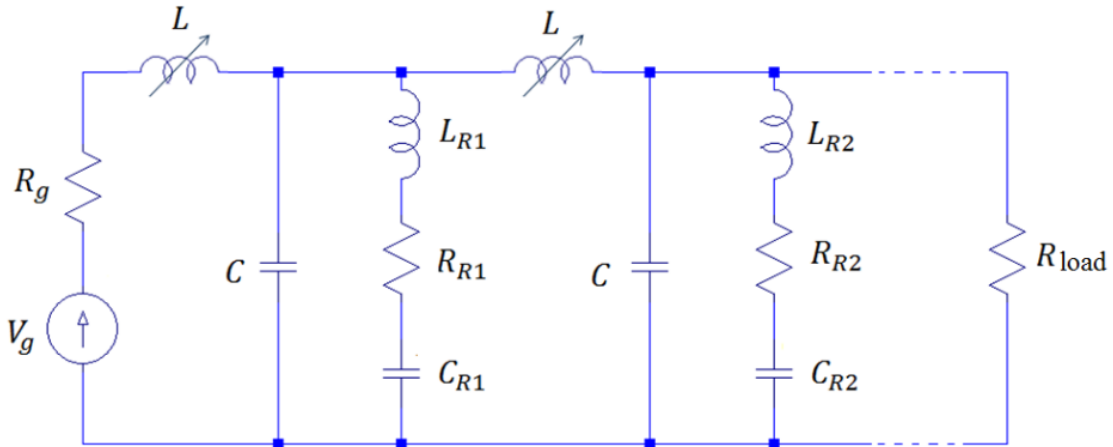
Figure 3.19. Model used by Pouladian-Kari to simulate the pulse compression in gyromagnetic lines.



Source: Author's production.

In fact, the model of Figure 3.19 takes into account that the ferrite permeability falls to extremely low saturation values ($\mu_r = 2 - 3$) depending on the current pulse applied onto the line, leading to rise time reduction of the order of hundreds of ps. The precession effect has been added by the inclusion of a RLC branch in parallel with the linear capacitance of the line at each section of the LC model as shown in Figure 3.20. The RLC values were adjusted to form a resonant circuit at the precession frequency of the ferrites. Since the precession depends on the total effective magnetic field applied, frequency tuning can be adjusted by varying the intensity of the axial magnetic bias field. In fact, precession frequency decreases with the axial bias field, but increases with the azimuthal field generated by the current pulse ($\omega \approx \gamma H_\theta$).

Figure 3.20. Complete Pouladian-Kari's model including the magnetic precession effect with constant magnetic bias.

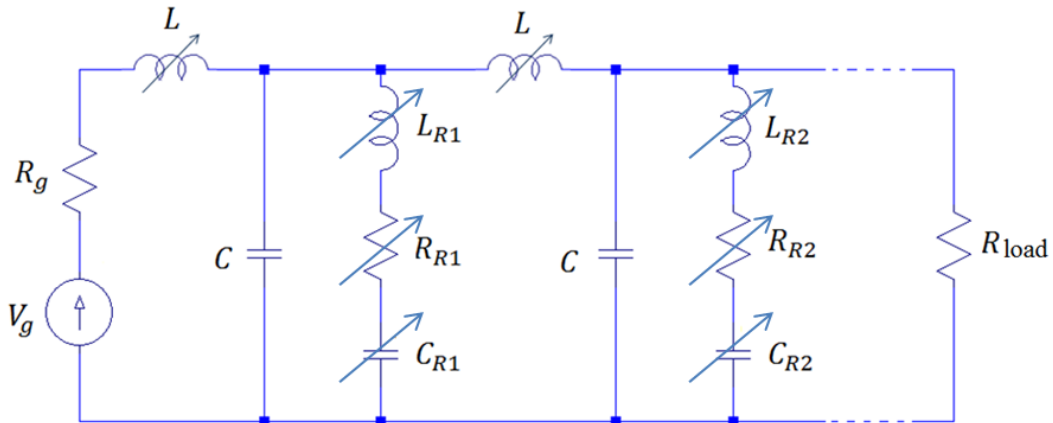


Source: Author's production.

3.5.3. Pouladian-Kari / Shapland's Model

This model [15] dated from 1991 is based on the same model developed by Pouladian-Kari et al. [14] described in the previous section. The novelty here is the use of variable values for the resonant branches placed in parallel with the linear capacitors for simulating a bias that increases linearly along the line. As precession frequency decreases with the axial field, it means that the RLC values should increase simultaneously along the line to represent a bias field that is higher along the line length. This aspect is represented by the varying RLC values in the scheme with linearly graded bias shown in Figure 3.21.

Figure 3.21. Complete Pouladian-Kari and Shapland's model including the magnetic precession effect.



Source: Author's production.

3.5.4. Dolan's Model

Dolan [16] pointed out that the model proposed by Pouladian-Kari et al. [14] and [15] does not include a direct representation of the magnetic precession in the ferrite, but only the resonant branches with values arbitrarily selected to produce a ferrite precession frequency observed at the output with determined damping rate, which in their view is an ad-hoc solution. Another problem is that at that time Pouladian-Kari's model was simulated using numerical methods since modeling nonlinear inductors in Spice circuit simulators was not an easy task because of the large line commands needed to emulate nonlinear components. In the case of Weiner's [13] and Pouladian's [14], [15] models, magnetic precession is not taken into account, since the azimuthal bias field only affects the pulse rise time. Thus, Dolan's model is suitable for the case with axial bias field because the modeling includes the LLG expression since the presence of the axial field is directly connected to the precessional motion of the magnetic moment. In this model the sources $V_1 - V_n$ represent the voltages (see Figure 3.22) induced along the line during the magnetization phase due to the change of the magnetic moment. In section m :

$$v_m = \frac{d\Phi}{dt} \Delta z = L_0 \frac{dI}{dt} \Delta z + \mu_0(b-a) \frac{dM_{\theta m}}{dt} \Delta z = L_0 \frac{dI}{dt} \Delta z + v_m \quad (3.48)$$

where $dM_{\theta m} = 2M_s$ and $\tau_m = dt$

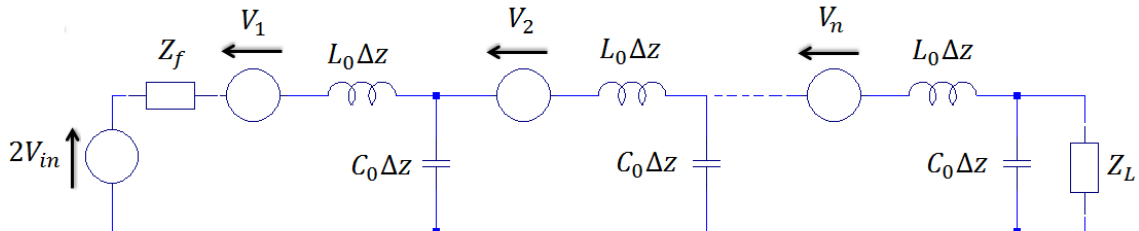
$$^4v_m = \mu_0(b-a) \frac{dM_{\theta m}}{dt} \Delta z = \mu_0(b-a) \frac{2M_s}{lS} I_m \Delta z \quad (3.49)$$

where b and a are the ferrite outer and inner radii, respectively, M_s is the magnetization of saturation, l is the magnetic average path, S is the switching constant, I_m is the average current, Δz is the length step used to make the line discrete $= l_c/n$, since L_0 and C_0 are given in H/m and F/m , respectively, l_c is the length of the coaxial line and n the number of sections (see the scheme in Figure 3.22).

It is important to highlight that ferrite loss can be taken into account in the simulation model in series with the component, if necessary. Dolan [16] used this model to simulate the output response of a line with azimuthal polarization (unidimensional), and also with axial field (three-dimensional). In the latter case (3D simulation), temporal variation of the magnetic moment along the Z axis was calculated using the initial angle θ_0 formed between M_θ and M_z during the application of the current pulse I , considering also the induced demagnetization field in the azimuthal and axial directions.

⁴ $v_m = \mu_0(b-a) \frac{dM_{\theta m}}{dt} \Delta z = \mu_0(b-a) \frac{2M_s}{\tau_m} \Delta z = \mu_0(b-a) \frac{2M_s}{S} H_{\theta m} \Delta z = \mu_0(b-a) \frac{2M_s}{lS} I_m \Delta z$

Figure 3.22. Model proposed by Dolan for simulation of the gyromagnetic line.



Source: Author's production.

3.6. Spice Circuit Simulations

With the advent of advanced circuit simulators with graphical user interface in the Windows environment, the idea of simulating gyromagnetics lines more easily using programs such as LT-Spice IV, in particular, has become attractive. A notable feature of this program is that a simple command can easily simulate the nonlinear inductance of the gyromagnetic line, where the inductance value is set in the program's command line through the corresponding flux equation associated with the inductor.

In this thesis we are proposing a new model based on Spice simulation since the previous models mentioned before were based on numerical simulation exclusively. For LT-Spice simulations, two different nonlinear inductance equations can be used. The first one developed by Kuek [50] models the nonlinear behavior of the inductor using a hyperbolic function as

$$L(i) = (L_i - L_s) \left[1 - \tanh^2 \left(\frac{i}{I_s} \right) \right] + L_s \quad (3.50)$$

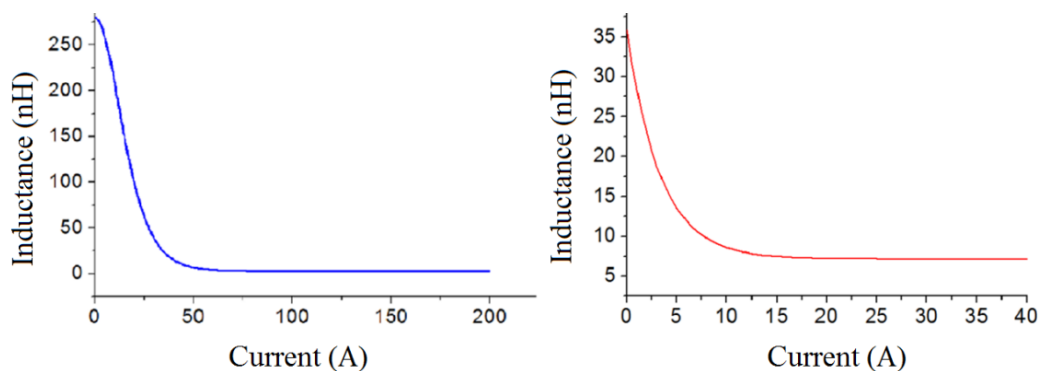
where L_i is the initial inductance of the line, L_s is the line inductance at saturation, i is the amplitude of the current pulse, and I_s is the saturation current of the ferrite. The second inductance equation, developed by Pouladian-Kari [14], uses another representation for the flux equation based on the NiZn ferrite's permeability and on an exponential function as

$$L(i) = L_s(1 + \mu_r e^{-\alpha i}), \quad (3.51)$$

where the constant $\alpha = \left(\frac{1}{I_s}\right)$ and μ_r is the relative permeability of the magnetic material.

It is important to know the variation of the inductance as a function of current, as shown by the curves in Figure 3.23 for a nonlinear magnetic material with ferrite cores, where equations (3.50) and (3.51) model the nonlinear behavior of the inductance since the inductance $L(I)$ decreases nonlinearly with the current.

Figure 3.23. Simulation of $L \times I$ curve of a nonlinear inductor using a) hyperbolic function and b) exponential function.



Source: Author's production.

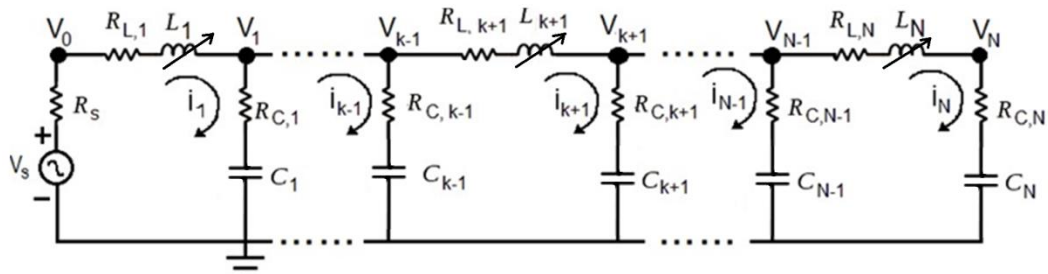
At a certain point, the inductor saturates, leading to the compression of the output rise time.

3.7. Numerical Analysis

An alternative way to simulate and study this type of transmission line is by means of numerical analysis. The circuit equations presented are based on the Kirchhoff's current and voltage laws. There will be presented the generalized circuit equations for the formulation: using $\{i(t), v(t)\}$ as state variables [67]. Considering each LC section, from the Kirchhoff's laws it is possible to obtain a system of equations for three sections: initial, intermediate and final, based on the general circuit from Figure 3.24.

For a general inductive LC line, considering the loss resistors in series with capacitors and inductors, it is possible to obtain (3.52) for the initial section, (3.53) for the intermediate section and (3.54) for the final section, being demonstrated as follows. It is important to highlight that all the equations were based on [67] considering the difference that in the original one the authors considered the nonlinear capacitor, while in this thesis the nonlinear component is the inductor.

Figure 3.24. Basic schematic for numerical analysis system.



Source: [67].

For the Initial Section, the corresponding equation is obtained taking into account the mesh with the voltage source, yielding (3.52) [67].

$$\frac{dI_k}{dt} = \frac{V_s}{L_k(i(t))} - \frac{R_s}{L_k(i(t))}(I_k) - \frac{R_{L,k}}{L_k(i(t))}(I_k) - \frac{R_{C,k}}{L_k(i(t))}(I_k - I_{k+1}) - \frac{v_k(t)}{L_k(i(t))}$$

$$\frac{dv_k}{dt} = \frac{I_k - I_{k+1}}{C}; k = 1. \quad (3.52)$$

In deriving equation (3.53) for the intermediate section, the mesh used is any from the middle of the line, which has the inductor, resistor in series with the inductor, capacitor, and resistor in series with the capacitor values as:

$$\frac{dI_k}{dt} = -\frac{R_{L,k}}{L_k(i(t))}(I_k) + \frac{R_{C,k-1}}{L_k(i(t))}(I_{k-1} - I_k) - \frac{R_{C,k}}{L_k(i(t))}(I_k - I_{k+1}) + \frac{v_{k-1}(t)}{L_k(i(t))} -$$

$$\frac{v_k(t)}{L_k(i(t))}$$

$$\frac{dv_k}{dt} = \frac{I_k - I_{k+1}}{C}; k = 2, 3, \dots, N - 1. \quad (3.53)$$

Lastly, equation (3.54) for the ending section includes the load resistance such as:

$$\begin{aligned} \frac{dI_k}{dt} &= -\frac{R_{L,k}}{L_k(i(t))}(I_k) + \frac{R_{C,k-1}}{L_k(i(t))}(I_{k-1} - I_k) - \frac{R_{C,k}}{L_k(i(t))}(I_k) + \frac{v_{k-1}(t)}{L_k(i(t))} - \frac{v_k(t)}{L_k(i(t))} \\ \frac{dv_k}{dt} &= \frac{I_k}{C}; k = N. \end{aligned} \quad (3.54)$$

3.8. Advantages of using Gyromagnetics Lines

The focus of this thesis on gyromagnetic NLTLs is due to the fact that this line is capable of generating stronger pulse oscillations at higher frequencies than dispersive lines. An advantage of the gyromagnetic line in relation to the dispersive dielectric NLTL is the stronger nonlinearity of the ferrite-based inductance when compared to that of the nonlinear lumped lines based on ceramic capacitors [11], [56], with less loss.

Gyromagnetic nonlinear lines may produce a very broad frequency spectrum starting from 600.0 MHz with RF conversion efficiency of about 10% and are currently exceeding frequencies of 3.0 GHz [64] for possible applications in satellite communications, where at least frequencies of this order of magnitude are required. Furthermore, nonlinear lumped LC lines have lower operating frequency around 1.0 GHz [8] in the case of inductive lines with saturable inductors being even worse in the case of capacitive lines, because of losses in the ceramic dielectric employed that limit their application up to 250.0 MHz. Although Seddon [8] has shown an approximate efficiency of 20% with LC lumped inductive lines at 1.0 GHz, surely the efficiency of dielectric LC lines is lower than 10% because of losses in the dielectric. In any cases, the results obtained so far with the use of nonlinear gyromagnetic lines have shown a

better performance than dielectric nonlinear lines as shown in Table 3.3 [8] and [67].

Table 3.3. Comparison of LC lumped dielectric and gyromagnetic lines.

| | LC lumped dielectric lines | Gyromagnetic lines |
|------------------------------|-----------------------------------|---------------------------|
| Conversion Efficiency | 1 - 20% | 10 - 40% |
| Minimum frequency | 1 MHz | 400 MHz |
| Maximum frequency | 300.0 MHz | 3.0 GHz |

Source: Author's production.

Thus, the research focus on this subject is of great interest, since computational simulations will be used as tools for line design before the line construction and subsequent experimental test.

3.9. State of the Art

The most recent papers (2014-2016) published on gyromagnetic nonlinear transmission lines are summarized and compared in Table 3.4 with their main characteristics. The first reference is dated from 2014 [69], and the authors used a spatially dispersive coaxial structure biasing the transmission line axially in order to provide high power and broad tuning range (from 0.95 to 1.45 GHz). The system had 60 sections with ferrite as the nonlinear element and used the shock velocity and the oscillation frequency to measure the line dispersion.

Another group from Ukraine National Science Center [70] studied the gyromagnetic line through experimental and numerical analysis in 2D, reaching an experimental frequency around 1.5 GHz for a line with 25.0 cm length.

The group from Tomsk [64] proposed the use of the NLTL delay sections for phase control in the case of a multichannel gyromagnetic line, because of the dependence of the velocity of the traveling shock rise time upon applied fields. Also the authors did not report in their experiments oscillations frequencies less than 400 MHz. In the experiments they observed that the delay grows with bias field up to 40.0 kA/m approximately when the delay starts to reduce as the bias field below this value is not intense enough to saturate the ferrite.

Johnson from Texas Tech in [71] performed the analysis of three different ferromagnetic materials to check the external biasing field influence on the delay time. All materials showed a general trend of decreasing delay time as the magnetic field bias is increased, but NiZn ferromagnetic material is optimal for achieving maximum phase delay.

Reale from Texas Tech recently in [72], taking into account the complexity of construction of coaxial lines, proposed a new geometry, a stripline. As the bias field and charge voltage increase, the center frequency also increases, because of the precession frequency dependence on the magnetic field in a gyromagnetic NLTL. The same group as shown in [73] described that the magnetic precession is essential for gyromagnetic line RF operation since without this effect, there are no oscillations observed. The magnetic moments at some point become aligned with the axial field, when precession motion stops because of the damping factor. The permeability of the material has a direct relation with the bias, affecting the propagation time of the line. In this manner, the longer the line is, the greater is the time delay. The distribution splitter divides the input pulse four ways and excites each line equally.

As observed in the above references (see comparison in Table 3.4), all the published works focused on the gyromagnetic line experimental design and results. In view of that, the search for alternative models to simulate these type of lines reinforces the contribution of this thesis as for the first time, a Spice simulation model was proposed for the design of such lines.

Table 3.4. Recent publications on Gyromagnetic Nonlinear Transmission Lines

| Paper | Group | Year | Type of line | Results |
|-------|----------------------------------------|------|------------------------------------------------------------------------------------|---------------------------------------------------------------------------------------------------------------|
| [69] | Air Force Research Laboratory (French) | 2014 | Experimental: spatially dispersive ferrite NLTL with axial bias | - Frequency tuning with the axial bias field adjustment from 0.95 to 1.45 GHz. |
| [70] | Ukraine National Science Center (Ahn) | 2015 | Experimental and numerical analysis: 1D and 2D | - Experimental frequency: 1.6 GHz - Line length: 25.0 cm |
| [64] | Tomsk (Romanchenko) | 2015 | Experimental: electronically controlled beam steering using two gyromagnetic lines | - Frequency: 0.5 – 1.7 GHz - 9.2% efficiency - 7.5 T |
| [71] | Texas Tech (Johnson) | 2015 | Experimental: different ferromagnetic materials | -NiZn is the optimal material -Magnetic field >, delay time < |
| [72] | Texas Tech (Reale) | 2016 | Experimental: new geometry proposal (stripline) | -15 kA/m magnetic field - Line length: 76.2 cm -Frequency: 771 MHz -Bias field ↑, center frequency ↑ |
| [73] | Texas Tech (Reale) | 2016 | Experimental: divides the input pulse four ways and excites each line equally | -Frequency: 2.0 - 4.0 GHz -1.0 kHz repetition rate - Line length: 76.2 cm |

Source: Author's production.

4. METHODOLOGY

In this work, Spice simulations on gyromagnetic lines have been carried out in the circuit simulator LT-Spice, version IV. For performance comparison between computational methods, a numerical simulation software (Mathematica) has been used just for Dolan's model. For best comparison of the results, output data from both softwares (Spice and numeric) have been exported to graphic software (Origin). For validation of the results, an experimental gyromagnetic line has been designed and tested. In summary, this thesis addresses two topics, circuit simulation and numerical analysis for the first one and experimental tests for the second.

4.1. Spice and Numerical Simulations

The Spice simulations have started with the circuit model developed by Weiner in 1989 [13], which includes ferrite losses, and the transmission line parameters, C and L, calculated on the basis of the physical mechanisms that provide the alignment of the ferrite magnetic moment with the magnetic field, as predicted by the LLG equation. Weiner did not test his proposed model via computational methods, but a check was made comparing the analytical calculations and experimental results, for example, for the pulse rise time variation as a function of the bias voltage source and the line length. The Weiner's [13] model main feature is that it is only used for calculating the output rise time with azimuthal polarization, without taking into account the axial magnetic polarization. In this case the Spice simulation can reproduce with reasonable accuracy the experimental results obtained by Weiner (as demonstrated ahead in the next chapter).

The second model reproduced is based on Pouladian-Kari et al. in 1989 [14], which mainly address the magnetic media nonlinearity due to the decrease in the magnetic permeability with the propagation of the current pulse through the

coaxial line conductor. The effect of precession motion on the pulse rise time is included in the model through a resonant RLC series circuit, as shown earlier in Figure 3.20. Although the RLC circuit values are selected arbitrarily to represent the precessional motion with frequency of oscillation ω and damping factor α , they have demonstrated that the numerical model is in good agreement with the experimental result. Thus, the goal of Spice simulations is based on the fact that it works quite well despite the precession effect has not been modeled according to the magnetic moment equation described by the LLG equation. The other model described by Pouladian-Kari / Shapland in 1991 [15] uses two types of magnetic bias: constant and linearly graded, where the component's values of the resonant branches changes along the line to represent the magnetic bias variation.

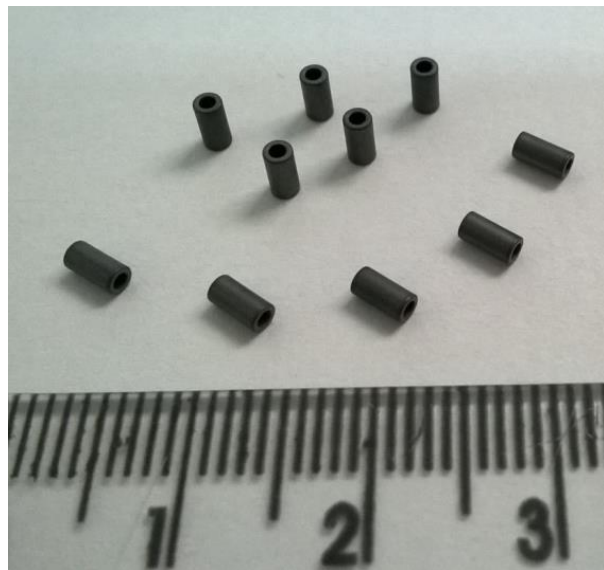
The last model studied was proposed by Dolan in 2000 [16], considered one of the most successful nowadays as it includes the axial magnetic bias in addition to the azimuthal field. In Weiner's model, only the azimuthal polarization is taken into account, while in Pouladian-Kari's [14], [15] model the introduction of the axial field is represented by RLC branches, which affects the precession frequency directly. On the other hand, Dolan's model is more precise because it includes the LLG expression, since in this case the axial field influence is directly connected to the precessional motion of the magnetic moment. Dolan's model can also include directly the ferrite losses, as in the case of modeling proposed by Weiner and/or Pouladian-Kari with the inclusion of the term R in the equivalent circuit in series with L . In fact, as we have seen, Dolan includes voltage sources in series with the saturated inductor at each line section, whose electromotive force is given by the variation of the magnetic moment M during the reverse transition interval time.

In short, the challenge herein was to implement the models described above using Spice simulation. This implementation and simulation results are discussed in the next chapter.

4.2. Line Design and Experimental Set-up

The coaxial gyromagnetic line is built by inserting ferrite beads through an internal conductor, where a tape sleeve is used to insulate the ferrite outer surface from the braiding. The first step for the line design is to calculate the saturated inductance in H/m given approximately by (3.35). Also, assuming $\epsilon_R = 1$ for the ferrite, the linear capacitance in pF/m was calculated by (3.42). The values used in simulations were based on the parameters and dimensions of the ferrite beads, where the line model has to be equivalent to the length of the line (20 cm in this case). For the simulation, the line has to be represented by a large number of LC sections. For the line construction, we used Amidon ferrite beads FB43201 of 3.8 mm length and with inner and outer diameters of 1.09 mm and 1.93, respectively (see Figure 4.1).

Figure 4.1. Ferrite beads

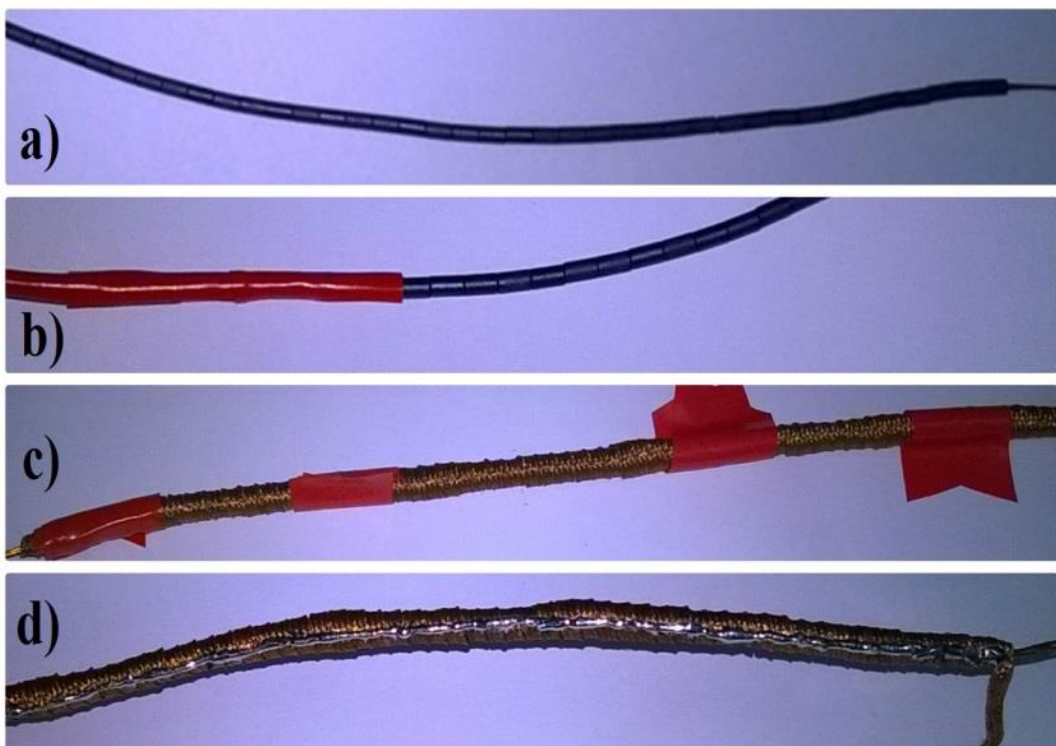


Source: Author's production.

To extend up to 20 cm across the length of the internal copper wire, 53 ferrite beads were placed side by side (see Figure 4.2 (a)) and their outer surface was

isolated from the braiding by two layers of insulating tape, forming a plastic sleeve (Figure 4.2 (b)). The braiding was built using a layer of flat metallic solder wire (CT-BRAND) made of copper of 2.5 mm width (Figure 4.2(c)). This setting was kept firmly in place by welding a thin layer of tin on the copper braiding (Figure 4.2 (d)). The total linear capacitance and inductance values measured in the coaxial line were 22.0 pF and 18.0 μ H, respectively using an LC meter, which gives an unbiased line impedance characteristic of about 900.0 ohms.

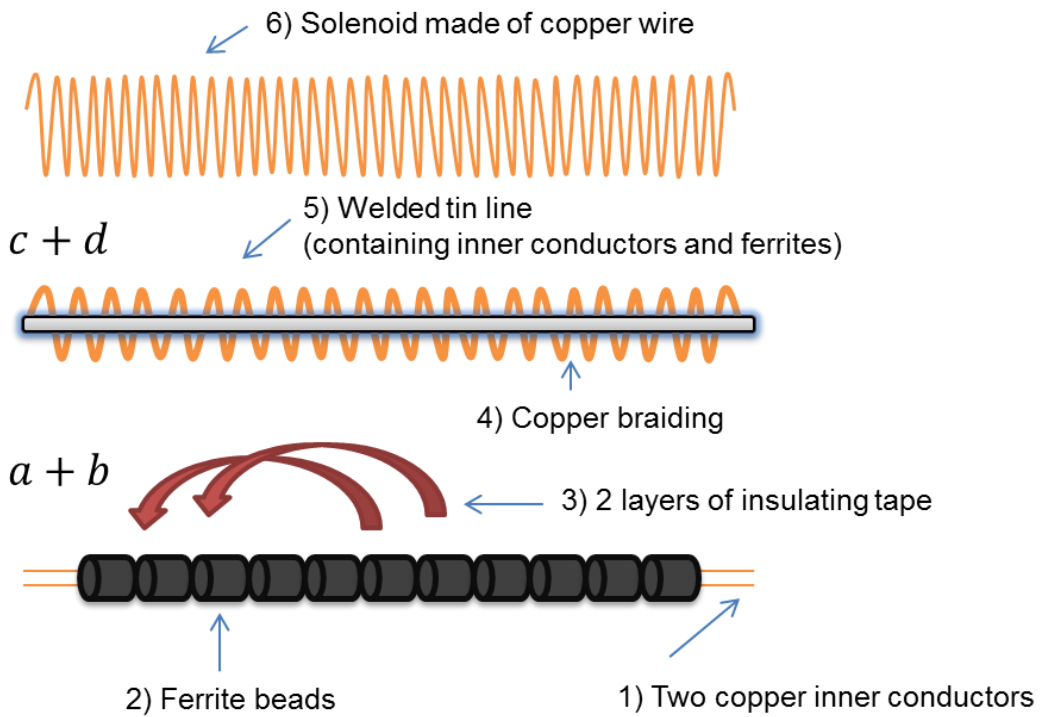
Figure 4.2. Construction steps of the coaxial line. a) copper wire inside the ferrite beads, b) insulating tape layer, c) solder wire layer, d) welded tin line.



Source: Author's production.

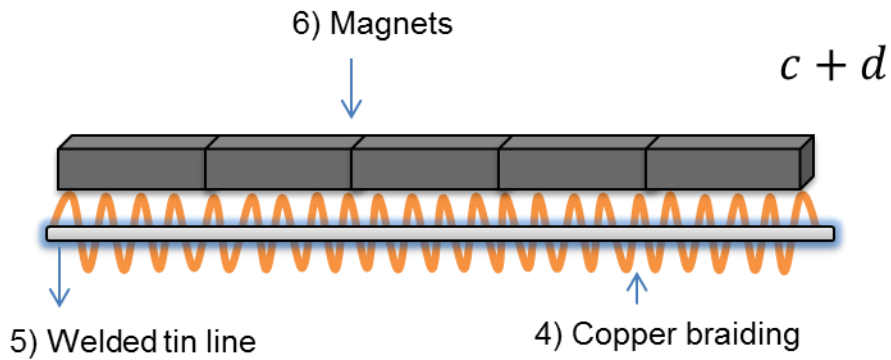
Figure 4.3 illustrates an expanded view of the coaxial line layers considering the system test using a solenoid while Figure 4.4 shows the final layers for the test using permanent magnets on top of the braiding.

Figure 4.3. Expanded view of the coaxial line assembly with solenoid.



Source: Author's production.

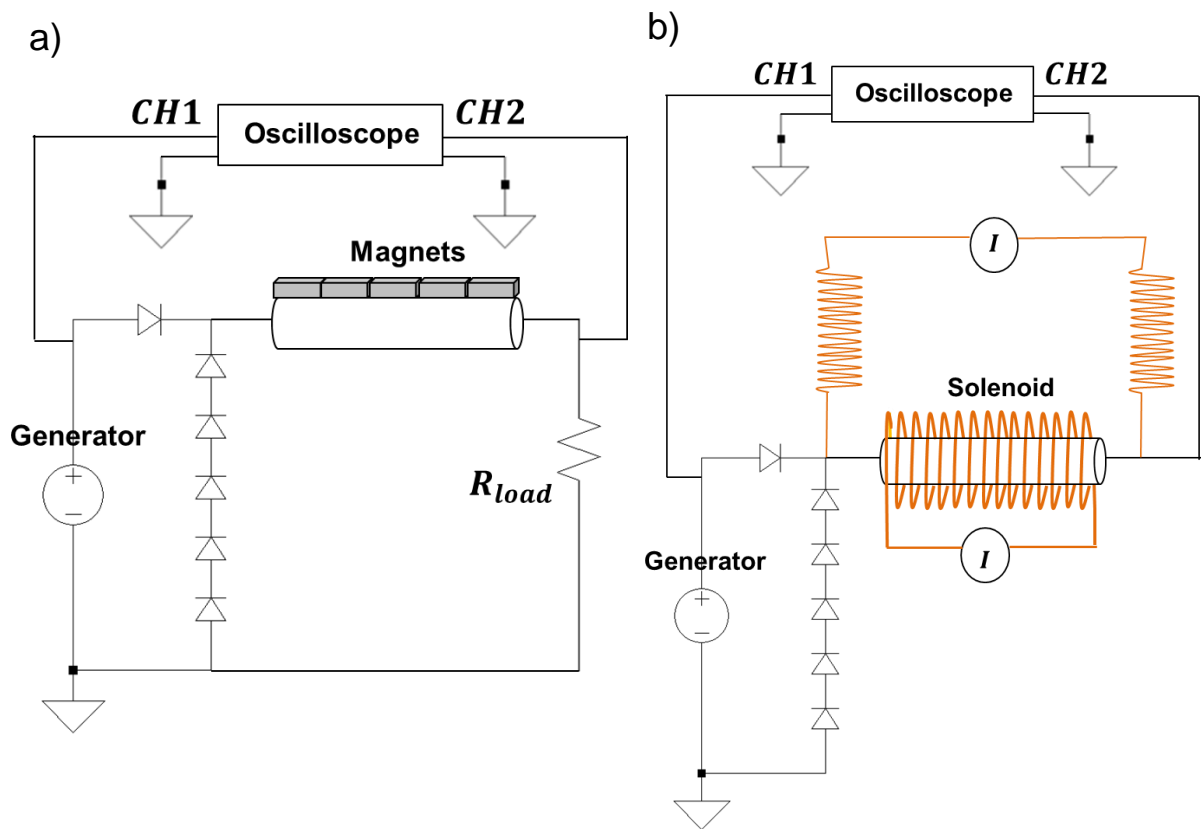
Figure 4.4. Final steps of the expanded view of the coaxial line assembly with permanent magnets.



Source: Author's production.

The first set-up of the experimental gyromagnetic line was completed by placing small pieces of permanent magnets over the extension of the coaxial line to produce the magnetic bias axial field as shown in Figure 4.5 (a). However, it has been verified experimentally that the use of permanent magnets is not enough to cause the magnetic precession because of the low axial H-field produced and, therefore a second set-up was built as shown in Figure 4.5 (b).

Figure 4.5. Teste set-up of gyromagnetic line (a) biases with permanent magnets (b) biased with a solenoid.

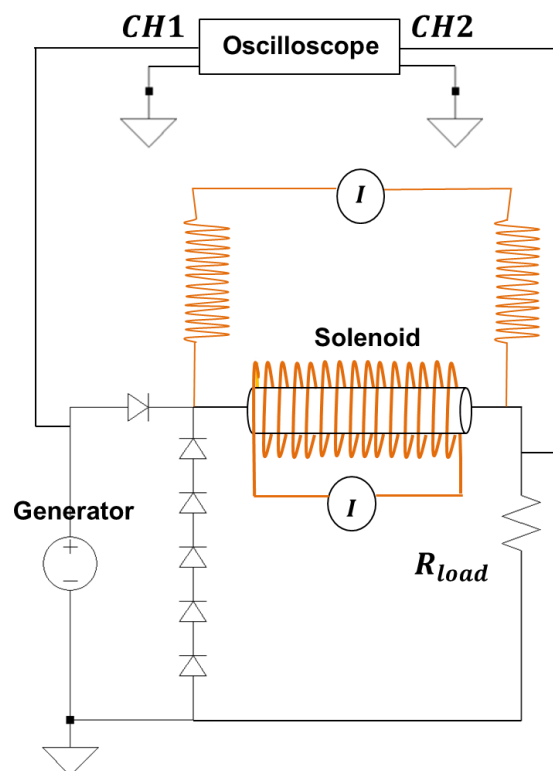


Source: Author's production.

Both Figures 4.5 (a) and (b) give the scheme employed to test the gyromagnetic line, showing the FID Technology 50 Ω HV fast pulse generator (model FPG5-1NM), diodes and load. In the scheme of Figure 4.5 (b) a stronger axial H-field

is generated by an external solenoid (with 220 turns) fed by a DC current source, which encloses the coaxial line axially. For better performance of the line at low voltage operation, we have also used an extra bias (azimuthal) provided by another DC current source to produce the axial current through the line inner conductor, being responsible for the formation of the azimuthal field. To isolate the high frequency input pulse injected onto the line from this second DC source, two extra solenoid windings (100 turns each) of high inductance are placed at input and output of the line and connected to the terminals of the DC source as shown in Figure 4.6.

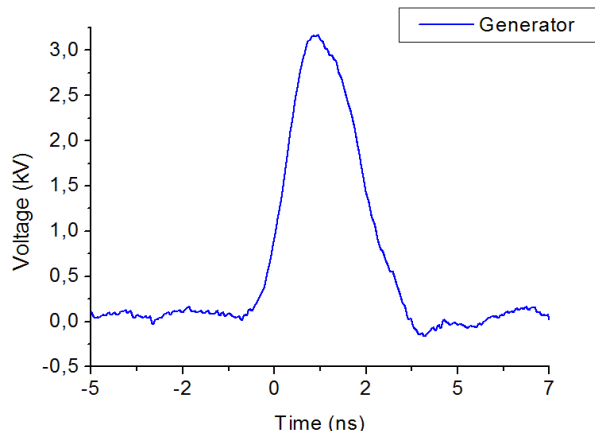
Figure 4.6. Scheme employed to test the gyromagnetic line with axial and azimuthal bias.



Source: Author's production.

Both signals at input and output were observed and extracted through a 4 kV/250 MHz Agilent probe linked to a 1.0 GHz digital scope from Agilent Technologies (model DSO9104A). The line was fed by the high voltage pulse generator FPS 5-1 NM, from FID Technology, capable of producing triangular pulses with amplitude varying in the range of 1.5 kV – 4 kV and with 2.5 ns of rise and fall times. Figure 4.7 gives the experimental output signal from the generator directly measured on a test load of 50.0Ω .

Figure 4.7. Generator signal on a 50Ω load termination.



Source: Author's production.

As a testing load, carbon resistors were used due to their small stray inductance since they have solid bulk for conducting the current instead of spiral as in the case of metallic resistors with higher inductance. Five power carbon resistors of $10.0 \Omega/3.0 \text{ W}$ were connected in series to provide a 50.0Ω load.

In order to protect the pulse generator output against reflections a BYW56 diode of 1.0 kV breakdown reverse voltage was used in series with the gyromagnetic line input. Another five diodes of the same model connected in series at the line input were used as free-wheeling diodes for generator protection (see Figures 4.5 (a) and (b)).

5. RESULTS AND DISCUSSIONS

In this chapter, the results obtained from models (Weiner, Pouladian-Kari, Pouladian-Kari/Shapland, and Dolan) implemented on Spice simulations will be presented. For Dolan's model, numerical and Spice simulation results are also compared. Lastly, experimental analysis of the gyromagnetic line are presented considering the coaxial line without any type of magnet bias, with the use of permanent magnets and with an axial bias produced by a solenoid.

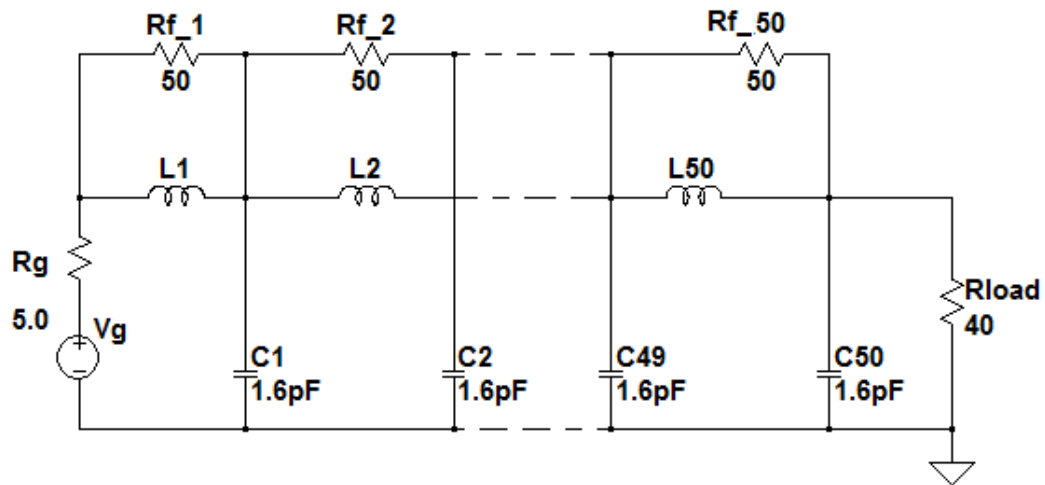
5.1. Weiner's Results Reproduced

In Figure 5.1 is shown the schematic⁵ of the simulated model based on Weiner's work, where it is important to highlight that ferrite loss can be taken into account in the simulation by including a resistor, if necessary, since R_f represents the bias field losses.

In order to obtain the same results in Spice as Weiner [13], it was necessary to adapt the circuit configuration as shown in Figure 5.1. Instead of placing the resistance R_f in series with the inductance, it was necessary to allocate this resistance in parallel because R_f represents the distributed resistance in the line during the magnetizing phase and not the ohmic losses of the inductor. In the Spice model, ohmic losses are represented by R_s in series with L and ferrite magnetic losses by R_f (already defined in (3.41) in parallel with L .

⁵ The nonlinear inductor is modeled by the flux equation $\text{flux}=(280\text{nH}-2.8\text{nH})*17.85*\{\tanh(x/17.85)\}+2.8\text{nH}^*x$. The schematic also contains linear capacitor of 1.6 pF, a load resistor of 40.0 Ω , a generator impedance of 5.0 Ω , and loss resistor in parallel with the nonlinear inductor of 50.0 Ω

Figure 5.1. LT-Spice schematic circuit used to reproduce Weiner's model.



Source: Author's production.

The discrete parameters for the LT-Spice LC ladder circuit used in simulations (Figure 5.1) are described in Table 5.1.

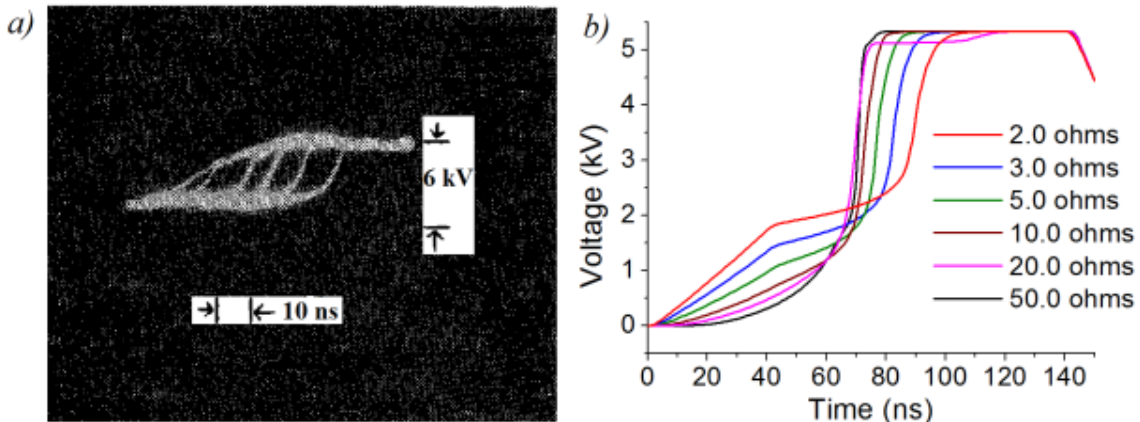
Table 5.1. Main parameters of Weiner's model.

| Parameter | Symbol | Value |
|----------------------|-------------|---------------|
| Initial Inductance | L_0 | 280.0 nH |
| Saturated Inductance | L_s | 2.8 nH |
| Linear Capacitance | C | 1.6 pF |
| Load Resistance | R_{load} | 40.0 Ω |
| Number of sections | n | 50 |
| Input Pulse | V | 6.0 kV |
| Input rise time | t_{ri} | 40.0 ns |
| Pulsewidth | $t_{on}(s)$ | 100.0 ns |

Source: Author's production.

One important characteristic of this model is that it addresses only pulse sharpening (output pulse rise time compression) using the azimuthal magnetic bias field, as in this case the gyromagnetic effect is negligible since the magnetic axial bias responsible for the precession effect is not present. Figures 5.2 (a) and 5.2 (b) show a comparison between the original result from Weiner [13] and the LT-Spice simulations obtained, respectively. In Figure 5.2 (b), it is possible to observe different rise times for corresponding R_f values. In fact, by increasing the azimuthal bias, R_f increases, and a progressive delay is introduced, which tends to decrease the initially long rise time with lower magnetic bias [13].

Figure 5.2. Experimental output voltage from the loaded ferrite line obtained from (a) Weiner's experiment varying azimuthal magnetic bias and (b) corresponding LTSpice simulations for several values of R_f .



Source: [13] and Author's production.

In this model R_f is the most important parameter in the rise time increase process since this resistance is calculated by means of the switch constant S which depends on the azimuthal field. Therefore, the azimuthal magnetic bias intensity is responsible for the variation of R_f in this model and, consequently,

for the rise time variation and line losses. The relation between the switching constant S and the azimuthal magnetic bias field can be explained by considering the switching time equation described in (3.26).

5.2. Pouladian-Kari et al.'s Results Reproduced

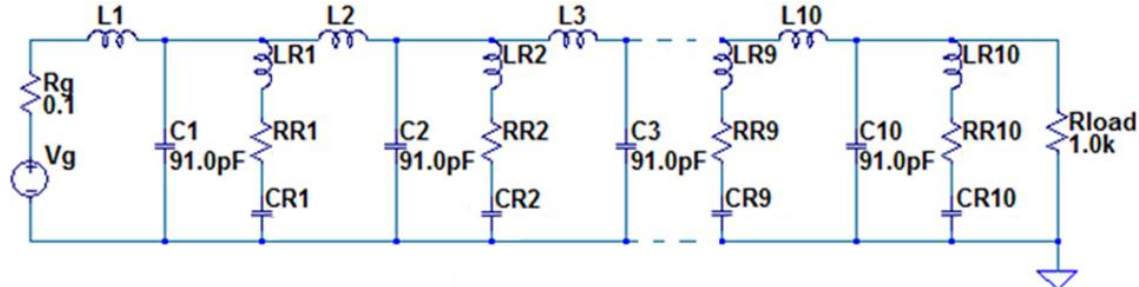
The second model to be studied is based on Pouladian-Kari et al.'s [14]. In this case the precession effect is taken into account by the inclusion of the RLC resonant branches in parallel with the linear capacitance of the line using two different configurations, further explained in the following sections.

5.2.1. Basic Model

The first Pouladian-Kari et al.'s configuration to be studied is based on the configuration where the values of the branches are the same for all the sections. The parameters used by Pouladian-Kari et al. [14] were a 64-cm long coaxial cable containing ferrite toroidal beads with approximate inner and outer diameters of 0.8 mm and 1.5 mm, respectively. The capacitance value per unit length was calculate using (3.42) and for the nonlinear inductor (3.35). As C_0 and L_0 are calculated per meter, the total values for L and C are just obtained by multiplying them by the line length. The basic schematic circuit for this model is shown in Figure 5.3.

The parameters for this reproduced model are listed on Table 5.2.

Figure 5.3. LT-Spice basic schematic circuit for Pouladian-Kari's model.



Source: Author's production.

Table 5.2. Main parameters of Pouladian's basic model.

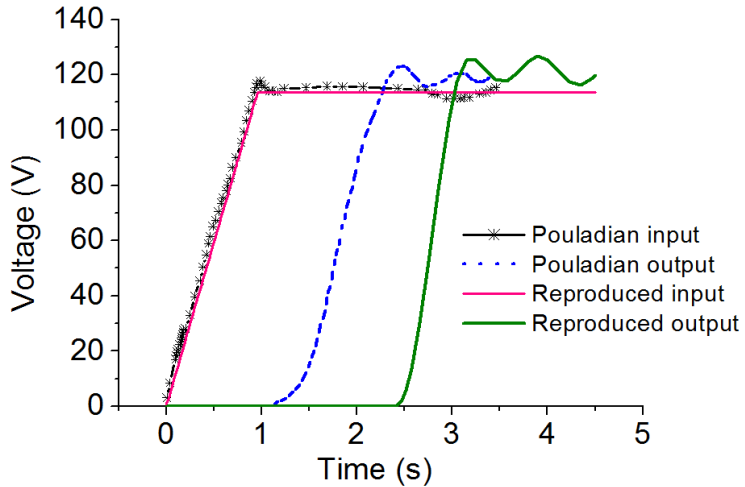
| Parameter | Symbol | Value |
|---------------------------|------------|----------|
| Saturated Inductance | L_s | 0.2 nH |
| Magnetic permeability | μ_r | 4.0 |
| Saturation current | I_s | 250.0 mA |
| Linear Capacitance | C | 91.0 pF |
| Load Resistance | R_{load} | 1.0 kΩ |
| Number of sections | n | 10 |
| Input Pulse | V | 10.0 kV |
| Input rise time | t_{ri} | 3.0 ns |
| Pulsewidth | t_{on} | 50.0 ns |
| Resistance of the branch | RR | 0.16 Ω |
| Inductance of the branch | LR | 1.0 nH |
| Capacitance of the branch | CR | 6.2 pF |

Source: Author's production.

First, the results obtained from LT-Spice simulations matched the Pouladian-Kari's simulations (see Figure 5.4), which confirms that the Spice model used is suitable for checking NTL performance. The original results [14] were based

on normalized values, and simulations for comparison purposes were performed in order to match the results.

Figure 5.4. Comparison of Pouladian-Kari's results.



Source: Author's production.

For the comparison with the original results given in [14], the horizontal and vertical scales in Figure 5.4 were normalized to 120.0 V peak and a 1.0 s rise time, which corresponds to 12.0 kV input pulse amplitude with 3.5 ns rise time. The values of the RLC components of the parallel branches were fixed at $LR=1.0\text{ nH}$; $CR=6.2\text{ pF}$; and $RR=0.16\Omega$. The difference between the line delays of the original and the reproduced model observed can be explained by the fact that Pouladian-Kari [14] considers the inductor flux varying linearly with time, while the reproduced model assumes flux varying nonlinearly with current. Appendix A.6 explains the flux modelling effect on line delay with more details.

For a deeper analysis of this model, the parameters were varied one by one to check the influence on the output signal. For this set of simulations, the shape of the input rectangular pulse was kept unchanged as the goal of this analysis is to observe the differences on the output pulse waveform produced by varying

the line parameters. For each simulation, only one line parameter was changed while keeping others unchanged (see Table 5.3) to observe the results of this variation on the line operation.

Table 5.3. Basic values for the varying parameters of Pouladian-Kari's model

| Parameter | Symbol | Value |
|-------------------------------|----------|----------|
| Magnetic permeability | μ_r | 4.0 |
| Saturation current | I_s | 250.0 mA |
| Input Pulse | V | 10 kV |
| Input rise time | t_{ri} | 3 ns |
| Pulsewidth | t_{on} | 50.0 ns |
| Resistance of the RLC branch | RR | 0.16 Ω |
| Inductance of the RLC branch | LR | 1.0 nH |
| Capacitance of the RLC branch | CR | 6.2 pF |

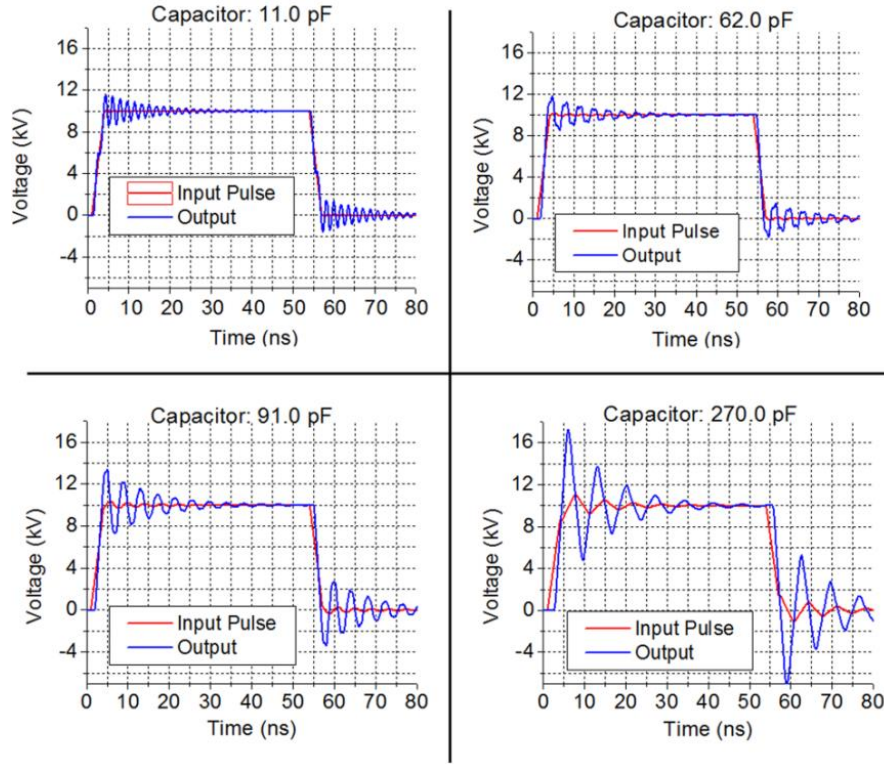
Source: Author's production.

The inductance nonlinearity was modeled using (3.51). Herein four results are presented for each line parameter varied, where the red line is the input pulse and the blue line is the output pulse. The y-axis corresponds to the voltage amplitude of the signals in kV, and the x-axis corresponds to time in nanoseconds. For all cases A, B, C and D the values of RLC for the parallel branches were fixed at L=1.0 nH, C=6.2 pF, and R=0.16 Ω.

5.2.1.1. Case A: Varying the Capacitor Values

The first simulation runs were performed for a 10-section line with linear capacitance set at 11.0 pF, 62.0 pF, 91.0 pF, and 270.0 pF, respectively, as seen in Figure 5.5.

Figure 5.5. LT-Spice simulation results using Pouladian-Kari's model for 11.0 pF, 62.0 pF, 91.0 pF and 270.0 pF linear capacitors, respectively.



Source: Author's production.

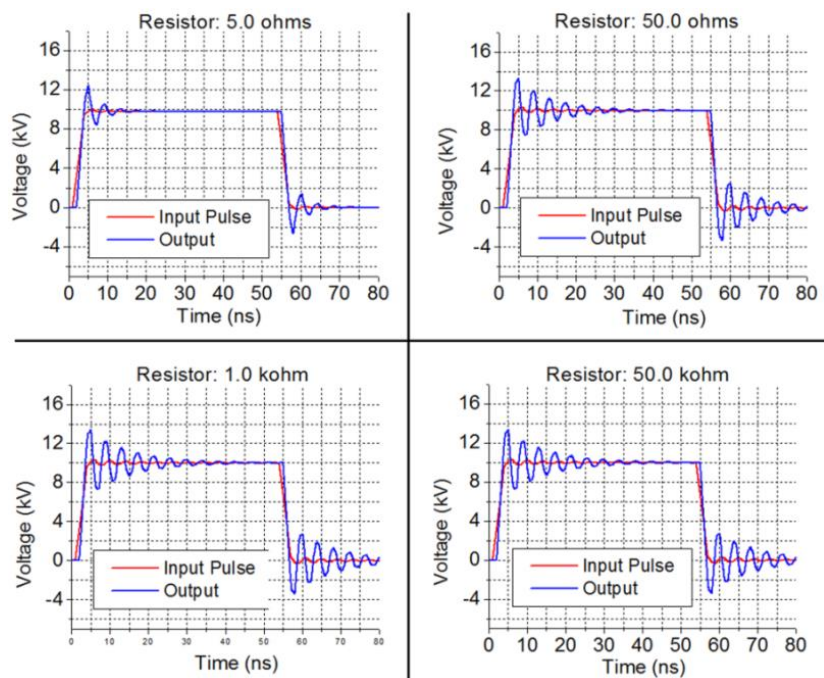
Other simulation parameters were: a) resistive load of $1.0 \text{ k}\Omega$, b) initial inductance of 0.9 nH , c) saturation inductance of 0.1 nH , and d) saturation current of 250.0 mA . Note that, when the capacitance increases, the oscillation peak increases but at a cost of decreasing output frequency. This is expected as the output frequency depends on the inverse of the squared root of LC.

Also observe that the time delay δ given by (3.4) increases with C as it is proportional to the squared root of LC. However, this effect is not clearly noticeable due to the time scale used and the low number of sections.

5.2.1.2. Case B: Varying the Load Resistance

For the load parameter variations, the solution was to run the simulation in small steps between 50.0 and $50.0\text{ k}\Omega$ for a 10-section line. Figure 5.6 gives the results for the following load values: $5.0\text{ }\Omega$, $50.0\text{ }\Omega$, $1.0\text{ k}\Omega$ and $50.0\text{ k}\Omega$. The remaining simulation parameters were: a) capacitor of 91.0 pF , b) initial inductance of 0.9 nH , c) saturation inductance of 0.1 nH , and d) saturation current of 250.0 mA .

Figure 5.6. LT-Spice simulation results using Pouladian-Kari's model for resistive loads of $5.0\text{ }\Omega$, $50.0\text{ }\Omega$, $1.0\text{ k}\Omega$ and $50.0\text{ k}\Omega$.



Source: Author's production.

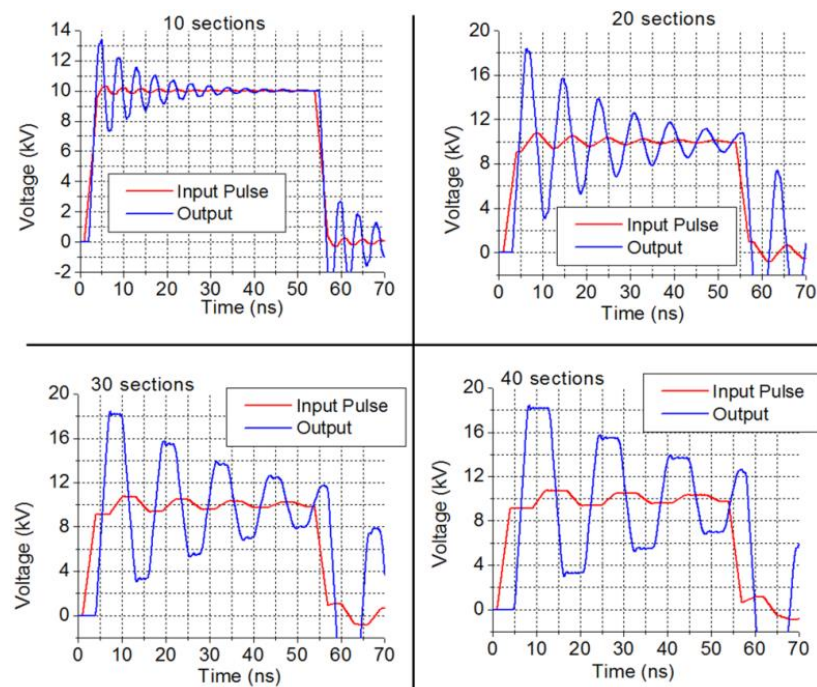
The main effect observed on the line performance is that the peak voltage increases as the load value increases up to $50.0\text{ }\Omega$ and remains practically the same above this value. Another aspect observed is that the oscillation frequency and the output rise time practically do not depend on the load. In fact, the rise time depends on the nonlinearity of the ferrite (or of the inductor) and the

dominant factor affecting frequency is the LC branch responsible for modeling the gyromagnetic effect.

5.2.1.3. Case C: Varying the Number of Sections

The number of sections was varied from $n = 10$ to 40 in steps of five sections and the results for $n = 10, 20, 30$ and 40 are presented in Figure 5.7, respectively.

Figure 5.7. LT-Spice simulation results using Pouladian-Kari's model for 10, 20, 30 and 40 sections.



Source: Author's production.

The other set of parameters were; a) a resistive load of $1.0 \text{ k}\Omega$, b) capacitor of 91.0 pF , c) initial inductance of 0.9 nH , d) saturation inductance of 0.1 nH , and

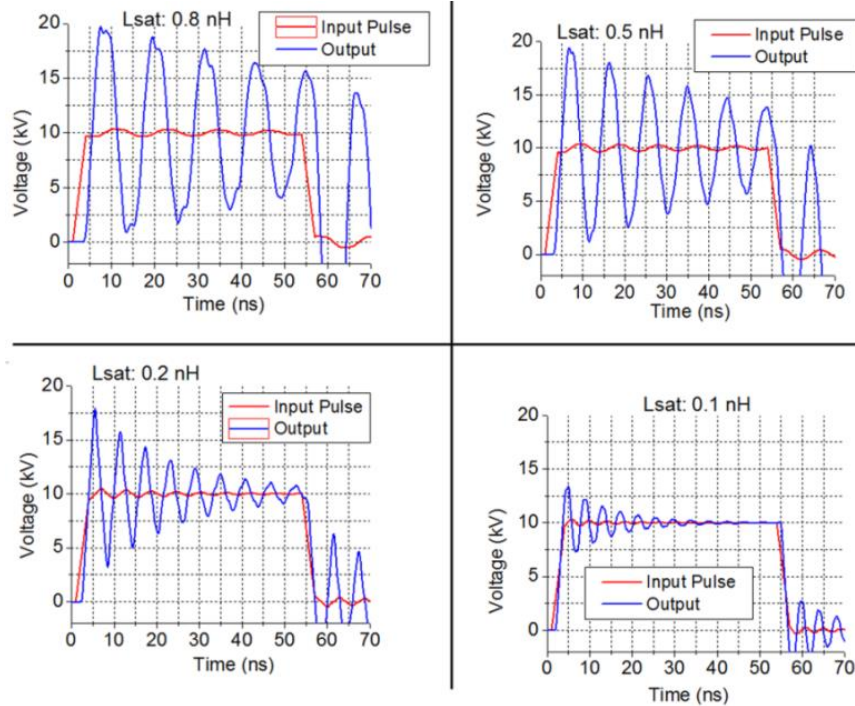
e) saturation current of 250.0 mA. Note that with 20 sections the amplitude peak of the output pulse reaches 18.0 kV and remains the same for 30 and 40 sections. On the other hand, as the number of sections increases, the frequency decreases and with 30 sections, the output oscillation becomes a distorted square waveform. The output rise time, however, remains the same.

5.2.1.4. Case D: Varying the Saturation Inductance

The value of the saturation inductance used in the flux equation (3.51) was varied from 0.8 nH to 0.01 nH in small steps in such a way that differences in the output waveform could be observed, with an initial inductance of 0.9 nH. The simulation run was performed for a 10-section line with a resistive load of 1.0 k Ω and linear capacitor set to 91.0 pF. Figure 5.8 shows the results for a saturation inductance of 0.8 nH, 0.5 nH, 0.2 nH, and 0.1 nH, respectively.

This is the most important parameter in Pouladian-Kari's model, since as the saturation inductance decreases, faster rise times and higher frequency oscillations are obtained, as expected. However, there is a limit at L= 0.01 nH, since for extremely low values of L the amplitudes of oscillations are compromised, being negligible, which is consistent with the observations made by Seddon [8]. As the saturation inductance decreases, oscillation amplitudes decrease with the line delay and pulse rise time becomes shorter, although this is almost imperceptible in the output waveforms of Figure 5.8. Thus, there is an optimum point where it is possible to observe several cycles of oscillations without compromising their amplitude. The saturation inductance has an optimum point at 0.2 nH for several cycles of oscillations for these simulations - this is the best choice for optimal NLTL performance for these parameters.

Figure 5.8. LT-Spice simulation results using Pouladian-Kari's model for saturation inductance of 0.8 nH, 0.5 nH, 0.2 nH and 0.1 nH, respectively.



Source: Author's production.

Pouladian-Kari [14] also reports that, although two identical lines contain the same ferrite material, they can give slightly different results in practice due to the effect of tolerance on the line parameters during the fabrication process. For example, the initial inductance, final inductance, and saturation current can vary from one line to another, and can have a strong influence on the line's output pulse. In summary in Table 5.4 is a comparison of all the parameters varied in this analysis.

Table 5.4. Comparison between the varying parameters

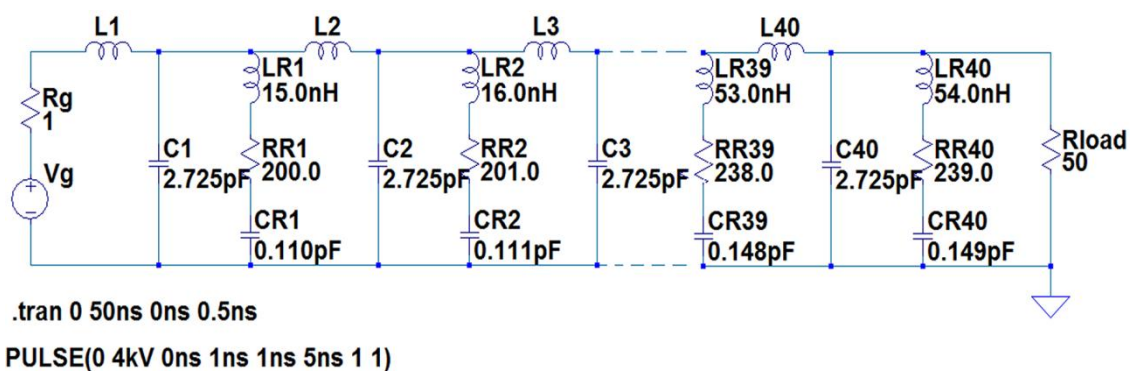
| Parameter | Symbol | Varying L_s | Varying C | Varying R_{load} | Varying n |
|-------------------------|---------------|----------------------------------------------|---------------------------------------------------|------------------------------------------------------------------|-------------------------------|
| A. Linear Capacitance | C | 91.0 pF | 11.0 pF 62.0 pF 91.0 pF 270.0 pF | 91.0 pF | 91.0 pF |
| B. Load Resistance | R_{load} | 1.0 $k\Omega$ | 1.0 $k\Omega$ | 5.0 Ω 50.0 Ω 1.0 $k\Omega$ 50.0 $k\Omega$ | 1.0 $k\Omega$ |
| C. Number of sections | n | 10 | 10 | 10 | 10 20 30 40 |
| D. Saturated Inductance | L_s | 0.8 nH 0.5 nH 0.2 nH 0.1 nH | 0.1 nH | 0.1 nH | 0.1 nH |

Source: Author's production.

5.2.2. Pouladian-Kari / Shapland's Results Reproduced

Simulations were also performed using a different Spice model for the line nonlinearity given by an exponential function according to (3.51). The simulation runs were fulfilled for a ferrite NLTL based on an improved Pouladian-Kari's model described elsewhere [15] with two different types of axial magnetic bias, constant and linearly graded. With a constant bias, the magnetic field is kept the same along the line axis while the graded magnetic field is varied linearly along the line axis. In the Spice LC model, the constant bias effect on the line is represented as a ladder as before by RLC branches with fixed component values. On the other hand, for the linearly graded bias the values of the RLC branches are varied along the line to simulate the magnetic linear variation along the axial length. For instance, Figure 5.9 shows the schematic of the LC ladder circuit model used in the LT-Spice simulation with a linearly graded magnetic bias.

Figure 5.9. LT-Spice simulation circuit model for a line with a linearly graded magnetic bias.



Source: Author's production.

The initial based parameters used in these simulations are summarized in Table 5.5.

Table 5.5. Main parameters of Pouladian / Shapland's model.

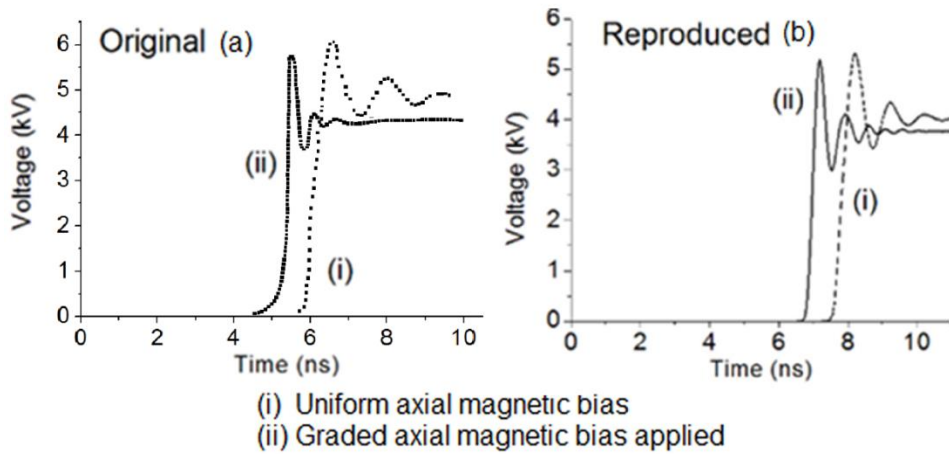
| Parameter | Symbol | Value |
|-----------------------------------|------------|---------|
| Saturated Inductance | L_s | 287 nH |
| Magnetic permeability | μ_r | 4 |
| Saturation current | I_s | 3.33 A |
| Linear Capacitance | C | 109 pF |
| Load Resistance | R_{load} | 50.0 Ω |
| Number of sections | n | 40 |
| Input Pulse | V | 4.0 kV |
| Input rise time | t_{ri} | 1.0 ns |
| Pulsewidth | $ton(s)$ | 5.0 ns |
| Initial Resistance of the branch | RR | 200.0 Ω |
| Initial Inductance of the branch | LR | 15.0 nH |
| Initial Capacitance of the branch | CR | 0.11 pF |

Source: Author's production.

Figures 5.10 (a) and (b) show a comparison between the line output waveforms with (i) constant magnetic bias, and (ii) linearly graded magnetic bias, obtained from a numerical software given in [15] and from the LT-Spice circuit simulation.

In Figure 5.10, one can observe that the line with linearly graded axial magnetic bias produces faster rise time of the output pulse with oscillations of lower amplitude while that with constant magnetic bias generates oscillations with higher amplitudes on the output pulse of slower rise time. Both original and the obtained LT-Spice simulations are similar, but again they show a discrepancy on the line delay due to the different approaches used for the flux modeling as explained before (Appendix A.6).

Figure 5.10. Constant and linearly graded bias a) Original b) Reproduced.



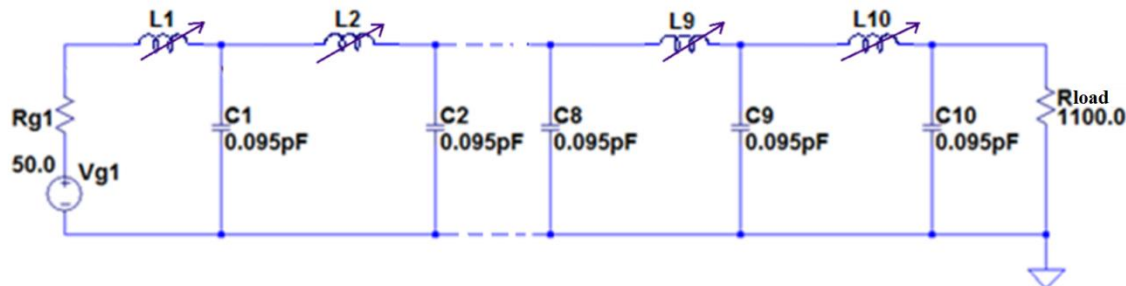
Source: [15] and Author's production.

5.3. Dolan's Results Reproduced

In Dolan's model [16], the schematic of the circuit includes a voltage source in series with the inductor, as shown in Figure 3.18. One interesting aspect about this configuration is to ensure the nonlinear behavior of the circuit, i.e., voltage source as the nonlinear element. In our case, as the equation of the inductance flux is used as the input command in LT-Spice simulation rather than the inductance value, the nonlinear behavior is considered altogether. Therefore, there was no need to include the voltage source in our simulation as illustrated by the LT-Spice schematic⁶ Figure 5.11. The parameters values used in the simulation are in Table 5.6.

⁶ The magnetic flux through the inductors is given by (3.50) with $L_0 = 465 \text{ nH}$, $L_S = 4,65 \text{ nH}$, and $I_S = 3,76 \text{ A}$.

Figure 5.11. Circuit basic scheme of LT-Spice for Dolan's model.



Source: Author's production.

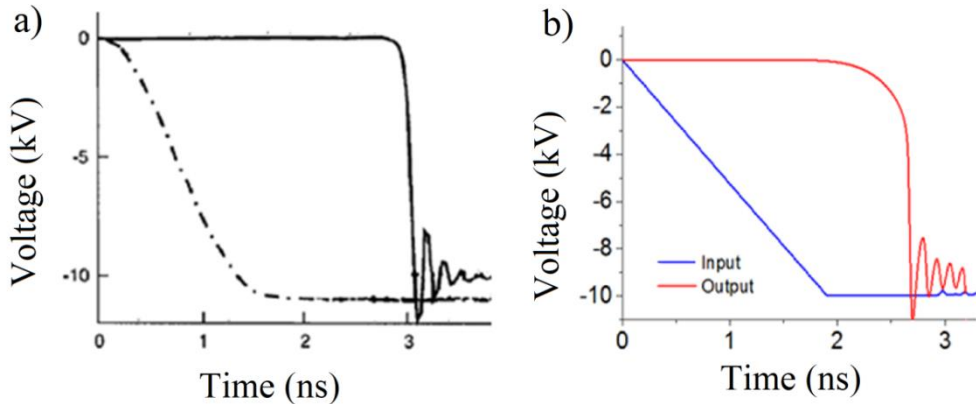
Table 5.6. Main parameters of Dolan's model.

| Parameter | Symbol | Value |
|-----------------------|------------|-----------------------|
| Saturated Inductance | L_s | 4.65 ns |
| Magnetic permeability | μ | $4\pi \times 10^{-7}$ |
| Saturation current | I_s | 3.76 A |
| Linear Capacitance | C | 0.095 pF |
| Load Resistance | R_{load} | $1.1 \text{ k}\Omega$ |
| Number of sections | n | 10 |
| Input Pulse | V | -10.0 kV |
| Input rise time | t_{ri} | 1.7 ns |
| Pulsewidth | $ton(s)$ | 10.0 ns |

Source: Author's production.

In fact, it was possible to find the same result obtained from the original model given in Figure 5.12 (a) with the reproduced waveform of Figure 5.12 (b).

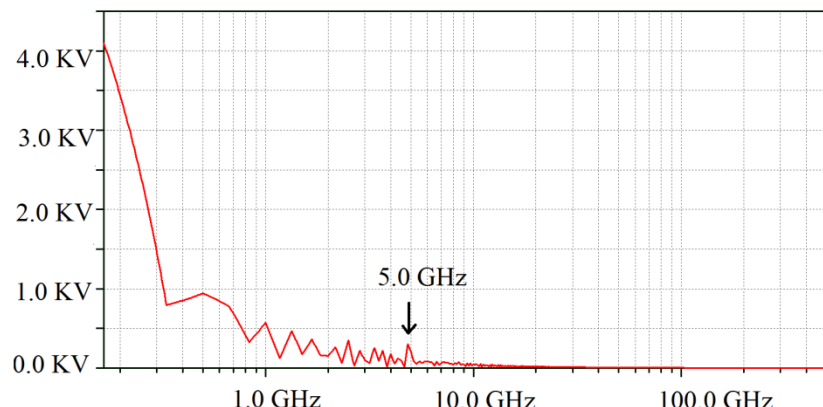
Figure 5.12. Response of Dolan's model a) Original b) Reproduced



Source: [16] and Author's production.

As observed in Figure 5.12 b), the pulse sharpening on the trailing edge was predicted correctly by the LT-Spice model (compare the input pulse rise time in blue with the output pulse rise time in red). Besides that, for Dolan's model as demonstrated by the Fast Fourier Transform spectrum from simulations (see Figure 5.13), oscillation frequencies of about 5.0 GHz were generated.

Figure 5.13. Output Fast Fourier Transform from simulated Dolan's model.

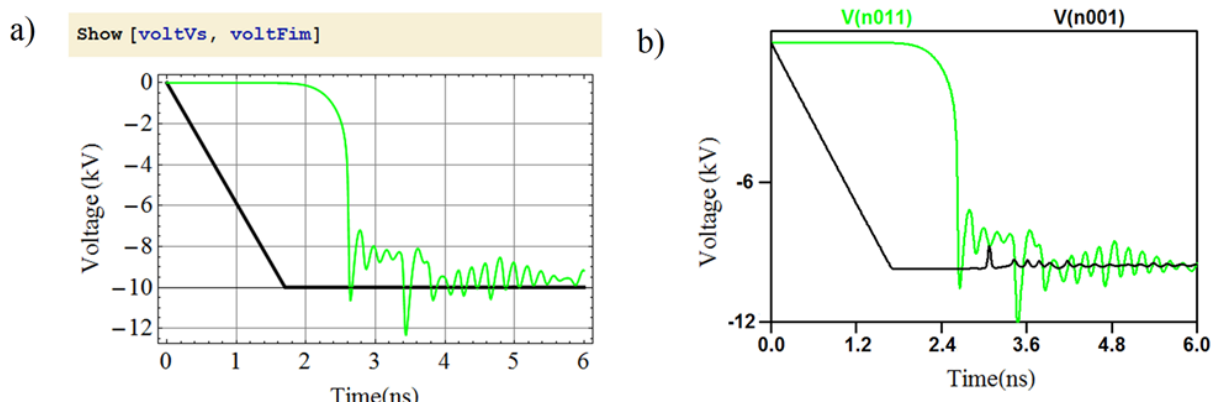


Source: Author's production.

5.4. Numerical Analysis

As mentioned at the beginning of this chapter, Dolan's model was also reproduced by means of numerical analysis in order to validate the equations and the simulated model. Using equations (3.50), (3.51) and (3.52) and the input commands for the line parameters, one can reproduce the same results by means of numerical analysis using the Mathematica software (see Appendix B for the detailed code) as shown in Figure 5.14 (a) where in black is the input pulse and in green is the output generated. For comparison, Figure 5.14 (b) shows the corresponding LT-Spice simulation with the same parameters used in the numerical simulation.

Figure 5.14. Dolan's results reproduced a) Numerical analysis model using Mathematica software, and b) Circuit simulation model using LT-Spice.



Source: Author's production.

By comparing Figures 5.14 (a) and 5.14 (b), one can observe an excellent agreement between the results using numerical analysis (Mathematica) and circuit simulation (LT-Spice), demonstrating that both methods are efficient for the study of this type of transmission line, which validates the model. Each one has its advantages and drawbacks. For example, the LT-Spice is easier to

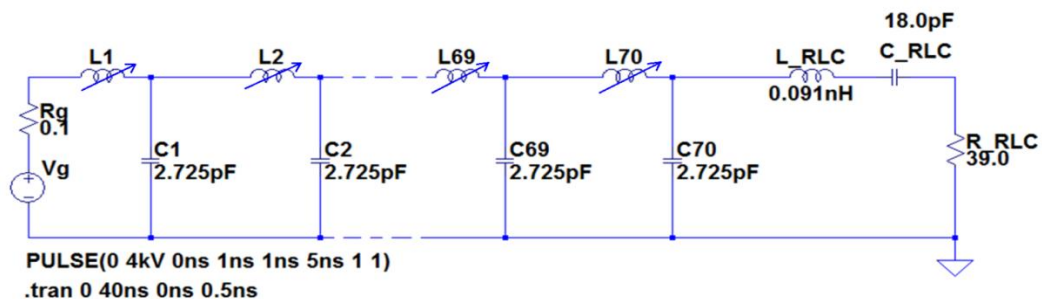
implement, but for a great number of sections it is harder to change the parameters on each line section as well as to add a great number of sections. On the other hand, with Mathematica it is harder to write the code, which takes more time. However, once implemented the code is simpler and faster to do any change on the circuit parameters to run the simulations.

5.5. Our Proposal of a New Topology Based on a Reactive Load

Based on the previous Dolan's model analyzed, we propose a new technique aimed at a frequency generation above 1.0 GHz and excellent Voltage Modulation Depth (VMD). This proposed model was simulated on LT-Spice.

With the goal of obtaining a more satisfactory VMD, the original number of sections was increased from 40 to 100 in steps of 5 with a RLC reactive load to check a reasonable VMD. This was based on the Marksteiner [74] work who proposed a solution, using a reactive load instead of a resistive one at the end of the line, providing a better modulated signal. The circuit test can be verified in Figure 5.15, with the reactive load, being $L=0.091\text{ nH}$, $C=18.0\text{ pF}$ and $R=39.0\Omega$.

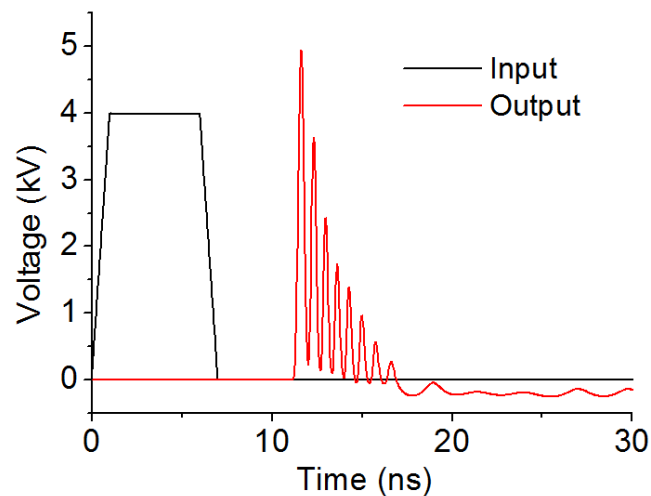
Figure 5.15. LT-Spice simulation schematic with reactive load.



Source: Author's production.

For this specific simulation, it was found that an optimum value of sections was 70. The input pulse in black and the output pulse in red are observed in Figure 5.16. The main line parameters for this simulation were based on Pouladian-Kari's model given in Figure 5.9 ($L_S = 7.175 \text{ nH}$, $\mu_r = 4$ and $I_S = 3.33 \text{ A}$).

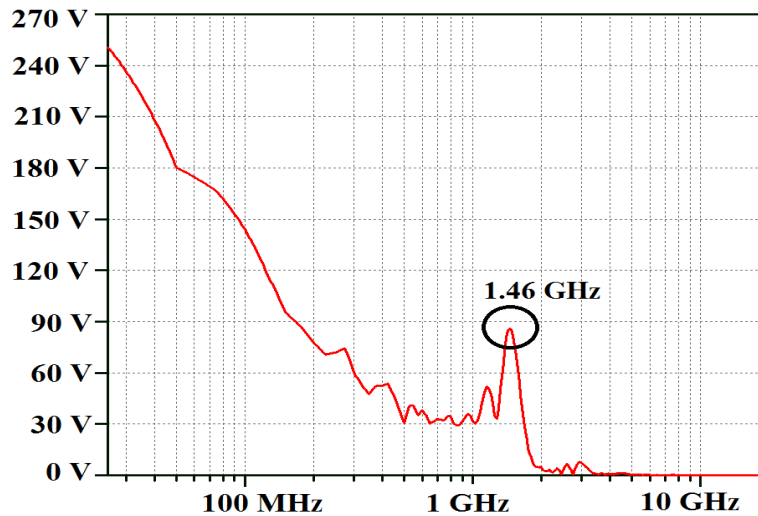
Figure 5.16. Input and output of the model with reactive load.



Source: Author's production.

Observe the depth related to the peaks and troughs of the oscillations on the output pulse. Also, an excellent output pulse rise time compression (0.35 ns) was obtained when compared to the input pulse rise time (1.0 ns). With FFT representation of the output signal in Figure 5.17 it is possible to observe that the maximum oscillation frequency reached 1.46 GHz.

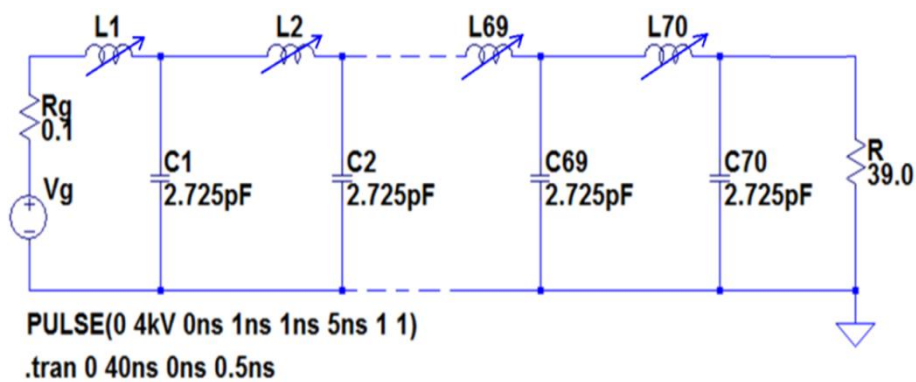
Figure 5.17. Output pulse FFT of the simulation with reactive load.



Source: Author's production.

In order to have a comparison with the reactive load case, the Spice simulation with resistive load using the same parameters of Figure 5.15 was performed. In this case, the load resistance of 39.0Ω was kept according to the scheme presented in Figure 5.18.

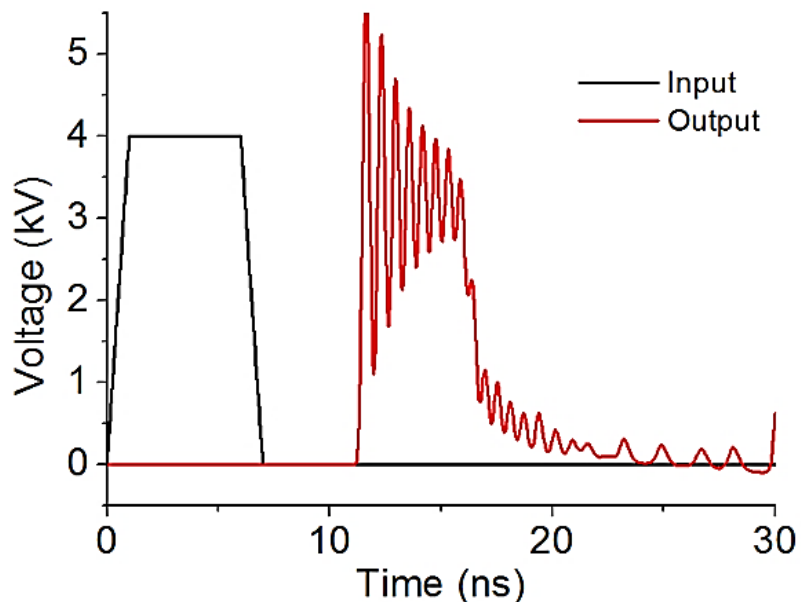
Figure 5.18. Simulation schematic with resistive load.



Source: Author's production.

Observe the input pulse in black and the output pulse in red shown in Figure 5.19. By comparing the output signal in Figure 5.19 to the corresponding one in Figure 5.16 it is noticed that there is a difference between the depths of the peaks, being deeper in the scheme with reactive load than in the case with resistive load. Also, in this case an excellent pulse compression is obtained since the output pulse rise time of about 0.35 ns is faster when compared to the input pulse rise time of 1.0 ns.

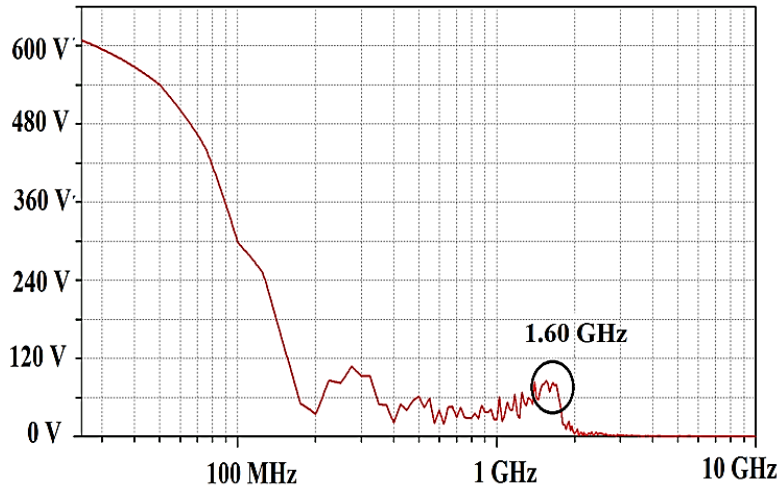
Figure 5.19. Input and output of the model with resistive load.



Source: Author's production.

With FFT representation of the output signal in Figure 5.20, it is possible to observe that the maximum oscillation frequency reached 1.60 GHz approximately.

Figure 5.20. Output pulse FFT of the simulation with resistive load.



Source: Author's production.

The comparison between both models shows that the one with reactive load has better voltage modulation depth (VMD) with lower frequency whereas with resistive load the model has the opposite behavior, i.e. lower VMD and higher frequency.

5.6. Experimental Validation

In order to validate the simulated Spice model proposed here in this thesis, experimental analyses of the gyromagnetic line were performed, including the characterization of the inductance L variation in relation to the current I. First, tests considered the coaxial line without any type of magnet bias to check just the line nonlinearity influence on the output rise time. After this, tests with magnetic axial bias using permanent magnets or a solenoid were made. To check the results, Spice simulations were performed for comparison with the experimental results obtained for the case using permanent magnets, validating our Spice model as planned. The value measured with the magnetic flux (H)

using permanent magnets was ≈ 477.46 A/m, while with the axial bias and azimuthal magnetic fields were respectively ≈ 6.88 kA/m and ≈ 39.78 A/m.

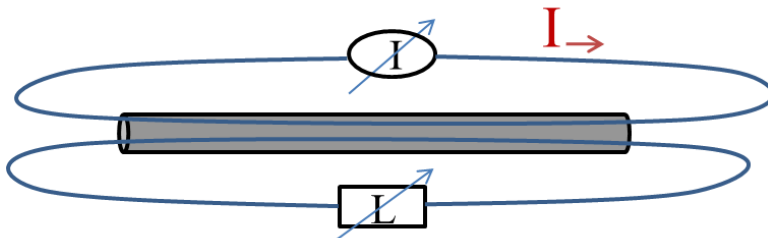
5.6.1. Characterization of L x I Curves

Considering different configurations for the coaxial line characterization, this subsection presents the bias and experimental assembly to measure the line inductance variation as function of the applied current (L x I curve) for three different cases. In Figure 5.21 is shown the assembly for all three cases, where in case 1 (Figure 5.21 (a)) with azimuthal bias, the line inner conductor is connected directly to the current pulse. In case 2 (Figure 5.21 (b)), for this measurement the same arrangement is made, but with six permanent magnets placed on the top of the coaxial line. Finally, in case 3 (Figure 5.21 (c)), the coaxial line is put inside the solenoid fed by the current pulse.

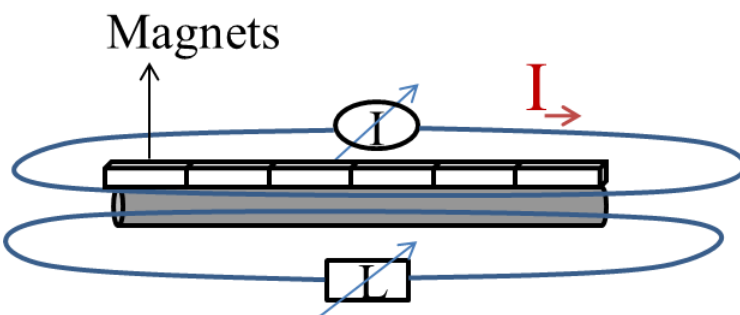
For cases 1 and 2, a DC variable current source was used to apply the current into the line varying from 0.0 to 10.0 A while for case 3 the same source was used to feed the solenoid for a current variation between 0.0 and 20.0 A. For the three case measurements shown in Table 5.7, an inductance meter was connected between the line input and output endings.

Figure 5.21. Assembly for coaxial line characterization (a) Case 1: Azimuthal bias, (b) Case 2: Bias with magnets, and (c) Case 3: Axial bias.

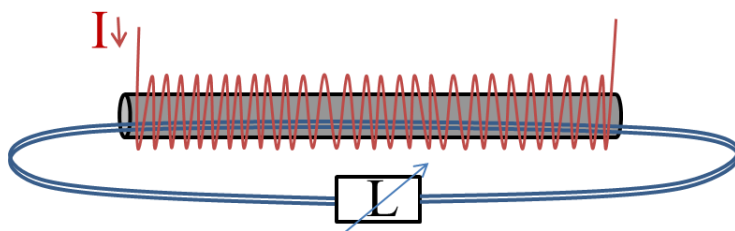
a) Case 1



b) Case 2



c) Case 3



Source: Author's production.

Table 5.7. Values of the inductance varying according to the applied current for (a) Case 1: Azimuthal bias, (b) Case 2: Bias with magnets, and (c) Case 3: Axial bias.

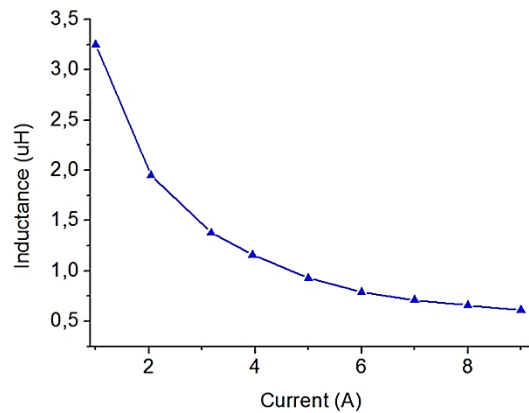
| (a) Case 1 | | (b) Case 2 | | (c) Case 3 | |
|-------------------|--------------|-------------------|--------------|-------------------|--------------|
| I(A) | L(μH) | I(A) | L(μH) | I(A) | L(μH) |
| 0.00 | 15.5 | 0.00 | 3.16 | 0.00 | 18.45 |
| 1.00 | 3.25 | 1.09 | 1.41 | 4.54 | 15.00 |
| 2.04 | 1.95 | 2.13 | 1.11 | 7.32 | 10.45 |
| 3.17 | 1.38 | 3.17 | 1.05 | 9.00 | 8.09 |
| 4.00 | 1.22 | 4.22 | 0.94 | 12.19 | 5.65 |
| 5.00 | 0.93 | 5.26 | 0.89 | 12.54 | 5.57 |
| 6.00 | 0.84 | 6.30 | 0.85 | 15.32 | 4.66 |
| 7.00 | 0.71 | 7.00 | 0.83 | 17.41 | 3.57 |
| 8.00 | 0.66 | 8.05 | 0.81 | 20.00 | 3.24 |
| 9.00 | 0.61 | 9.09 | 0.79 | 20.54 | 2.88 |

Source: Author's production.

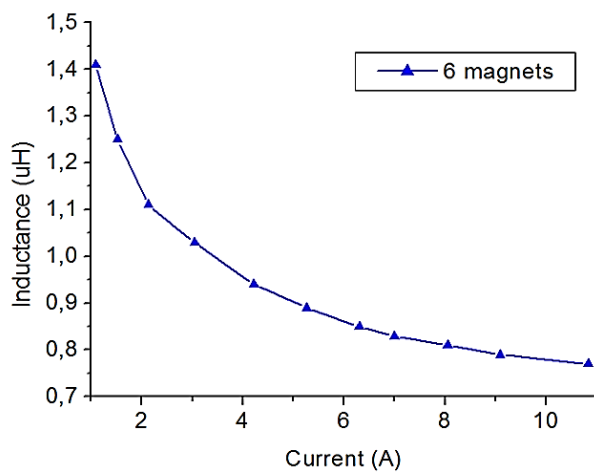
Figure 5.22 shows the $L \times I$ curves for the three cases. In case 1 (Figure 5.22 (a)) with the azimuthal bias, saturation occurs at a current of about 6.0 A for a measured inductance around 0.84 μH. For case 2 (Figure 5.22 (b)) with the use of permanent magnets, the saturated inductance is of the order of 0.81 μH and was measured at a current of 8.05 A. For case 3 with the solenoid arrangement (Figure 5.22 (c)), the inductance of saturation starts at 3.57 μH with higher current (above 17.41 A approximately). All three graphics presented in Figure 5.22 illustrate the nonlinear behavior of the line inductance with increasing current with more than 99% of inductance variation.

Figure 5.22. L x I curves for (a) Case 1: Azimuthal bias, (b) Case 2: Bias with magnets, and (c) Case 3: Axial bias.

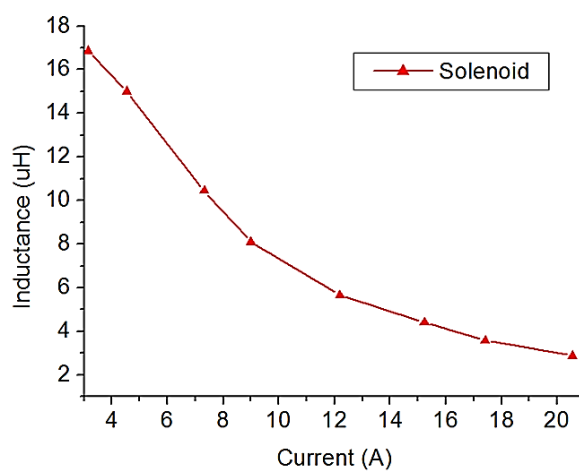
a) Case 1



b) Case 2



c) Case 3

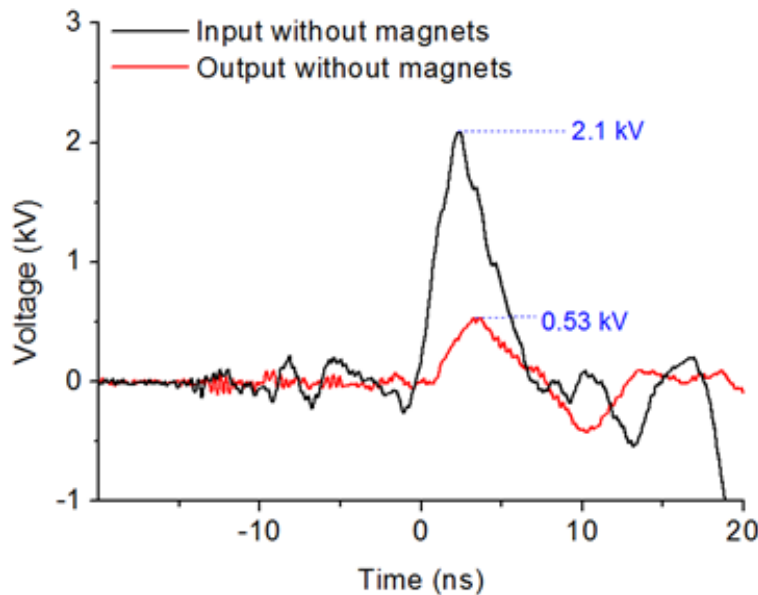


Source: Author's production.

5.6.2. Experimental Line Operation without Bias

For comparison with the biased cases, Figure 5.23 displays the output and input voltages without any magnetic bias. In this figure, one can see that there is a line delay of approximately 2.0 ns between pulses as expected and a considerable drop of peak amplitude of about 1.6 kV for the output pulse due to line losses and reflection as the line is not matched to the load because of the nonlinearity.

Figure 5.23. Input and output of the coaxial line without magnets.

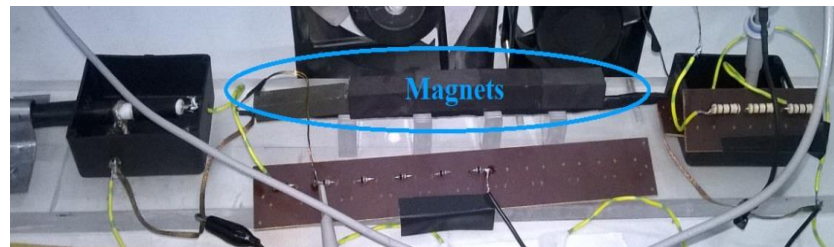


Source: Author's production.

5.6.3. Experimental Line Operation with Permanent Magnets

For line operation with axial magnetic bias without any DC current source, six permanent magnets with transversal square section of $1.5 \times 1.5 \text{ cm}^2$ and length 3.5 cm were placed side by side along the line (on top) as shown in Figure 5.24.

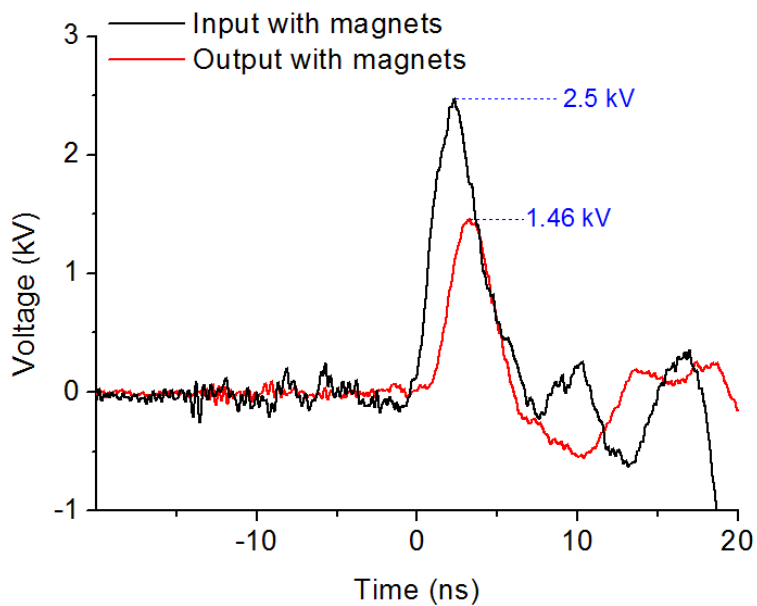
Figure 5.24. Several magnets placed along the coaxial line (on top).



Source: Author's production.

Figure 5.25 shows the results (input and output pulses) obtained with the set-up given in Figure 5.24. It is possible to observe an improvement in the output pulse compared to operation without bias, which demonstrates the considerable magnetization influence on line performance as in this case the output rise time is shortened and the peak amplitude relative to the input is increased.

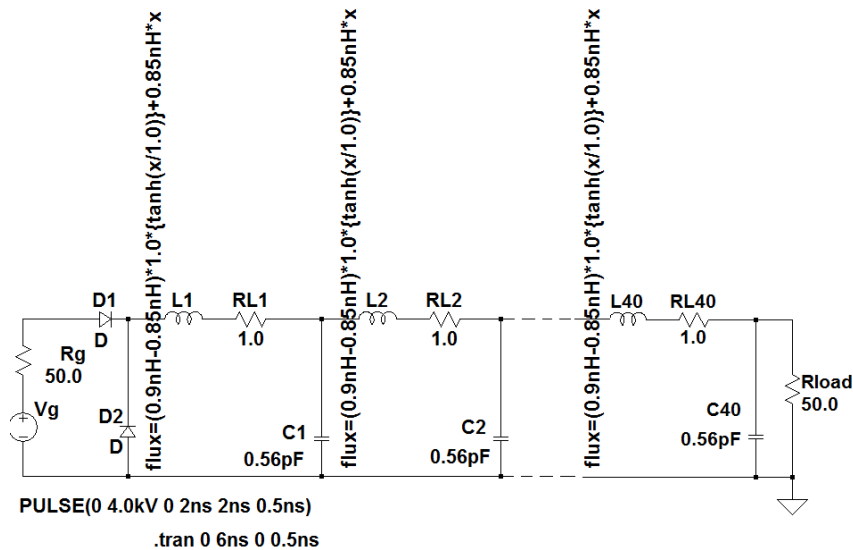
Figure 5.25. Input and output pulse using permanent magnets as external bias.



Source: Author's production.

In order to validate the Spice gyromagnetic simulation proposed and described in this thesis, the circuit model with the same parameters as the coaxial line built and biased with magnets was reproduced (see corresponding scheme in Figure 5.26).

Figure 5.26. Spice scheme used to simulate the gyromagnetic line with magnets.

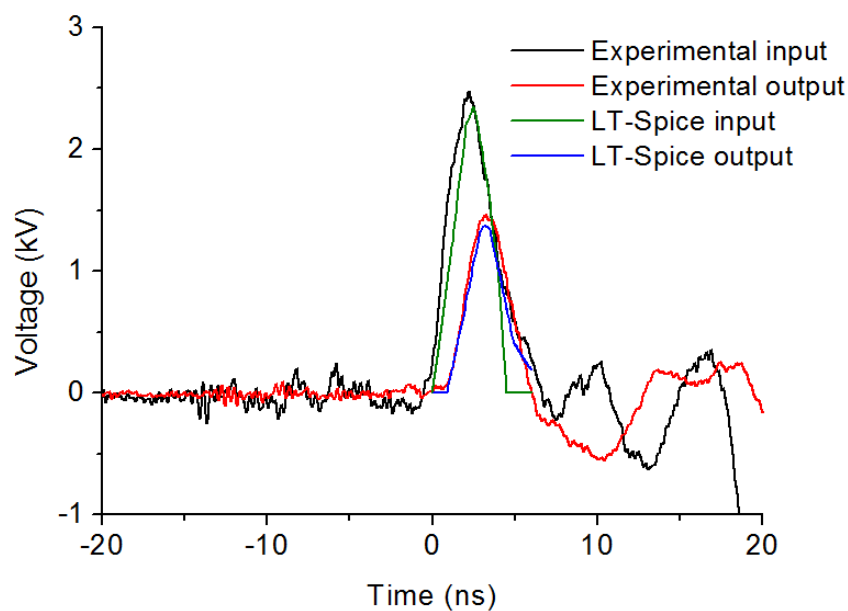


Source: Author's production.

In the simulation, the generator output impedance and load are fixed at 50.0 ohms according to the experimental parameters. The input pulse simulated has the same specification according to the experimental result in Figure 5.25. The values of the saturated inductance (0.85 nH) and the capacitance (0.56 pF) were calculated according to (3.35) and (3.42), based on the ferrite and line dimensions already described. The initial inductance in the flux equation displayed on the schematics was adjusted so that the simulations are fitted to the experimental results since the ferrite relative magnetic permeability drops when the permanent magnets are placed along the line ($\mu_r=160$). Also, in the scheme of Figure 5.26, the resistance of 1.0 Ω in series with the line inductance

represents the ferrite losses. A comparison between the experimental results of Figure 5.25 and the corresponding simulations obtained from schematics in Figure 5.26 is given in Figure 5.27, showing good agreement and thus proving the viability of using the Spice circuit model proposed.

Figure 5.27. Comparison between experimental result using magnets and Spice circuit model.



Source: Author's production.

5.6.4. Experimental Line Tests with Axial and Azimuthal Bias at Low Voltage Operation

The picture of the set-up line configuration proposed in Figure 4.6 in Chapter 4.2 to study the magnetic precession with two magnetic biases applied simultaneously is shown in Figure 5.28. One important aspect about this configuration for low voltage operation is that the tests were performed with open terminals because with the use of the load the rise time is too long and it

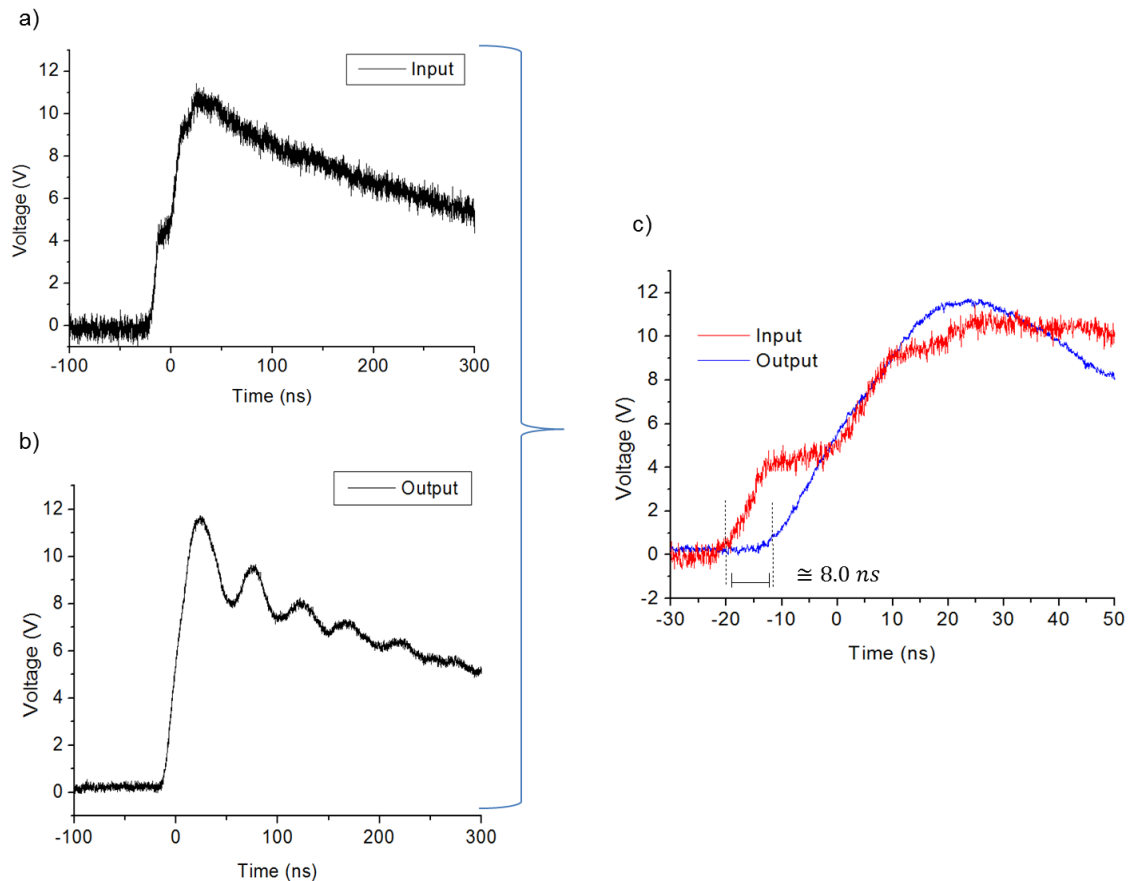
is harder to observe the gyromagnetic effect on the line. The line was fed by a pulse from a low voltage generator (TTI-model TGP-110) with 10 V of input amplitude and 300 ns width using axial and azimuthal biases fixed at 7960 A/m and 148 A/m, respectively. The corresponding values of the current set at the DC sources and the magnetic field intensities in A/m with the respective formulation are shown in Table 5.8. Figure 5.29 (a) shows the applied input pulse with a rise time of less than 100 ns. On the output pulse in Fig. 5.29 (b), it is possible to observe the compressed rise time of less than 50 ns with a series of oscillations of considerable voltage modulation caused by the magnetic precession effect. The input and output pulses displayed together on a short scale in Fig. 5.29 (c) show the small delay line of about 7 ns, which gives a decreased line inductance of about 3 μ H at a fixed total line capacitance of the order 22 pF due to the use of both magnetic biases that lowers the initial ferrite magnetic permeability.

Figure 5.28. Experimental assembly with axial and azimuthal bias for low voltage operation.



Source: Author's production.

Figure 5.29. Experimental results of the line with axial and azimuthal biases at low voltage operation (a) Input pulse, (b) output pulse and (c) both pulses on shorter scale.



Source: Author's production.

Table 5.8. Axial and azimuthal biases at low voltage operation.

| Formulation | Current (I) | Magnetic field (H) |
|-------------------------------------------------------------------|---------------------------------|----------------------------------------|
| $H_Z = NI/79.6l$ with $N = 220$ and $l = 0.2m$ | 8 A | 7960 A/m |
| $H_\theta = I/79.6\pi d_{mean}$ with $d_{mean} = 1.51 \text{ mm}$ | 0.7 A | 148 A/m |

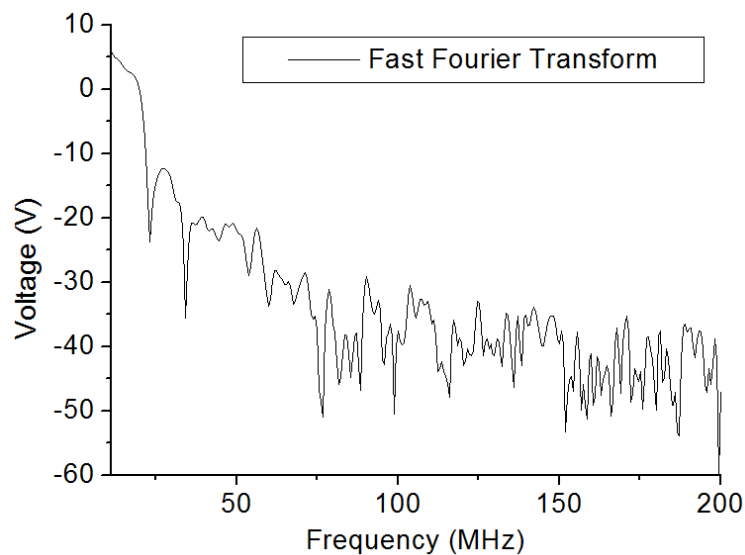
Source: Author's production.

Figure 5.30 displays the FFT spectrum of the output signal where the oscillation frequency of Fig. 5.29 (b) can be obtained at a frequency near the first knee of the curve, 20.0 MHz approximately. The order of magnitude of this frequency can be also obtained using (3.31) (see section 3.4.2.3 in chapter 3) that relates oscillation frequency with magnetic axial and azimuthal fields. In CGS units, (3.35) is given by:

$$f_c \approx 14 \frac{\text{GHz}}{T} \times \mu_0 H_\theta \sqrt{\frac{\chi M_s}{\mu_0 H_z}} \quad (5.1)$$

where $14 \text{ GHz/T} = \frac{\mu_0 \gamma}{4\pi}$, the ferrite magnetization at saturation $M_s = 0.35 \text{ T}$ and ferrite filling factor $\chi \approx 0.7$, considering the used ferrite outer and inner diameters of 1.93 and 1.03 mm, respectively. Thus, for $H_\theta = 148 \text{ A/m}$ and $H_z = 7960 \text{ A/m}$, the center frequency calculated is of the order of 12 MHz, reasonably in the range of magnitude for the value measured on FFT spectrum of about 20 MHz.

Figure 5.30. Output FFT spectrum of the NLTL at low voltage operation.

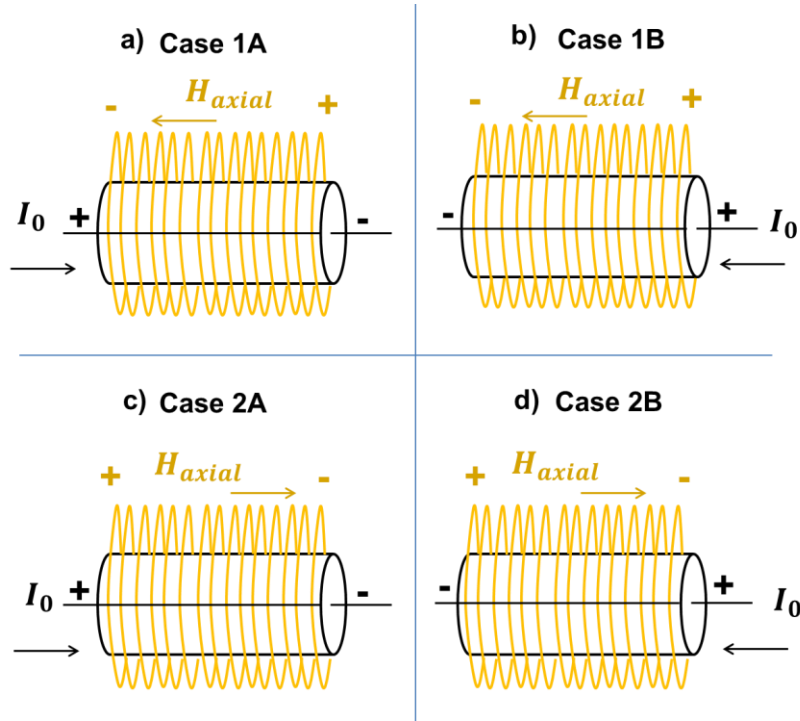


Source: Author's production.

5.6.4.1. Different Configurations of Magnetic Biases for the Gyromagnetic NLTL at Low Voltage Operation

Different connections with both magnetic biases, axial and azimuthal, were performed to verify the influence on the output pulse of gyromagnetic line at low voltage operation. Four different configurations were used to vary the direction of the axial magnetic field $H_z=H_0$ and bias current I_0 responsible for the azimuthal field as shown in Figure 5.31.

Figure 5.31. Different configurations of magnetic biasing showing four possible combinations for directions of the axial field H_0 and bias current I_0 .

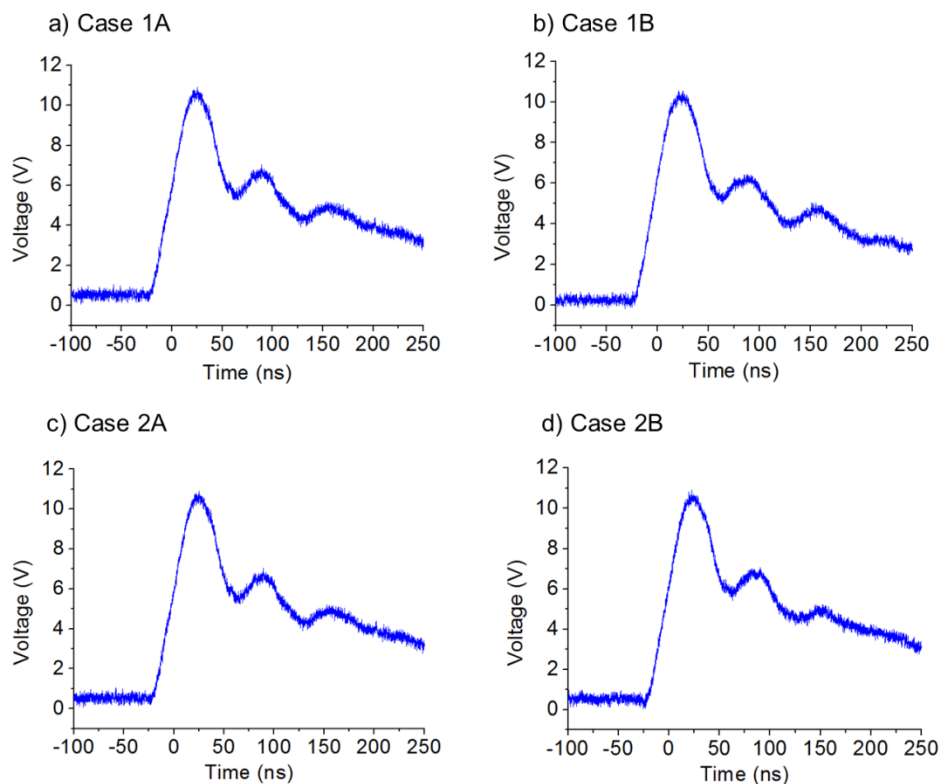


Source: Author's production.

The axial field and bias current directions are changed by inverting the output connections of the DC current sources in the line experimental set-up shown in Figure 4.6 (Chapter 4.2). For instance, in cases 1A and 2B as shown respectively in Figures 5.31 (a) and (d) H_0 and I_0 have opposite directions, while

in case 1B and 2A they are in the same direction given respectively in Figures 5.31 (b) and (c). For cases 1A and 1B, H_0 points towards the input (-z) whereas for 2A and 2B towards the output (+z). With I_0 , it goes from input to output for cases 1A and 2A and opposite for cases 1B and 2B. For all the cases, the solenoid current and the axial bias current I_0 were kept around the corresponding values of 8 A and 0.7 A, giving respectively 7960 A/m and 148 A/m for the axial and azimuthal fields (see Table 5.8 again). The results obtained for the four cases are shown in Figure 5.32, where one can note slight variations on the output pulse in terms of oscillation frequency mainly as expected.

Figure 5.32. Output pulse of the NLTL operating at low voltage in four different configurations.



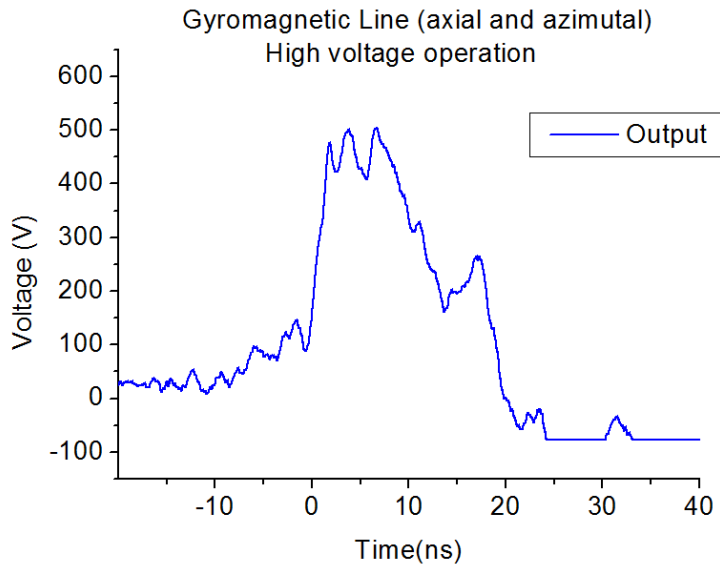
Source: Author's production.

Since the measurements were made with the line with open terminals as in the previous section, the bias current pulse I_0 is zero. Moreover, it seems that the rotational movement of the azimuthal field is not affected by the sense of the axial field.

5.6.5. Experimental Line with Axial and Azimuthal Bias for High Voltage Operation

A line test was also performed at high voltage using the FID generator (already described in Chapter 4.2) with axial and azimuthal bias applied simultaneously at bias currents of 2.10 A and 0.24 A, respectively. The formulae for the H-field calculation is obtained once more in the first column of Table 5.8 shown in the last section. A current of 10.0 A through the axial line solenoid corresponds to an intensity of an external magnetic field of about 2308 A/m. However, in this case the azimuthal field is generated by the sum of the currents provided by the DC source bias (0.24 A) and the high voltage pulse applied, which is of the order of 10.24 A (10 A + 0.24 A) considering the peak amplitude of the output pulse obtained of about 500 V into a load of 50 ohms as shown in Fig. 5.33. Thus, this corresponds to an azimuthal field of the order of 2149 A/m. To obtain the result in Figure 5.33 the FID generator of fast rise time was used to produce an input pulse with peak of about 2500 V with an approximate Gaussian shape of 5ns width. As observed in this figure the lower pulse peak amplitude at output is due to the negative coefficient reflection as load resistance is 50 ohms and the stressed line impedance is higher (of the order of 450 ohms) since the ferrite is not heavily saturated under this condition and limitation of the maximum voltage provided by the generator.

Figure 5.33. Line output pulse with axial and azimuthal bias at high voltage operation.



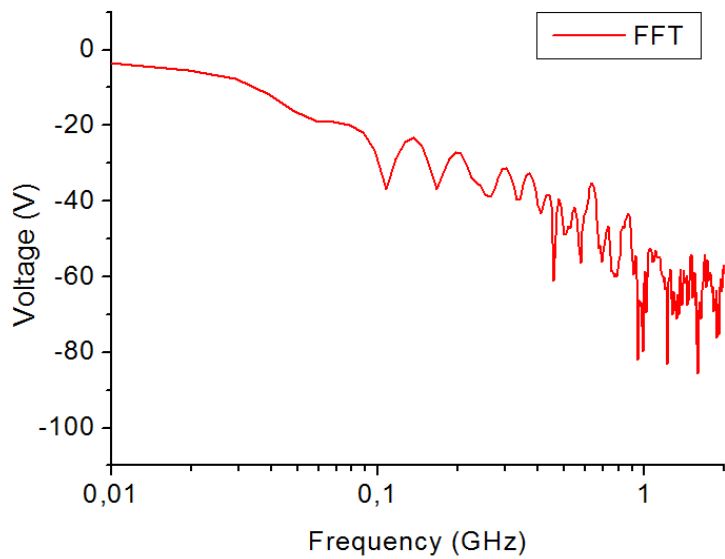
Source: Author's production.

Figure 5.34 shows the FFT spectrum of the output pulse. Although not very clear in the FFT spectrum the oscillation frequency appears to be in the range of 300-400 MHz. In fact, this value can be confirmed using (3.34) in CGS units as given below

$$f_c \approx 14 \frac{G_{Hz}}{T} \mu_0 H_\theta \sqrt{1 + \frac{\chi M_s}{\mu_0 \sqrt{H_\theta^2 + H_z^2}}} \quad (5.2)$$

where χ is assumed to be 0.7 and $M_s=0.35$ T. For $H_z= 2308$ A/m and $H_\theta=2149$ A/m, (5.2) gives a center frequency near 300 MHz, which is of the order of magnitude seen in the FFT in Fig. 5.34.

Figure 5.34. FFT spectrum of the output pulse for line operation at high voltage.



Source: Author's production.

It is important to highlight that we did not achieve a better signal at the output of the gyromagnetic line because of the voltage limitation of the function generator that was used.

6. CONCLUSIONS

According to the results obtained from LT simulations, numerical computation, and experimental analysis it is possible to make the following conclusions:

- ✓ Weiner's model was adapted to the Spice simulations in which R_f (ferrite losses) is dependent on the azimuthal bias and responsible for the output rise time variation.
- ✓ In Pouladian-Kari LT-Spice model, the resonant RLC branches were added to simulate the precession of the ferrite magnetic moment under the presence of an axial magnetic bias.
- ✓ In Pouladian-Kari's model, the values of the RLC branches are fixed for constant magnetic bias while for linearly graded magnetic bias the RLC components are linearly varied to represent the axial magnetic field increasing along the line.
- ✓ LT-Spice and Mathematica simulations based on Dolan's model were reproduced with great success without the need of voltage sources, since the flux equation simulates fully the nonlinear behavior of the line.
- ✓ Dolan's numerical analysis is in good agreement with the LT-Spice simulation result, which validates the results of the Spice modelling.
- ✓ Spice simulation has a user-friendly platform compared to numerical computation as in the latter case it is harder to work with the implementation of the code lines. However, once the code is ready, for numerical analysis it is easier to make any changes, especially for a large number of line sections.
- ✓ The coaxial line inductance was characterized in relation to an axial current through the inner conductor fed by a DC source with and without

permanent magnets as well as in relation to an axial magnetic field generated by an external solenoid.

- ✓ The LT-Spice simulated model was validated by comparing the results with the experimental test using permanent magnets.
- ✓ Different connections with both biases, axial and azimuthal, were performed in order to verify the influence on the output pulse.
- ✓ In the experimental tests, it was observed that when the axial bias is increased, the frequency is also increased with output pulse rise time compression.
- ✓ Moreover, it was noted that the azimuthal bias has direct relation with the modulation of the output pulse and a slight influence on the output rise time compression.
- ✓ At low voltage operation with open circuit at the end of the line, good modulation of the output pulse was obtained, although the slow rise time of the input pulse makes it difficult to observe the gyromagnetic effect.
- ✓ At high voltage operation, the frequency generated by the gyromagnetic line was around 400 MHz.
- ✓ NLTL frequency has a stronger dependence on the input pulse voltage as azimuthal field is generated by the resulting pulse current.
- ✓ The development of gyromagnetic lines demands the research on new nonlinear magnetic materials which present high saturation magnetization variation with low voltage and also have a good performance in the aggressive space environment.
- ✓ This research also identified that there is a strong demand for nonlinear magnetic materials that have a high saturation magnetization variation

with low voltage and also have a good performance in the aggressive conditions of space environment.

All these conclusions give basis as exploratory research for the use of the gyromagnetic line in aerospace applications. The development of gyromagnetic lines demands the research on new nonlinear magnetic materials which present high saturation magnetization with low voltage and also have a good performance in the aggressive conditions of space environment.

7. FUTURE WORK

As gyromagnetic NLTL research is a new area, there are many issues that need to be explored. Among the several topics to be studied, we suggest those that could lead to the possible use of NLTL in aerospace applications such as

- ✓ Study of new magnetic materials with nonlinear behavior at higher and lower voltage operation.
- ✓ Analysis of critical parameters and material components of the NLTLs that need to be evaluated in order to comply with the requirements for space applications.
- ✓ Need of performing space qualification tests (temperature, vacuum, gravity, radiation) of the components and materials used in the NLTL.
- ✓ Length increase of the experimental gyromagnetic coaxial line in order to observe with accuracy the output pulse delay and its influence on magnetic precession and output rise time.
- ✓ Assembly improvements especially related to line connections to decrease stray parasitic impedances that deteriorate the input and output signals.
- ✓ Exploratory studies of gyromagnetic NLTL implementation in space vehicles and satellites taking into account the need for two extra batteries and an input fast pulse generator which can impact on the compact size of the device required in space applications.
- ✓ Design and protection of the DC current sources in such a way that even with NLTLs operating with high voltage pulses they continue to work normally without electromagnetic interference.
- ✓ To clarify better the stronger frequency dependence on azimuthal field rather than on the axial one in gyromagnetic lines.

REFERENCES

- [1] LARSON, W. J.; WERTZ, J. R. **Space mission analysis and design**. 3. ed. Microcosm Press and Kluwer Academic Publishers, 2005.
- [2] BRISKMAN, R.D.; KALISKI, M.A.R. Transmitter microdischarges in communications and Broadcast Satellites. **Acta Astronautica**, v.126, Oct.2016, p.163-167.
- [3] ROMANCHENKO, I.V.; ROSTOV, V.V.; GUNIN, A.V.; KONEV, V.Y. High power microwave beam steering based on gyromagnetic nonlinear transmission lines. **J. Appl. Phys.**, v.117, 214907, Jun. 2015.
- [4] ROSTOV, V.V.; BYKOV, N.M.; BYKOV, D.N.; GUNIN, A.V.; KLOMOV, A.I.; KOVALCHUK, O.B.; KUTENKOV, V.O.; ROMANCHENKO, I.V. Generation of sub-GW RF pulses in nonlinear transmission lines. In: IEEE INTERNATIONAL PULSED POWER CONFERENCE, 2009, Washington, DC. **Proceedings...** Washington: IEEE, 2009. p.70-73.
- [5] ROMANCHENKO, I.V.; ROSTOV, V.V.; GUBANOV, V.P.; STEPCHENKO, A.S.; GUNIN, A.V.; KURKAN, I.K. Repetitive sub-gigawatt rf source based on gyromagnetic nonlinear transmission line, **Rev. Sci. Instrum.**, v. 83, 074705, Jul. 2012.
- [6] REALE, D.V.; PARSON, J.M.; NEUBER, A.A.; DICKENS, J.C.; MANKOWSKI, J.J. Investigation of a stripline transmission line structure for gyromagnetic nonlinear transmission line high power microwaves sources. **Rev. Sci. Instrum.**, v. 87, 034706, March 2016.
- [7] REALE, D.V.; BRAGG, J.W.; GONSALVES, N.R.; JOHNSON, J.M.; NEUBER, A.A.; DICKENS, J.C.; MANKOWSKI, J.J. Bias-field controlled phasing and power combination of gyromagnetic nonlinear transmission lines. **Rev. Sci. Instrum.**, v. 85, 054706, May 2014.

- [8] SEDDON, N.; SPIKINGS, C.R.; DOLAN, J.E. RF Pulse formation in NLTLs. In: IEEE INTERNATIONAL PULSED POWER CONFERENCE, 16., 2007, Albuquerque, USA. **Proceedings...** Albuquerque: IEEE, 2007. p. 678-681.
- [9] BROWN, M.P.; SMITH, P.W. High Power, pulsed soliton generation at radio and microwave frequencies. In: IEEE INTERNATIONAL PULSED POWER CONFERENCE, 1997, Baltimore, MD, **Proceedings...** Baltimore: IEEE, 1997. p. 346-354.
- [10] SMITH, P.W. **Transient electronics**: pulsed circuit technology. West Sussex, England: John Wiley & Sons, 2002. p. 237-264.
- [11] SPIKINGS, C. R.; SEDDON, N.; IBBOTSON, R. A.; DOLAN, J. E. HPM Systems based on NLTL technologies. In: IET CONFERENCE ON HIGH POWER RF TECHNOLOGIES. 2009, London, UK. **Proceedings...** London: IET, 2009. p.1-3.
- [12] KATAYEV, I.G. **Electromagnetic shock waves**. London, U.K.: Iliffe Books Ltda, 1966.
- [13] WEINER, M. Pulse sharpening in ferrite transmission line. In: IEEE PULSED POWER CONF., 2., 1979, New York. **Proceedings...** New York: IEEE, 1979. p. 91-95.
- [14] POULADIAN-KARI ET AL.-KARI, R.; BENSON, T.M.; SHAPLAND, A.J.; PARKES, D.M. The electrical simulation of pulse sharpening by dynamic lines. In: IEEE INTERNATIONAL PULSED POWER CONFERENCE, 7., 1989, Monterrey – California. **Proceedings...** IEE, 1989. p.178-181.
- [15] POULADIAN-KARI ET AL.-KARI, R.; SHAPLAND, A.J.; BENSON, T.M. Development of ferrite line pulse sharpeners for repetitive power applications. **IEEE Proceedings-H Microwaves, Antennas and Propagation.** , v. 138, n. 6, p. 504-512, 1991.

- [16] DOLAN, J.E.; BOLTON, H.R. Shock front development in ferrite-loaded coaxial lines with axial bias. **IEEE Proc.-Sci. Meas. Technol.**, v. 147, n. 5, p. 237-242, 2000.
- [17] FLEETER, R. **Micro space craft**. The Edge City Press, 1995.
- [18] DOODY, D.; STEPHAN, G. **Basics of space flight**: learners workbook, advanced mission operations section. Jet Propulsion Laboratory, Rev. A, 1995.
- [19] PISACANE, V.L.; MOORE, R.C. **Fundamentals of space systems**. New York: Oxford University Press, 1994.
- [20] NEAL, V.; LEWIS, C.S.; WINTER, F.H. **Spaceflight**: a Smithsonian guide. New York: Mc Millan, 1995.
- [21] PRADO, A.F.B.; KUGA, H.K. **Fundamentos de tecnologia espacial**. INPE, São José dos Campos, 2001.
- [22] WERTZ, J.R.; LARSON, W.J. **Reducing space mission cost**. space technology library. Dordrech: Kluwer, 1999.
- [23] BRAGG, J.W.B.; DICKENS, J.; NEUBER, A. Investigation into the temperature dependence of ferrimagnetic nonlinear transmission lines. **IEEE Trans. Plasma Sci.**, v. 40, n. 10, p. 2457-2461, 2012.
- [24] INTERNATIONAL TELECOMMUNICATION UNION. Available in < <http://www.itu.int/en/ITU-R/Pages/default.aspx> >. Access date: 27th June, 2016.
- [25] MOREIRA, A. Synthetic Aperture Radar (SAR): principles and applications. In: ADVANCED TRAINING COURSE IN LAND REMOTE SENSING, 4., 2013, Atenas. **Transparências...** ESA, July 2013. Available in: <https://earth.esa.int/documents/10174/642943/6-LTC2013-SAR-Moreira.pdf> . Access date: 30th August, 2015.

- [26] COSTA, M. M. S.; BOGOSSIAN, O. L.; PASSARO, A. Basic Requirements for synthetic aperture radar satellite mission. In: WORKSHOP EM ENGENHARIA E TECNOLOGIA ESPACIAIS, 6. (WETE), **Proceedings...**São José dos Campos. INPE, 2015. On-line. ISSN 2177-3114. Available in: <<http://urlib.net/8JMKD3MGP3W34P/3L8HBTL>>. Access date: 16th May, 2016.
- [27] LEITE, B. R. A.; HABERMANN, M. Utilização do SAR R-99 para busca marítima: metodologias e possibilidades de emprego. In: SIMPÓSIO DE APLICAÇÕES OPERACIONAIS EM ÁREAS DE DEFESA – SIGE, **Proceedings...** São José dos Campos: Sige, 2013. 15. ITA. 1 CD-ROM.
- [28] Voyager Mission celebrates 30 years since Uranus. Available in <http://voyager.jpl.nasa.gov/news/uranus_30_year.html>. Access date: 11th November, 2016.
- [29] GILMOUR, A.S. **Klystrons, traveling wave tubes, magnetrons, crossed-field amplifiers, and gyrotrons.** Atech House, 2011. p. 317-18. ISBN 1608071855.
- [30] TRAVELING-wave tube: electronics in Encyclopedia Britannica. Available in <<http://global.britannica.com/technology/traveling-wave-tube>>. Access date: 23th June, 2016.
- [31] MICROWAVE tubes: PT6049 Traveling wave tube in TMD. Available in <<http://www.tmd.co.uk/products/microwave-tubes/details.asp?id=145>>. Access date: 25th June, 2016.
- [32] ROSSI, J.O.; SILVA NETO, L.P.; YAMASAKI, F.S.; BARROSO, J.J.; RANGEL, E.G.L.; SCHAMILOGLU, E. **High-Voltage Soliton Generation with Nonlinear Lumped Varactor Diode Lines.** In: SIMPÓSIO DE APLICAÇÕES OPERACIONAIS NA ÁREA DA DEFESA (SIGE), 18., 2016, São José dos Campos. **Proceedings...** São José dos Campos: ITA, 2016.

- [33] ROSSI, J.O; SCHAMILOGLU, E.; KUEK, N. S.; YAMASAKI, F. S. Design considerations in Lossy dielectric nonlinear transmission lines. In: IEEE PULSED POWER AND PLASMA SCIENCE, 2013, San Francisco. **Proceedings...** San Francisco: IEEE, 2013.
- [34] SILVA NETO, L. P.; ROSSI, J. O.; BARROSO, J. J.; YAMASAKI, F. S. RF pulse formation in NLTLs using varactor diode. In: SIMPÓSIO DE APLICAÇÕES OPERACIONAIS EM ÁREAS DE DEFESA (SIGE), 16., 2014, São José dos Campos. **Proceedings...** São José dos Campos: ITA, 2014. 1 CD-ROM.
- [35] YAMASAKI, F. S.; SCHAMILOGLU, E. ; J.O. ROSSI ; BARROSO, J. J. Spice simulations of inductive nonlinear transmission lines. In: INTERNATIONAL MICROWAVE AND OPTOELECTRONICS CONFERENCE (IMOC 2015), 2015, Porto de Galinhas. **Proceedings...** Porto de Galinhas: IEEE, 2015.
- [36] GAUDET, J.; SCHAMILOGLU, E.; ROSSI, J.O.; BUCHENAUER, C.J.; FROST, C. Nonlinear transmission lines for high power microwave applications: a survey. In: IEEE INTERNATIONAL POWER MODULATORS AND HIGH-VOLTAGE CONFERENCE, 2008. Las Vegas. **Proceedings...** Las Vegas: IEEE, 2008. p. 131-138.
- [37] RANGEL, E.G.L.; BARROSO, J.J.; J.O. ROSSI YAMASAKI, F.S. ; SILVA NETO, L.P.; SCHAMILOGLU, E. Influence of input pulse shape on RF generation in nonlinear transmission lines. **IEEE Transactions on Plasma Science**, v. 44, n. 10, p. 2258-2267, Oct. 2016. DOI: 10.1109/TPS.2016.2593606.
- [38] RANGEL, E.G.L.; ROSSI, J.O.; BARROSO, J.J.; YAMASAKI, F.S.; SILVA NETO, L.P.; SCHAMILOGLU, E. Analysis of RF generation using NLTLs driven by pump input pulses of different shapes. In: EURO-ASIAN PULSED POWER CONFERENCE (EAPPC 2016), 6., 2016, Estoril. **Proceedings...** Estoril: IEEE, 2016.

- [39] YAMASAKI, F. S.; ROSSI, J.O.; BARROSO, J. J. Estudos de linhas de transmissão não lineares para geração de sinais de radio frequência. In: SIMPÓSIO BRASILEIRO DE MICRO-ONDAS E OPTOELETRÔNICA (SBMO, 15), 15. E CONGRESSO BRASILEIRO DE ELETROMAGNETISMO (CBMAG, 10), 10., 2012, João Pessoa. **Anais...** João Pessoa: 2012.
- [40] YAMASAKI, F. S.; ROSSI, J.O.; BARROSO, J. J.; SILVA NETO, L. P. Geração de RF usando linhas de transmissão não lineares. In: MOMAG 2014, 2014, Curitiba. **Proceedings...** Curitiba: 2014.
- [41] ROSSI, J. O.; SILVA, L. P.; BARROSO, J. J.; YAMASAKI, F. S.; SCHAMILOGLU, EDL . Overview of RF generation using nonlinear transmission lines. In: IEEE PULSED POWER CONFERENCE (PPC), 2015, Austin, TX, **Proceedings...** Austin: IEEE, 2015. ISBN 9781479984039. DOI: <10.1109/ppc.2015.7296892>. Disponível em: <<http://dx.doi.org/10.1109/ppc.2015.7296892>>.
- [42] ROSSI, J. O.; SILVA NETO, L. P.; YAMASAKI, F. S.; BARROSO, J. J. State of the art of nonlinear transmission lines for applications in high power microwaves. In: SBMO/IEEE MTTS INTERNATIONAL MICROWAVE AND OPTOELECTRONICS CONFERENCE (IMOC), 15., 2013, Rio de Janeiro. **Proceedings...** Rio de Janeiro: SBMO/IEEE MTTS, 2013.
- [43] YAMASAKI, F. S.; J.O. ROSSI ; BARROSO, J. J. Study of nonlinear lumped element transmission lines for RF generation. In: WORKSHOP EM ENGENHARIA E TECNOLOGIA ESPACIAIS, 3. (WETE), **Proceedings...** São José dos Campos. INPE, 2013. On-line. Available in: <<http://mtc-m21b.sid.inpe.br/rep/sid.inpe.br/mtc-m19/2013/10.22.12.15>>. Access date: 10th June, 2016.
- [44] SILVA NETO, L.P.; ROSSI, J.O.; YAMASAKI, F. S.; BARROSO, J. J. Análise do comportamento de uma LTNL em baixa tensão. In: WORKSHOP EM ENGENHARIA E TECNOLOGIA ESPACIAIS, 4. (WETE), **Proceedings...**

São José dos Campos. INPE, 2014. On-line. Available in: <[http://mtc-m16d.sid.inpe.br/col/sid.inpe.br/mtc-m19/2013/05.22.14.54/doc/livretos/\[WETE\]\[2014\]\[Livreto\].pdf](http://mtc-m16d.sid.inpe.br/col/sid.inpe.br/mtc-m19/2013/05.22.14.54/doc/livretos/[WETE][2014][Livreto].pdf)>. Access date: 25th October, 2016.

- [45] YAMASAKI, F. S.; ROSSI, J. O.; BARROSO, J. J. RF generation using nonlinear transmission lines for aerospace applications. In: SBMO/IEEE MTTS INTERNATIONAL MICROWAVE AND OPTOELECTRONICS CONFERENCE (IMOC), 15., 2013, Rio de Janeiro. **Proceedings...** Rio de Janeiro: SBMO/IEEE MTTS, 2013.
- [46] IKEZI, H.; DEGRASSIE, J. S.; DRAKE, J. Soliton generation at 10 MW level in the very high frequency band. **Applied Physics Letters**, v.58, p.986, 1991.
- [47] IKEZI, H.; WOJTOWICZ, S.S.; WALTZ, R.E.; de GRASSIE, J.S.; BAKER, D.R. High power soliton generation at microwave frequencies. **J. Appl. Phys.**, v. 64, p. 3277-3281, Jun. 1988.
- [48] KUUSELA, T.; HIETARINTA, J. Nonlinear electrical transmission line as a burst generator. **Rev. Sci. Instrum.**, v. 62, p. 2266-2270, May 1991.
- [49] KUEK, N. S. **Theoretical and experimental studies on nonlinear lumped element transmission lines for RF generation**. Thesis submitted for the Degree of Doctor of Philosophy Department of Electrical & Computer Engineering National University of Singapore, 2013.
- [50] KUEK, N.S.; LIEW, A.C.; SCHAMILOGLU, E.; ROSSI, J.O. Circuit modeling of nonlinear lumped element transmission lines including hybrid lines. **IEEE Trans. Plasma Sci.**, v.40, n.10, p.2523-2534, Oct. 2012.
- [51] YAMASAKI, F.S.; SILVA NETO, L.P.; ROSSI, J.O.; BARROSO, J.J. Soliton generation using nonlinear transmission lines. **IEEE Trans. Plasma Sci.**, v.42, n.11, p.3471-3477, Nov. 2014.

- [52] ROSSI, J.O.; RIZZO, P.N. Study of hybrid nonlinear transmission lines for high power RF generation. In: IEEE INTERNATIONAL PULSED POWER CONFERENCE, 2009, Washington, DC. **Proceedings...** Washington: IEEE, 2009. p.46-50.
- [53] YAMASAKI, F.S.; DE ANGELIS, A.F.; ROSSI, J.O. **Simulação gráfica no MATLAB da solução de ondas de sólitons para a equação de Korteweg-de Vries (KdV).** Trabalho de graduação interdisciplinar apresentado junto à Faculdade de tecnologia, como requisito de conclusão do curso de Tecnologia em telecomunicações, UNICAMP, Limeira, Julho de 2010.
- [54] DRAZIN, P. G.; JOHNSON, R. S. **Solitons:** an introduction. Cambridge: texts in applied Mathematics, 1989.
- [55] GALLEAS, W.; YMAI, L.H.; NATTI, P.L.; TAKANO, E.R. Ondas do tipo sóliton em guias dielétricos. **Revista Brasileira de Ensino de Física**, v. 25, n. 3, set. 2003.
- [56] YAMASAKI, F. S.; SCHAMILOGLU, E.; ROSSI, J.O.; BARROSO, J. J. Simulation studies of distributed nonlinear gyromagnetic lines based on LC lumped model. **IEEE Transactions on Plasma Science**, v.44, n. 10, p.2232-2239, Oct. 2016. DOI: 10.1109/TPS.2016.2556320
- [57] YAMASAKI, F.S.; ROSSI, J.O.; BARROSO, J.J.; SCHAMILOGLU, E. Analysis of a gyromagnetic nonlinear transmission line based on experimental results. In: IEEE EURO-ASIAN PULSED POWER CONFERENCE, 2016, Estoril, Portugal. **Proceedings...** Estoril: IEEE, 2016.
- [58] YAMASAKI, F. S.; SCHAMILOGLU, E.; ROSSI, J. O.; BARROSO, J. J. Spice simulations of nonlinear gyromagnetic lines. In: IEEE PULSED POWER CONFERENCE, 2015, Austin, TX. **Proceedings...** Austin: IEEE, 2015.

- [59] YAMASAKI, F.S.; ROSSI, J.O.; BARROSO, J.J.; SCHAMILOGLU, E. Simulação de linhas não lineares giromagnéticas. In: MOMAG 2016, 2016, Porto Alegre. **Proceedings...** Porto Alegre: 2016.
- [60] POZAR, D.M. **Microwave engineering**. 3. ed. John Wiley & Sons Inc., 2005, p.441-485.
- [61] LAKSHMANAN, M. The fascinating world of the Landau-Lifshitz-Gilbert equation: an overview. **Philosophical Transactions of The Royal Society A Mathematical Physical and Engineering Sciences**, A 369, p. 1280–1300, 2011.
- [62] MALLINSON, J.C. On damped gyromagnetic precession. **IEEE Transactions on Magnetics**, v. 23, n. 4, p. 2003-2004, July 1987.
- [63] LANDAU-Lifshitz-Gilbert equation. Available in <https://en.wikipedia.org/wiki/Landau%20%93Lifshitz%20%93Gilbert_equation>. Access date: 03rd October, 2016.
- [64] ROMANCHENKO, I.V.; ROSTOV, V.V.; GUNIN, A.V.; KONEV, V.Y. High power microwave beam steering based on gyromagnetic nonlinear transmission lines. **J. Appl. Phys.**, v.117, 214907, 2015.
- [65] BRAGG, J.W.B.; DICKENS, J.C.; NEUBER, A.A. Material selection considerations for coaxial, ferrimagnetic-based nonlinear transmission lines. **J. Appl. Phys.**, v.113, 064904, 2013.
- [66] GYORGY, E.M. Rotational model of flux reversal in square loop ferrites. **J. Appl. Phys.**, v. 28, p.1011-1015, Sept. 1957.
- [67] GRECO, A.F.G.; BARROSO, J.J.; ROSSI, J.O. Modeling and analysis of ladder-network transmission lines with capacitive and inductive lumped elements. **Journal of Electromagnetic Analysis and Applications**, v.5, n.5, p. 2013-218, May 2013.

- [68] BRAGG, J.; DICKENS, J.; NEUBER, A. Temperature dependence on ferrimagnetic based nonlinear transmission line. In: IEEE INTERNATIONAL PULSED POWER CONFERENCE, 2011, Chicago, IL, **Proceedings...** Chicago: IEEE, 2011. p.182-184.
- [69] FRENCH, D.; HOFF, W. Spatially dispersive ferrite nonlinear transmission line with axial bias. **IEEE Transactions on Plasma Science**, v.42, n. 10, p.3387-3390, Aug. 2014. DOI: 10.1109/TPS.2014.2348492
- [70] AHN, J.W.; KARELIN, S.Y.; KRASOVITSKY, V.B.; KWON, H.O.; MAGDA, I.I.; MUKHIN, V.S.; SINITSIN, V.G. Exciting high frequency oscillations in a coaxial transmission line with a magnetized ferrite: 2D approach. **Journal of Magnetics**, v.100, n. 6, p. 68-72, Dec. 2015.
- [71] JOHNSON, J.M.; REALE, D.V.; CRAVEY, W.H.; GARCIA, R.S; BARNETT, D.H.; NEUBER, A.A.; DICKENS, J.C.; MANKOWSKI, J.J. Material selection of a ferrimagnetic loaded coaxial delay line for phasing gyromagnetic nonlinear transmission lines. **The Review of Scientific Instruments**, v, 86, n. 8, 084702, 2015. PMID:26329216.
- [72] REALE, D.V.; PARSON, J.M.; NEUBER, A.A.; DICKENS, J.C.; MANKOWSKI, J.J. Investigation of a stripline transmission line structure for gyromagnetic nonlinear transmission line high power microwave sources. **Rev. Sci. Instrum.**, v. 87, 034706, 2016.
- [73] JOHNSON, J.M.; REALE, D.V.; KRILLE, J.T.; GARCIA, R.S.; CRAVEY, A.A.; NEUBER, A.A.; DICKENS, J.C.; MANKOWSKI, J.J. Characteristics of a four element gyromagnetic nonlinear transmission line array high power microwave source. **Rev. Sci. Instrum.**, v. 87, 054704, 2016.
- [74] MARKSTEINER, Q.R.; CARLSTEN, B.; RUSSELL, S. Numerical calculations of RF efficiency from a soliton generating nonlinear transmission line. **J. Appl. Phys.**, v.106, 113306, 2009.

[75] DESOER, C. A.; KUH, E.S. **Basic circuit theory**. McGraw-Hill, 1969.

APPENDIX A: DEVELOPMENT OF EQUATIONS

The main equations that had to be developed in order to justify or understand a specific issue during the thesis are presented in this appendix.

A.1. Linear Capacitance

Considering the total capacitance per unit length of the line as the relation:

$$\frac{1}{C_T} = \frac{1}{C_1} + \frac{1}{C_2}, \quad (\text{A.1.1})$$

since $C_1 = \frac{2\pi\varepsilon_0\varepsilon_1}{\ln(\frac{b}{a})}$ and $C_2 = \frac{2\pi\varepsilon_0\varepsilon_2}{\ln(\frac{D}{d_o})}$, where ε_0 is the electrical permittivity of free space, ε_1 is the electrical permittivity of the ferrite, ε_2 is the electrical permittivity of the dielectric, D is outer radius of the line, b is the outer radius of the ferrite and a is the inner radius of the ferrite.

Then,

$$\frac{1}{C_T} = \frac{\ln(\frac{b}{a})}{2\pi\varepsilon_0\varepsilon_1} + \frac{\ln(\frac{D}{b})}{2\pi\varepsilon_0\varepsilon_2}, \quad (\text{A.1.2})$$

$$\frac{1}{C_T} = \frac{\varepsilon_2 \ln(\frac{b}{a}) + \varepsilon_1 \ln(\frac{D}{b})}{2\pi\varepsilon_0\varepsilon_1\varepsilon_2}, \quad (\text{A.1.3})$$

$$C_T = \frac{2\pi\varepsilon_0\varepsilon_1\varepsilon_2}{\varepsilon_2 \ln(\frac{b}{a}) + \varepsilon_1 \ln(\frac{D}{b})}. \quad (\text{A.1.4})$$

The final equation of the linear capacitance is

$$C_T = \frac{2\pi\epsilon_0}{\frac{\ln(\frac{b}{a})}{\epsilon_1} + \frac{\ln(\frac{D}{b})}{\epsilon_2}}. \quad (\text{A.1.5})$$

A.2. Relation between LLG and LL Equations

Considering the original LL equation dated from 1935,

$$\frac{\partial \vec{M}}{\partial t} = \gamma \mu_0 \vec{M} \times \vec{H} - \frac{\alpha \gamma}{M_s} \mu_0 [\vec{M} \times (\vec{M} \times \vec{H})], \quad (\text{A.2.1})$$

and the modified version LLG from 1955,

$$\frac{\partial \vec{M}}{\partial t} = \gamma \mu_0 \vec{M} \times \vec{H} - \frac{\alpha}{M_s} \vec{M} \times \frac{\partial \vec{M}}{\partial t}, \quad (\text{A.2.2})$$

substituting in the right-hand side of (A.2.2) the term $\frac{\partial \vec{M}}{\partial t}$,

$$\frac{\partial \vec{M}}{\partial t} = \gamma \mu_0 \vec{M} \times \vec{H} - \frac{\alpha}{M_s} \vec{M} \times \left[\gamma \mu_0 \vec{M} \times \vec{H} - \frac{\alpha}{M_s} \vec{M} \times \frac{\partial \vec{M}}{\partial t} \right], \quad (\text{A.2.3})$$

$$\frac{\partial \vec{M}}{\partial t} = \gamma \mu_0 \vec{M} \times \vec{H} - \frac{\alpha}{M_s} \gamma \mu_0 \vec{M} \times (\vec{M} \times \vec{H}) + \frac{\alpha^2}{M_s^2} \vec{M} \times \left(\vec{M} \times \frac{\partial \vec{M}}{\partial t} \right). \quad (\text{A.2.4})$$

Using vector cross product identity, we have:

$$a \times (b \times c) = b(a \cdot c) - c(a \cdot b), \quad (\text{A.2.5})$$

$$\vec{M} \times \vec{M} \times \frac{\partial \vec{M}}{\partial t} = \vec{M} \left(M \cdot \frac{\partial \vec{M}}{\partial t} \right) - \frac{\partial \vec{M}}{\partial t} (\vec{M} \cdot \vec{M}). \quad (\text{A.2.6})$$

Since $\vec{M} \cdot \frac{\partial \vec{M}}{\partial t} = 0$ (because of the circular nature of the motion, $\vec{M} \cdot (\vec{M} \times \vec{H}) = 0$) and $\vec{M} \cdot \vec{M} = M^2$, then

$$\vec{M} \times \left(\vec{M} \times \frac{\partial \vec{M}}{\partial t} \right) = -M^2 \frac{\partial \vec{M}}{\partial t}. \quad (\text{A.2.7})$$

So,

$$\frac{\partial \vec{M}}{\partial t} = \gamma \mu_0 \vec{M} \times \vec{H} - \frac{\alpha}{M_s} \gamma \mu_0 \vec{M} \times (\vec{M} \times \vec{H}) + \frac{\alpha^2}{M_s^2} (-M^2) \frac{\partial \vec{M}}{\partial t}, \quad (\text{A.2.8})$$

$$\frac{\partial \vec{M}}{\partial t} = \gamma \mu_0 \vec{M} \times \vec{H} - \frac{\alpha}{M_s} \gamma \mu_0 \vec{M} \times (\vec{M} \times \vec{H}) - \alpha^2 \frac{\partial \vec{M}}{\partial t}, \quad (\text{A.2.9})$$

$$(1 + \alpha^2) \frac{\partial \vec{M}}{\partial t} = \gamma \mu_0 \vec{M} \times \vec{H} - \frac{\alpha}{M_s} \gamma \mu_0 \vec{M} \times (\vec{M} \times \vec{H}), \quad (\text{A.2.10})$$

$$\frac{\partial \vec{M}}{\partial t} = \frac{\gamma \mu_0}{(1+\alpha^2)} \left[\vec{M} \times \vec{H} - \frac{\alpha}{M_s} \vec{M} \times (\vec{M} \times \vec{H}) \right]. \quad (\text{A.2.11})$$

Thus LL and LLG equations are equivalent if $\alpha \ll 1$.

A.3. Formulation in Cartesian Coordinates

With an initial axial magnetic bias field it is possible to analyze the Landau-Lifshitz equation in Cartesian coordinates as follows:

$$\frac{\partial \vec{M}}{\partial t} = \frac{\gamma}{1+\alpha^2} \mu_0 \left[\vec{M} \times \vec{H} - \frac{\alpha}{M_s} \vec{M} \times \vec{M} \times \vec{H} \right], \quad (\text{A.3.1})$$

$$\frac{\partial \vec{M}}{\partial t} = \frac{\gamma}{1+\alpha^2} \mu_0 \left\{ \vec{M} \times \vec{H} - \frac{\alpha}{M_s} [\vec{M}(\vec{M} \cdot \vec{H}) - \vec{H}(\vec{M} \cdot \vec{M})] \right\}. \quad (\text{A.3.2})$$

Since $\vec{M} \cdot \vec{M} = M^2$, then

$$\frac{\partial \vec{M}}{\partial t} = \frac{\gamma}{1+\alpha^2} \mu_0 \left\{ \vec{M} \times \vec{H} - \frac{\alpha}{M_s} [\vec{M}(\vec{M} \cdot \vec{H}) - M^2 \vec{H}] \right\}. \quad (\text{A.3.3})$$

Knowing that $\vec{H} = H_z \vec{z}$ in the z direction,

$$\frac{\partial \vec{M}}{\partial t} = \frac{\gamma}{1+\alpha^2} \mu_0 \left\{ \vec{M} \times \vec{H} - \frac{\alpha}{M_s} [\vec{M}(M_z H_z) - M^2 \vec{H}] \right\}. \quad (\text{A.3.4})$$

Considering $\vec{M} = \begin{bmatrix} M_x \\ M_y \\ M_z \end{bmatrix}$ and $\vec{H} = \begin{bmatrix} 0 \\ 0 \\ H_z \end{bmatrix}$, then we have that

$$\vec{M} \times \vec{H} = \begin{bmatrix} \vec{x} & \vec{y} & \vec{z} \\ M_x & M_y & M_z \\ 0 & 0 & H_z \end{bmatrix} = \vec{x} M_y H_z - M_x H_z \vec{y}. \quad (\text{A.3.5})$$

From (A.3.1),

$$\begin{bmatrix} \frac{\partial M_x}{\partial t} \\ \frac{\partial M_y}{\partial t} \\ \frac{\partial M_z}{\partial t} \end{bmatrix} = \frac{\gamma}{1+\alpha^2} \mu_0 \begin{bmatrix} M_y H_z \\ M_x H_z \\ 0 \end{bmatrix} - \frac{\alpha}{M} \begin{bmatrix} M_z H_z M_x \\ M_z H_z M_y \\ M_z H_z M_z \end{bmatrix} + \begin{bmatrix} 0 \\ 0 \\ \alpha M H_z \end{bmatrix}. \quad (\text{A.3.6})$$

So, in the x direction:

$$\frac{\partial M_x}{\partial t} = \frac{\gamma}{1+\alpha^2} \mu_0 \left[M_y H_z - \frac{\alpha}{M_s} M_z H_z M_x \right], \quad (\text{A.3.7})$$

in the y direction:

$$\frac{\partial M_y}{\partial t} = \frac{\gamma}{1+\alpha^2} \mu_0 \left[-M_x H_z - \frac{\alpha}{M} M_z H_z M_y \right], \quad (\text{A.3.8})$$

in the z direction:

$$\frac{\partial M_z}{\partial t} = \frac{\gamma}{1+\alpha^2} \mu_0 \left[-\frac{\alpha}{M_s} M_z^2 H_z + \alpha M H_z \right]. \quad (\text{A.3.9})$$

Isolating α ,

$$\frac{\partial M_z}{\partial t} = -\frac{\gamma\alpha}{1+\alpha^2} \mu_0 \left[\frac{M_z^2 H_z}{M_s} - M H_z \right]. \quad (\text{A.3.10})$$

Isolating M and H_z ,

$$\frac{\partial M_z}{\partial t} = -\frac{\gamma\alpha}{1+\alpha^2} \mu_0 M \left[\frac{M_z^2}{M_s^2} - 1 \right] H_z. \quad (\text{A.3.11})$$

The magnetic moment equation in the Z direction can be rewritten as:

$$\frac{\partial M_z}{\partial t} = -\frac{\gamma\alpha}{1+\alpha^2} M_s \mu_0 \left[1 - \frac{M_z^2}{M_s^2} \right] H_z. \quad (\text{A.3.12})$$

Rearranging (A.3.12),

$$\frac{\partial M_z}{\partial t} = \frac{M_s}{\frac{1+\alpha^2}{\gamma\alpha}} \mu_0 \left[1 - \frac{M_z^2}{M_s^2} \right] H_z, \quad (\text{A.3.13})$$

where $\frac{1+\alpha^2}{\gamma\alpha} = S$ is the switching constant

$$\frac{\partial M_z}{\partial t} = \frac{M_s}{S} \mu_0 \left[1 - \frac{M_z^2}{M_s^2} \right] H_z. \quad (\text{A.3.14})$$

Thus, the switching constant becomes:

$$S = \frac{1+\alpha^2}{\alpha} \gamma^{-1} = \left(\frac{1}{\alpha} + \alpha \right) \gamma^{-1}. \quad (\text{A.3.15})$$

A.4. Calculation of the Parameters of Weiner's Model

Considering a ferrite for high frequency application, $\mu_r \cong 100$ for a rise time response of 1.0 ns. See in Figure A.1 the dimensions of the model used by Weiner.

Figure A.1. Dimensions of the coaxial line used by Weiner.



Source: Author's production.

Considering the air core inductance (3.33),

$$L_0 = \frac{\mu_0}{2\pi} \ln \left(\frac{b}{a} \right) = \frac{4\pi \times 10^{-7}}{2\pi} \ln(2) = 1.38 \times 10^{-7} \cong 140.0 \text{ nH/m.} \quad (\text{A.4.1})$$

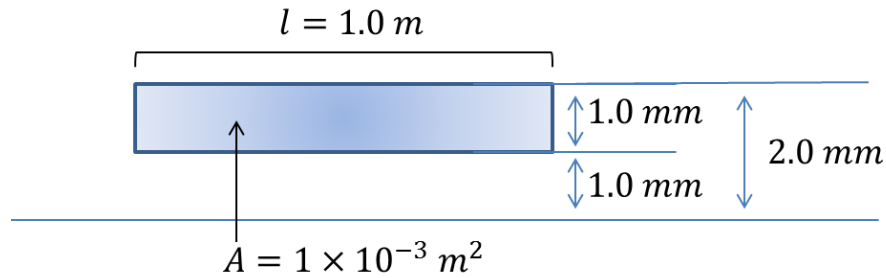
For 1.0 meter, $I_0=L_0 \times 1.0 \text{ m}=140.0 \text{ nH}$. For the ferrite with $\mu_r=100$ before saturation $I_i=\mu_r \times L_0=14.0 \mu\text{H}/\text{m}$ or $I_i=14.0 \mu\text{H}$ with 1.0 meter.

For the calculation of the flux inside the ferrite per meter, knowing that $H = \frac{I}{2\pi r}$,

$$\frac{\varphi}{l} = \int \frac{B dA}{l} = \int B dr = \int \mu H dr = \int_a^b \frac{\mu I}{2\pi r} dr = \mu_0 \mu_r \frac{I}{2\pi} \ln \left(\frac{b}{a} \right). \quad (\text{A.4.2})$$

For the calculation of the saturation current, consider $B_{sat} = 2500 \text{ Gauss} = 0.25 \text{ T}$ and the parameters of Figure A.2,

Figure A.2. Coaxial area calculation



Source: Author's production.

$$\varphi = BA = 0.25 \times 10^{-3} \text{ Weber} = I_{sat} \times 14 \times 10^{-6}, \quad (\text{A.4.3})$$

$$I_{sat} = \frac{0.25 \times 10^{-3}}{14 \times 10^{-6}} = 17.85 \text{ A.} \quad (\text{A.4.4})$$

For the linear capacitance, considering (3.40),

$$C_0 = \frac{2\pi\epsilon_0}{\ln\left(\frac{b}{a}\right)} = 80.0 \text{ pF/m.} \quad (\text{A.4.5})$$

Line discretization for a number of sections $n = 50$ and $l = 1.0 \text{ m.}$

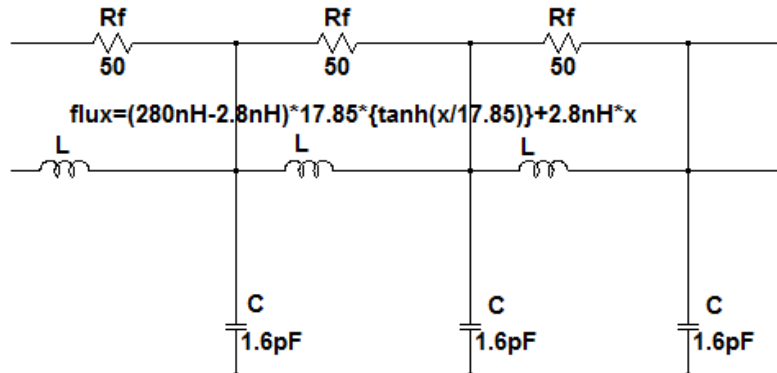
$$l'_i = \frac{L_i \times l}{N} = \frac{L_i}{N} = \frac{14 \times 10^{-6}}{50} = 280.0 \text{ nH,} \quad (\text{A.4.6})$$

$$l'_0 = \frac{L_0 \times l}{N} = \frac{L_0}{N} = 2.8 \text{ nH,} \quad (\text{A.4.7})$$

$$c'_0 = \frac{C_0 \times l}{N} = \frac{C_0}{N} = \frac{80.0 \text{ pF}}{50} = 1.6 \text{ pF.} \quad (\text{A.4.8})$$

The general schematic circuit is shown in Figure A.3.

Figure A.3. General schematic circuit used in Weiner's model.



Source: Author's production.

For the biased impedance value,

$$Z_{biased} = \sqrt{\frac{280 \text{nH}}{1.6 \text{pF}}} = 418.0 \Omega. \quad (\text{A.4.9})$$

For the pulse reduction rise time

$$\Delta T = n\sqrt{LC} - \sqrt{L_{sat}C}, \quad (\text{A.4.10})$$

$$\Delta T = 50\sqrt{280.0 \text{nH} \times 1.6 \text{pF}} - \sqrt{2.8 \text{nH} \times 1.6 \text{pF}}, \quad (\text{A.4.11})$$

$$\Delta T = 50 \times (669 \times 10^{-12} - 66.9 \times 10^{-12}) \cong 30.0 \text{ ns}. \quad (\text{A.4.12})$$

A.5. Calculation of the Parameters of the Pouladian-Kari and Shapland's Model

From the original equation used by Pouladian-Kari,

$$L = L_s[1 + \mu_r \exp(-\alpha I)]. \quad (\text{A.5.1})$$

When $I = 0$,

$$L = L_s(1 + \mu_r) = L_0 + \mu_r L_0. \quad (\text{A.5.2})$$

For $\mu_r \gg 1$, then

$$L_i \cong \mu_r L_0 = L. \quad (\text{A.5.3})$$

Considering $I \gg I_s \rightarrow L = L_s$, then the flux equation become

$$\varphi = L_s I + \mu_r L_s \int_0^I \exp(-\alpha I) dI = L_s I - \frac{\mu_r L_s}{\alpha} [1 - \exp(-\alpha I)]. \quad (\text{A.5.4})$$

Knowing that

$$\alpha = \frac{I}{I_s}, \quad (\text{A.5.5})$$

$$\varphi = L_s I + \mu_r L_s I_s \left[1 - \exp\left(-\frac{I}{I_s}\right) \right]. \quad (\text{A.5.6})$$

φ_{sat} when $I \gg I_s \rightarrow \left[1 - \exp\left(-\frac{I}{I_s}\right) \right] \approx 1$, so

$$\varphi_{sat} = L_s I + \mu_r L_s I_s = L_s (I + \mu_r I_s). \quad (\text{A.5.7})$$

For $\mu_r \gg 1$,

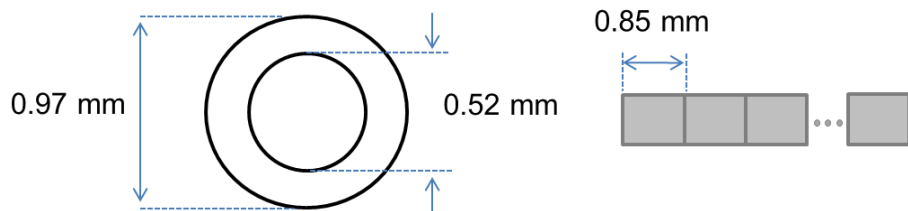
$$\varphi_{sat} \approx \mu_r L_s I_s = L_i I_s, \quad (\text{A.5.8})$$

when μ_r is small

$$\varphi_{sat} \approx L_s (1 + \mu_r) I_s. \quad (\text{A.5.9})$$

Considering the ferrite dimensions used in Pouladian-Kari's model as the values demonstrated in Figure A.4:

Figure A.4. Ferrite dimensions used in Pouladian-Kari/Shapland's model.



Source: Author's production.

Knowing from the ferrite datasheet that $\varphi_{sat} = 0.25 T$ and $\mu_r = 4$, we have:

$$\varphi_{sat} = 0.25 \times \frac{0.97 - 0.52}{2} \times 0.85 = 47.88 \times 10^{-6} \text{ Weber.} \quad (\text{A.5.10})$$

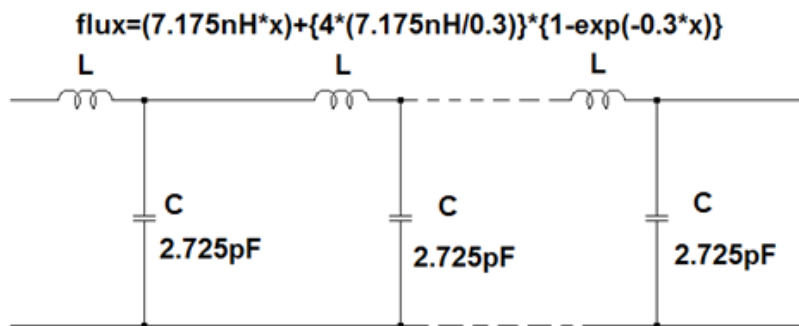
From,

$$I_s = \frac{\varphi_{sat}}{L_s(1+\mu_r)} = \frac{47.8 \times 10^{-6}}{5 \times 287 \text{ nH}} = 33 \text{ A.} \quad (\text{A.5.11})$$

From (A.5.5), considering $I_s = 33 \text{ A}$, then $\alpha = 0.03$.

For 40 sections the total values for the saturated inductance and the linear capacitance are $L_s = 287.0 \text{ nH}$ and $C = 109.0 \text{ nF}$ respectively. The general schematic circuit is shown in Figure A.5.

Figure A.5. General schematic circuit used in Pouladian-Kari/Shapland's model.



Source: Author's production.

For the biased impedance value,

$$Z_{biased} = \sqrt{\frac{287 \text{ nH}}{109 \text{ pF}}} = 170.0 \Omega. \quad (\text{A.5.12})$$

For the pulse reduction rise time

$$\Delta T = \sqrt{LC} - \sqrt{L_{sat}C}, \quad (\text{A.5.13})$$

$$\Delta T = \sqrt{287.0 \text{ nH} \times 5 \times 109.0 \text{ pF}} - \sqrt{287.0 \text{ nH} \times 109.0 \text{ pF}}, \quad (\text{A.5.14})$$

$$\Delta T = \sqrt{287.0 \text{ nH} \times 109.0 \text{ pF}} [\sqrt{5} - 1] = 5.59 \text{ ns} (1.23) = 6.87 \text{ ns}. \quad (\text{A.5.15})$$

A.6. Pouladian-Kari et al.'s Discrepancies

As observed in the previous Pouladian-Kari's results, there are certain discrepancies between the original results and the simulated ones. This can be explained since for Pouladian-Kari's analysis [14], [15], the author mentioned that the voltage across the inductor is related to the following current as:

$$v = L \frac{dI}{dt} + I \frac{dL}{dt}. \quad (\text{A.6.1})$$

From this,

$$v = L \frac{dI}{dt} + I \frac{dL}{dt} = L \frac{dI}{dt} + I \frac{dI}{dt} \frac{dL}{dI} = \frac{dI}{dt} \left(L + I \frac{dL}{dI} \right), \quad (\text{A.6.2})$$

and defining $L + I \frac{dL}{dI} = L'$, (A.6.2) is recast in the form

$$v = L' \frac{dI}{dt}. \quad (\text{A.6.3})$$

Since L decreases exponentially with I , this implies that $\frac{dL}{dI} < 0$, and thus, $I \frac{dL}{dI} < 0$, and $L' < L$.

Considering L' as the Pouladian-Kari's model inductance and L as the inductance of the reproduced model, the phase velocity in both cases become

$$v_{ph1} = \frac{1}{\sqrt{LC}} \quad (\text{A.6.4})$$

and

$$v_{ph2} = \frac{1}{\sqrt{L'C}}. \quad (\text{A.6.5})$$

As L' is smaller than L , v_{ph2} (Pouladian-Kari's) is faster than v_{ph1} (reproduced).

Another way to explain the difference between the delays is through the time delay

$$\delta_1 = n\sqrt{LC} \quad (A.6.6)$$

while Pouladian-Kari's is

$$\delta_2 = n\sqrt{L'C}. \quad (A.6.7)$$

Again, as $L' < L$, then the delay δ_1 related to the reproduced model is larger than the delay δ_2 corresponding to the original Pouladian-Kari's model.

This happens because Pouladian-Kari considered the flux relation as

$$\phi(t) = L(t) i(t), \quad (A.6.8)$$

that is, $L(t)$ is a time varying inductance, while our model considered the flux relation as

$$\phi(t) = L(i) i(t), \quad (A.6.9)$$

with the current-dependent inductance. According to [75] $\phi(t) = L(t) i(t)$ is the definition for a linear time-varying inductor, and $\phi(t) = L(i) i(t)$ is the magnetic flux linked definition with a nonlinear inductor, which is the better approach, justifying the difference between the time delays.

A.7. Calculation of the Precession Frequency at High Voltage Operation

The experiment was performed at high voltage with both axial and azimuthal bias, where V_p is the peak voltage (500 V) at the output and R_{load} (50.0 Ω) is the load resistance. According to Table 5.10 the current applied for the azimuthal bias is 0.24 A, so we have that the total current I_0 is:

$$I_0 = \frac{V_p}{R_{load}} = \frac{500 \text{ V}}{50.0 \Omega} + 0.24 \text{ A} = 10.24 \text{ A}. \quad (\text{A.7.1})$$

Knowing the values of the ferrite inner diameter (a) and ferrite outer diameter (b) from section 4.2 and considering the medium diameter of the ferrite as:

$$d_m = \frac{(a+b)}{2} = \frac{(1.93+1.09)}{2} = 1.51 \text{ mm}, \quad (\text{A.7.2})$$

the azimuthal magnetic field is:

$$H_\theta = \frac{I_0}{\pi d_m} = \frac{10.24 \text{ A}}{\pi 1.51 \times 10^{-3} \text{ m}} = 2160.33 \frac{\text{A}}{\text{m}} = 27.14 \text{ Oe}. \quad (\text{A.7.3})$$

By considering the number of turns N of the solenoid equivalent to 220 the current I_Z from Table 5.10 for the axial bias (2.10 A), and the length l of the coaxial line (20.0 cm), the axial magnetic field becomes:

$$H_Z = \frac{NI_Z}{l} = \frac{220 \text{ turns} \times 2.10 \text{ A}}{0.20 \text{ m}} = 2310.0 \frac{\text{A}}{\text{m}} = 29.02 \text{ Oe} \quad (\text{A.7.4})$$

Knowing the gyromagnetic ratio $\gamma = 28024.95 \text{ MHz/T}$ and the saturation magnetization of ferrite $M_s = 3500 \text{ gauss}$ it is possible to calculate the magnetic precession frequency as:

$$f_p = \frac{\gamma \mu_0}{4\pi} H_\theta \times \sqrt{\frac{M_s}{H_\theta^2 + H_Z^2}} = 1.4 \times 27.14 \times \sqrt{\frac{3500}{\sqrt{27.14^2 + 29.02^2}}} \cong 356.61 \text{ MHz} \quad (\text{A.7.5})$$

APPENDIX B: MATHEMATICA CODE

In this appendix the code used in Mathematica software in order to do the numerical analysis is presented.

```

Clear["Global`*"];

Number of sections

NN = 11;

Time

tmax = 6.0; (* time in ns *)

Definition of the main parameters of the line

fN = 1.0; (* Normalization factor *)

Rs = 50.0;

Resc_impar = Table[Rc[k] = 0.0, {k, 1, NN, 2}]; (* resistance in Ω *)
Resc_par = Table[Rc[k] = 0.0, {k, 2, NN, 2}]; (* resistance in Ω *)

Rc[NN]=1100.0;

Resl_impar=Table[Rl[k]=0.0,{k,1,NN,2}];(* resistance in Ω *)
Resl_par=Table[Rl[k]=0.0,{k,2,NN,2}];(* resistance in Ω *)

(*Indodd=Table[Ls[k]=2.7 * 10^3,{k,1,NN,2}];(* inductance in nH :2.7 μH*)*)
(*Indeven=Table[Ls[k]=2.7 * 10^3,{k,2,NN,2}];(* inductance in nH *)*)

(* voltage in V, resistance in Ω, current in A *)

Null;^2

Input Pulse

t0 = 0.0; ts = 1.7 + t0; tflat = 300.0; tfall = 1.7; tc = ts + tflat;
td = tc + tfall; a0 = -10.0 10^3; {ts, tflat, tfall, td - tc};

Vs[t_] := Which[t ≤ t0, 0, t > t0 && t ≤ ts, a0  $\frac{t - t_0}{ts - t_0}$ ,
                  t > ts && t ≤ tc, a0, t > tc && t ≤ td, a0  $\frac{-t + td}{td - tc}$ , t > td, 0]

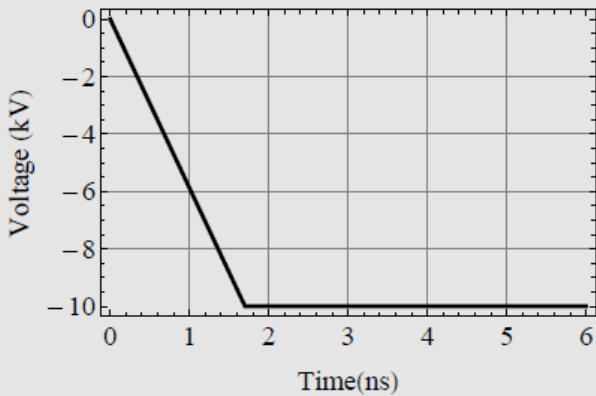
TabVs = Table[{t, Vs[t] / 1000}, {t, 0, tmax, 0.01}];

```

```

voltVs = ListPlot[TabVs, PlotRange -> All,
  PlotStyle -> {AbsoluteThickness[1.4], RGBColor[0, 0, 0], Thickness[0.008]},
  FrameLabel -> {"Time(ns)", "Voltage (kV)"}, Joined -> True,
  GridLines -> {Automatic, Automatic}, FrameTicks -> {Automatic, Automatic},
  Frame -> True, LabelStyle -> Directive[Black, 17]]

```



Fourier Transform

```

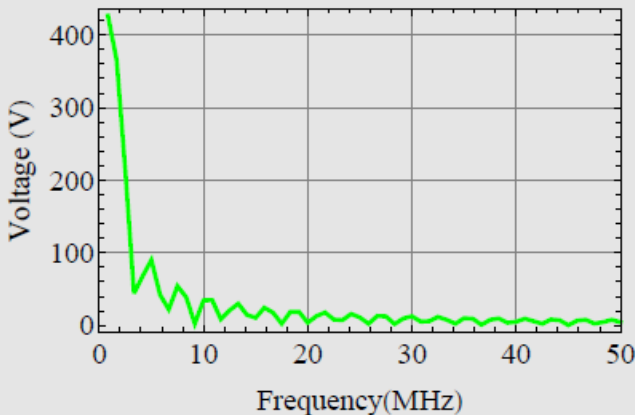
np = 256; tfourier = 1000;

pulse = Table[Vs[t] / 1000, {t, 0, tfourier, 0.05}];

datafIn = Table [{f / (1.2), Abs[Fourier[pulse]][[{f}]]}, {f, 1, 60, 1}];

pVs = ListPlot[datafIn, Joined -> True, PlotRange -> {{0, 50}, All},
  PlotStyle -> {AbsoluteThickness[1.8], RGBColor[0, 1, 0], Thickness[0.008]},
  FrameLabel -> {"Frequency(MHz)", "Voltage (V)"}, Joined -> True,
  GridLines -> {Automatic, Automatic}, FrameTicks -> {Automatic, Automatic},
  Frame -> True, LabelStyle -> Directive[Black, 17]]

```



```
NIntegrate[Vs[t] / 1000, {t, 0, 200}]
```

```
-1991.5
```

Nonlinear Capacitance

```
m = 0.0; xj = 0.7; Cs0 = 0.095 * 10^-3; (*1.6 nH x 10^-3 → pF *)
```

```
(* nonlinear capacitor *)
```

$$Cv[k_][t_] := \text{Which} [v[k][t] > -xj, \frac{Cs0}{\left(1.0 + 1 * \frac{v[k][t]}{xj}\right)^m}, v[k][t] \leq -xj, 10.0];$$

```
(* LINEAR CAPACITOR: m = 0 *)
```

$$Cv[k_][t_] := \frac{Cs0}{\left(1.0 + 1 * \frac{v[k][t]}{xj}\right)^m}$$

$$Ca[Va_] = \frac{Cs0}{\left(1.0 + 1 * \frac{Va}{xj}\right)^m}$$

```
0.000095
```

```
Cv[NN][t] := 10 000 000.0;
```

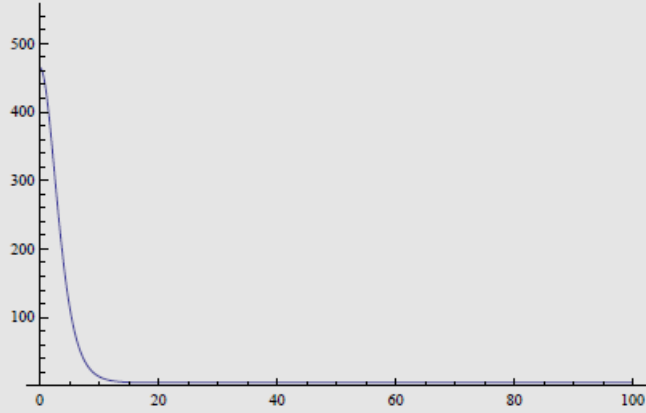
Nonlinear Inductance

```
L0 = 465.0; La = 4.65; Is = 3.76; (*Inductance in nH; Current in A*)
```

$$Ls[k_][t_] := (L0 - La) \left(\text{Sech} \left[\frac{i[k][t]}{Is} \right]^2 \right) + La$$

$$La1[Ia_] := (L0 - La) \left(\text{Sech} \left[\left(\frac{Ia}{Is} \right)^2 \right] + La \right)$$

```
Plot[{La1[Ia]}, {Ia, 0, 100}, PlotRange → {0, L0 * 1.2}]
```



```
Ls[NN][t] := 1.0 × 10^-8
```

```
Ls[k_][t_] := 280.0
```

Equation for the First Section

```
eqi = Table[ {i[k]'[t] == vs[t]/ls[k][t] - rs/ls[k][t]*i[k][t] - 
    rc[k]/ls[k][t]*(i[k][t] - i[k+1][t]) - (v[k][t])/ls[k][t] - rl[k]/ls[k][t]*i[k][t], 
    v[k]'[t] == (i[k][t] - i[k+1][t])/cv[k][t]}, {k, 1, 1}];
```

Equation for the intermediate sections

```
eqs = Table[ {i[k]'[t] == rc[k-1]/ls[k][t]*(i[k-1][t] - i[k][t]) + (v[k-1][t])/ls[k][t] - 
    rc[k]/ls[k][t]*(i[k][t] - i[k+1][t]) - (v[k][t])/ls[k][t] - rl[k]/ls[k][t]*i[k][t], 
    v[k]'[t] == (i[k][t] - i[k+1][t])/cv[k][t]}, {k, 2, nn-1}];
```

Equation for the last section

```
eqf = Table[ {i[k]'[t] == 
    rc[k-1]/ls[k][t]*(i[k-1][t] - i[k][t]) + (v[k-1][t])/ls[k][t] - rc[k]/ls[k][t]*(i[k][t]) - 
    (v[k][t])/ls[k][t] - rl[k]/ls[k][t]*i[k][t], v[k]'[t] == (i[k][t])/cv[k][t]}, {k, nn, nn}];
```

```
eqparcial = Join[eqi, eqs, eqf];
```

```
eqfinal = Flatten[eqparcial];
```

Initial condition and solution of the equations

```
initial1 = Flatten[Table[{i[k][0] == 0., v[k][0] == 0.}, {k, 1, nn}]];
```

```
vlist = Flatten[Table[{v[k][t], i[k][t]}, {k, 1, nn}]];
```

```
sol = NDSolve[Join[eqfinal, initial1],
  vlist, {t, 0., tmax}, MaxSteps → Infinity];
```

```
soll = Flatten[sol];
```

```
inputiv =
  Table[{i[k][t_] = i[k][t] // . soll, v[k][t_] = v[k][t] // . soll}, {k, 1, nn}];
```

```
outiv = Flatten[inputiv];
```

```
v[0][t_] := vs[t] - rs i[1][t]
```

```

vfp = Table[v[k][t_] = Rc[k] * (i[k][t] - i[k + 1][t]) + v[k][t], {k, 1, NN - 1}];

V[NN][t_] := Rc[NN] * (i[NN][t]) + v[NN][t]

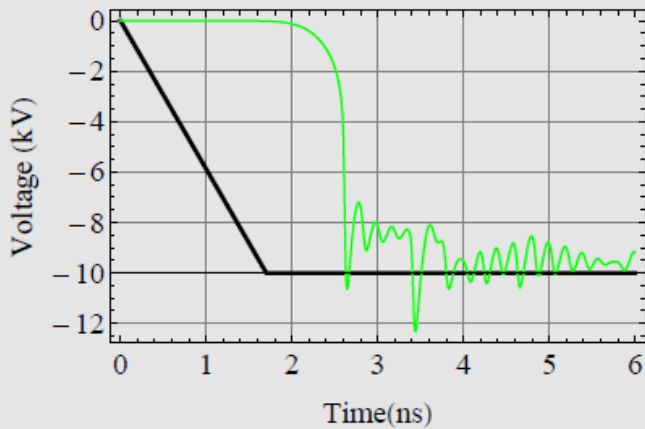
Pload[t_] := V[NN][t] i[NN][t]

Pin[t_] := Vs[t] i[1][t]

```

Results

```
Show [voltVs, voltFim]
```



APPENDIX C: PUBLISHED WORKS AND PARTICIPATION IN EVENTS

In this appendix are pointed the contents presented in conferences, workshops, symposiums and also published in Journals by reverse chronological order, addressing the work developed during this D.Sc. thesis. The works marked with * were presented by the student.

C.1. Journals

IEEE Transactions on Plasma Science

Special Issue - Pulsed Power Science & Technology - 2016

YAMASAKI, F. S.; SCHAMILOGLU, E. ; J.O. Rossi; BARROSO, J. J.
Simulation Studies of Distributed Nonlinear Gyromagnetic Lines Based on LC Lumped Model. In: IEEE Transactions on Plasma Science, v.44, Issue 10, pp.2232-2239, Oct. 2016. DOI: 10.1109/TPS.2016.2556320

IEEE Transactions on Plasma Science

Special Issue - Pulsed Power Science & Technology - 2016

RANGEL, E.G.L.; BARROSO, J.J.; J.O. ROSSI **YAMASAKI, F.S. ; SILVA NETO, L.P.; SCHAMILOGLU, E.**; Influence of Input Pulse Shape on RF Generation in Nonlinear Transmission Lines. In: IEEE Transactions on Plasma Science, v. 44, Issue 10, pp. 2258-2267, Oct. 2016. DOI: 10.1109/TPS.2016.2593606

IEEE Transactions on Plasma Science - 2014

YAMASAKI, F. S.; SILVA NETO, LAURO P.; ROSSI, JOSE O.; BARROSO, JOAQUIM J.; Soliton Generation Using Nonlinear Transmission Lines. In: IEEE Transactions on Plasma Science, V. 42, Issue 11, pp. 3471-3477, 2014. DOI: 10.1109/TPS.2014.2361487

C.2. International Conferences

6th Euro-Asian Pulsed Power Conference – EAPPC 2016

YAMASAKI, F.S.; ROSSI, J.O.; BARROSO, J.J.; and SCHAMILOGLU, E.; Analysis of a gyromagnetic nonlinear transmission line based on experimental results. In: Euro-Asian Pulsed Power Conference (EAPPC), 2016, Estoril, Portugal.

6th Euro-Asian Pulsed Power Conference – EAPPC 2016

RANGEL, E.G.L.; ROSSI, J.O.; BARROSO, J.J.; **YAMASAKI, F.S.**; SILVA NETO, L.P.; and SCHAMILOGLU, E.; Analysis of RF Generation Using NLTLs Driven by Pump Input Pulses of Different Shapes. In: Euro-Asian Pulsed Power Conference (EAPPC), 2016, Estoril, Portugal.

XVIII Simpósio de Aplicações Operacionais em Áreas de Defesa – SIGE 2016

ROSSI, J.O.; SILVA NETO, L.P.; **YAMASAKI, F.S.**; BARROSO, J.J.; RANGEL, E.G.L. and SCHAMILOGLU, E.; High-Voltage Soliton Generation with Nonlinear Lumped Varactor Diode Lines. In: 18º Simpósio de Aplicações Operacionais em Áreas de Defesa (SIGE), 2016, São José dos Campos, Brazil.

International Microwave and Optoelectronics Conference – IMOC 2015

* **YAMASAKI, F. S.** ; SCHAMILOGLU, E. ; J.O. ROSSI ; BARROSO, J. J. . Spice Simulations of Inductive Nonlinear Transmission Lines. In: International Microwave and Optoelectronics Conference (IMOC), 2015, Porto de Galinhas, Brazil.

20th IEEE Pulsed Power Conference – PPC 2015

* **YAMASAKI, F. S.** ; SCHAMILOGLU, E. ; ROSSI, J. O. ; BARROSO, J. J. . Spice simulations of nonlinear gyromagnetic lines. In: IEEE Pulsed Power Conference (PPC), 2015, Austin, USA.

20th IEEE Pulsed Power Conference – PPC 2015

* ROSSI, J. O. ; SILVA, L. P. ; BARROSO, J. J. ; **YAMASAKI, F. S.** ; SCHAMILOGLU, EDL . Overview of RF generation using nonlinear transmission lines. In: IEEE Pulsed Power Conference (PPC), 2015, Austin, USA.

XVI Simpósio de Aplicações Operacionais em Áreas de Defesa – SIGE

2014

SILVA NETO, LAURO P.; ROSSI, JOSE O.; BARROSO, JOAQUIM J.; **YAMASAKI, FERNANDA S.**; RF pulse formation in NLTLs using varactor diode. In: XVI Simpósio de Aplicações Operacionais em Áreas de Defesa (SIGE), 2014, São José dos Campos, Brazil.

International Microwave and Optoelectronics Conference – IMOC 2013

* **YAMASAKI, FERNANDA S.**; ROSSI, JOSE O.; BARROSO, JOAQUIM J.; RF Generation using Nonlinear Transmission Lines for Aerospace Applications. In International Microwave and Optoelectronics Conference (IMOC), 2013, Rio de Janeiro, Brazil.

International Microwave and Optoelectronics Conference – IMOC 2013

ROSSI, JOSE O.; SILVA NETO, LAURO P.; **YAMASAKI, FERNANDA S.**; BARROSO, JOAQUIM J. State of the art of nonlinear transmission lines for applications in high power microwaves. In International Microwave and Optoelectronics Conference (IMOC), 2013, Rio de Janeiro, Brazil.

19th IEEE Pulsed Power Conference - PPC 2013

ROSSI, J.O.; SCHAMILOGLU, E. ; KUEK, N. S. ; **YAMASAKI, F. S.** . Design Considerations in Lossy Dielectric Nonlinear Transmission Lines. In: IEEE Pulsed Power Conference (PPC), 2013, San Francisco, USA.

C.3. National Conferences

17º SBMO - Simpósio Brasileiro de Micro-ondas e Optoeletrônica e 12º

CBMag - Congresso Brasileiro de Eletromagnetismo – MOMAG 2016

* **YAMASAKI, F.S.** ; ROSSI, J.O. ; BARROSO, J.J. ; SCHAMILOGLU, E.; Simulação de Linhas Não Lineares Giromagnéticas. In: 17º SBMO - Simpósio Brasileiro de Micro-ondas e Optoeletrônica e 12º CBMag - Congresso Brasileiro de Eletromagnetismo (MOMAG), 2016, Porto Alegre, Brazil.

V Workshop em Engenharia e Tecnologia Espaciais – WETE 2014

SILVA NETO, L.P.; ROSSI, J.O.; **YAMASAKI, F. S.** ; BARROSO, J. J. . Análise do comportamento de uma LTNL em baixa tensão. In: Workshop em Engenharia e Tecnologia Espaciais (WETE), 2014, São José dos Campos, Brazil.

**16º SBMO - Simpósio Brasileiro de Micro-ondas e Optoeletrônica e 11º
CBMag - Congresso Brasileiro de Eletromagnetismo – MOMAG 2014**

* **YAMASAKI, F. S.** ; J.O. Rossi ; BARROSO, J. J. ; SILVA NETO, L. P. . Geração de RF Usando Linhas de Transmissão Não Lineares. In: 16º SBMO - Simpósio Brasileiro de Micro-ondas e Optoeletrônica e 11º CBMag - Congresso Brasileiro de Eletromagnetismo (MOMAG), 2014, Curitiba, Brazil.

IV Workshop em Engenharia e Tecnologia Espaciais – WETE 2013

* **YAMASAKI, F. S.** ; J.O. Rossi ; BARROSO, J. J. . Study of Nonlinear Lumped Element Transmission Lines for RF Generation. In: Workshop em Engenharia e Tecnologia Espaciais (WETE), 2013, São José dos Campos, Brazil.

The resulting scientific contribution of this doctoral thesis is presented in Table B.1, which is divided in chronological order in the columns and in types of divulgence in the lines (Journals, International Conferences and National Conferences), with a total of 17 works.

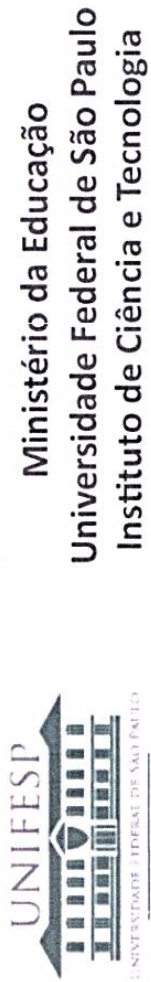
Table C.1. Summary of the works published and presented at conferences during the development of this thesis.

| | 2013 | 2014 | 2015 | 2016 | TOTAL |
|----------------------------------|-------------|-------------|-------------|-------------|--------------|
| Journals | | 1 | | 2 | 3 |
| International Conferences | 3 | | 3 | 3 | 10 |
| National Conferences | 1 | | | 1 | 4 |
| TOTAL | 4 | 4 | 3 | 6 | 17 |

Source: Author's production.

APPENDIX D: TEACHING INTERNSHIP

Teaching internship accomplished according to the Capes exigency (120 hours) in the São Paulo Federal University (UNIFESP), under supervision of the Professor Doctor Tiago de Oliveira, in the following disciplines:



CERTIFICADO

Certifico que Fernanda Sayuri Yamasaki, participou do Projeto de Tutoria Acadêmica INPE/UNIFESP durante o 1º semestre de 2014 com carga horária total de 60 horas, juntamente à disciplina Circuitos Digitais, sob a supervisão do Prof. Dr. Tiago de Oliveira.

São José dos Campos, 2 de outubro de 2014.

A handwritten signature in black ink, which appears to read 'Anderson Garbuglio de Oliveira'.

Prof. Dr. Anderson Garbuglio de Oliveira
Coordenador da Comissão de Monitoria

A handwritten signature in black ink, which appears to read 'Luiz Leduíno de Sáles Neto'.

Prof. Dr. Luiz Leduíno de Sáles Neto
Diretor Acadêmico



Ministério da Educação
Universidade Federal de São Paulo
Instituto de Ciência e Tecnologia

CERTIFICADO

Certifico que **Fernanda Sayuri Yamasaki**, participou do Projeto de Tutoria Acadêmica INPE/UNIFESP durante o 2º semestre de 2014 com carga horária total de 60 horas, juntamente à disciplina Laboratório de Sistemas Computacionais: Circuitos Digitais, sob a supervisão do Prof. Dr. Tiago de Oliveira.

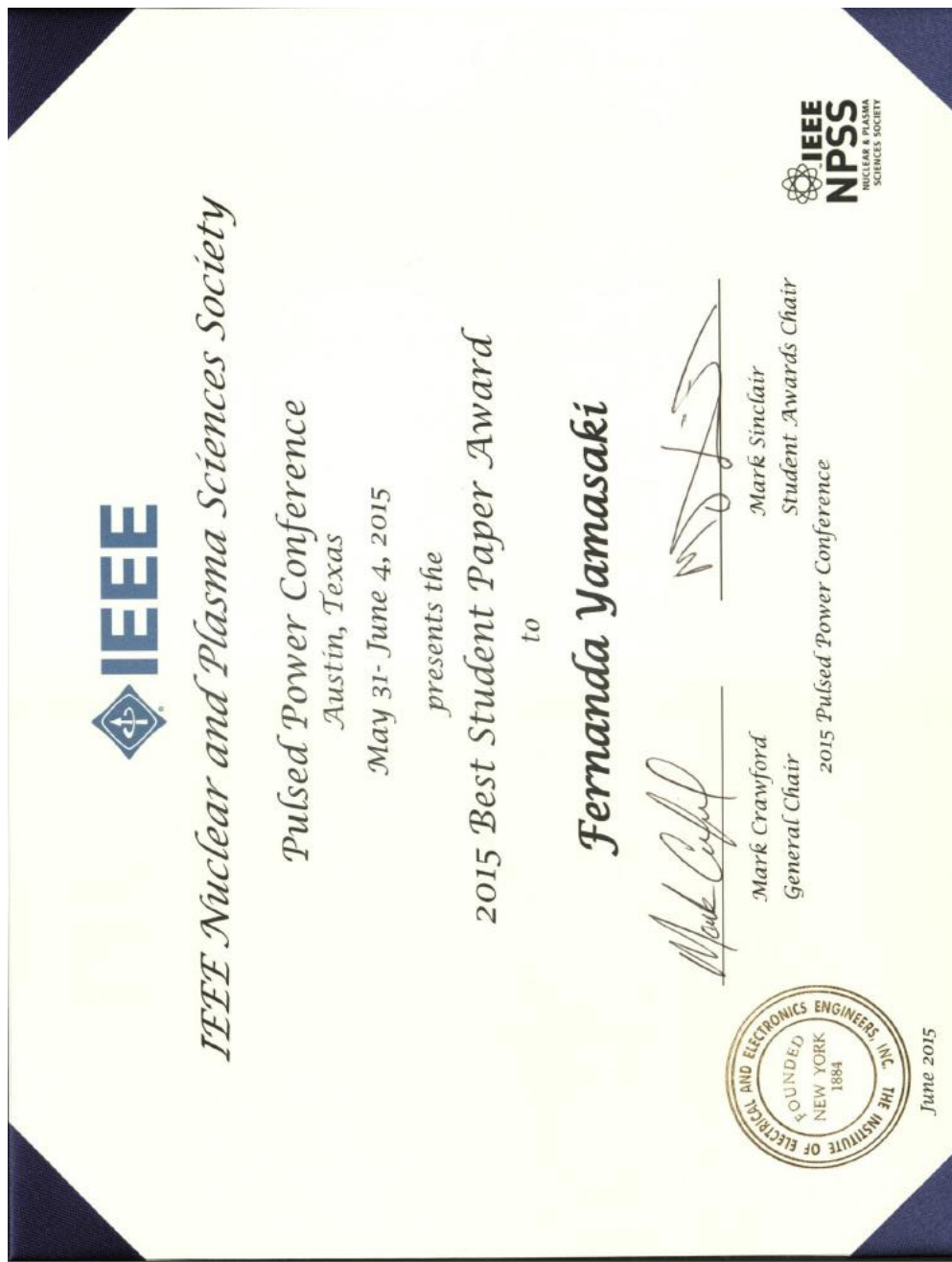
São José dos Campos, 15 de dezembro de 2014.

Prof. Dr. Anderson Garbuglio de Oliveira
Coordenador da Comissão de Monitoria

Prof. Dr. Luiz Leduíno de Salles Neto
Diretor Acadêmico

APPENDIX E: AWARD

During the D.Sc. Program, the student received the “2015 Best Student Paper Award” conferred by the “IEEE Nuclear and Plasma Sciences Society” during the “2015 Pulsed Power Conference” event, that happened from May 31st to June 4th, 2015, in Austin, Texas, United States of America.



APPENDIX F: SANDWICH PROGRAM

During the period of 2015 February to August, Ms. Fernanda Yamasaki spent 6 months as a graduate student in a Sandwich Program in the Department of Electrical and Computing Engineering at the University of New Mexico (UNM). During this period she worked with Spice simulations of gyromagnetic nonlinear transmission lines, supervised by Professor Dr. Edl Schamiloglu who is the head of an active program on high power microwave devices for RF generation in space applications, including nonlinear transmission lines. Her sandwich program was supported by a scholarship provided by the Brazilian Agency CAPES (Coordination for the Improvement of Higher Level Personnel).



APPENDIX G: PROJECT SUPPORTERS



ANNEX A: MAIN DATASHEETS

In this appendix there will be presented the most important datasheets used during this thesis that make possible the gyromagnetic line design and tests.

A.1. Ferrite bead FB-43201

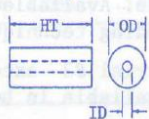
| Ferrite Shielding Beads | | | | | | | | | |
|-------------------------|-----------|---------------------|------|-------|-------------------------------------|------|------|------|-------------------|
| Part number | Bead type | Dimensions (inches) | | | A_L of Materials (mh/1000 turns) | | | | Impedance factor* |
| | | OD | ID | Hgt | 43 | 64 | 73 | 75 | |
| FB-(--)-101 | 1 | .138 | .051 | .128 | 510 | 150 | 1500 | 3000 | ---- |
| FB-(--)-201 | 1 | .076 | .043 | .150 | 360 | 110 | 1100 | ---- | 0.70 |
| FB-(--)-301 | 1 | .138 | .051 | .236 | 1020 | 300 | 3000 | ---- | 2.00 |
| FB-(--)-801 | 1 | .296 | .094 | .297 | 1300 | 390 | 3900 | ---- | 2.60 |
| FB-(64)-901 | 2 | .250 | .050 | .417 | ---- | 1130 | ---- | ---- | 7.50 ** |
| FB-(--)-1801 | 1 | .200 | .062 | .437 | 2000 | 590 | 5900 | ---- | 3.90 |
| FB-(--)-2401 | 1 | .380 | .197 | .190 | 520 | ---- | 1530 | ---- | 1.02 |
| FB-(--)-5111 | 3 | .236 | .032 | .394 | 3540 | 1010 | ---- | ---- | 6.70 *** |
| FB-(--)-5621 | 1 | .562 | .250 | 1.125 | 3800 | ---- | ---- | ---- | 6.40 |
| FB-(--)-6301 | 1 | .375 | .194 | .410 | 1100 | ---- | ---- | ---- | 2600 |
| FB-(43)-1020 | 1 | 1.000 | .500 | 1.112 | 3200 | ---- | ---- | ---- | 6.20 |
| FB-(77)-1024 | 1 | 1.000 | .500 | .825 | ---- | ---- | ---- | 5600 | 3.70 |
| 2X-(43)-151 | 4 | 1.020 | .500 | 1.125 | Split bead, 43 Mat. Z=159 @ 25 MHz. | | | | Z=245 @ 100 MHz |
| 2X-(43)-251 | 4 | .590 | .250 | 1.125 | Split bead, 43 mat. Z=171 @ 25 Mhz. | | | | Z=275 @ 100 MHz |

Notes: Complete the part number by adding material number in space (--) provided.

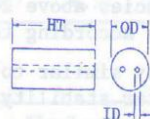
A_L values based on low frequency measurements. (mh/1000 turns) = nanohenries/turns²

** Based on a single 'U-turn' winding. *** Based on a 2 1/2 turn, side to side winding.

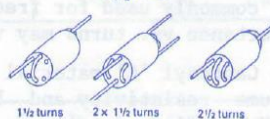
Type 1



Type 2



Type 3

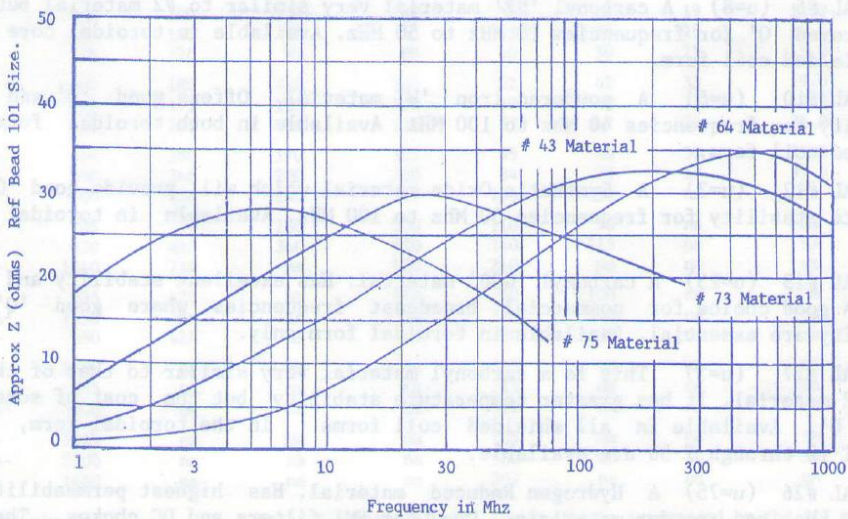


Type 4



Material vs Frequency vs Impedance

* Impedance Factor: This chart is based upon the '101' size bead. Impedances for other size beads may be approximated as follows: Find the 'Z' of the same material at your operating frequency in the chart below. Multiply that 'Z' by the Impedance Factor shown above.



A.2. Diode BYW56

Philips Semiconductors

Product specification

Controlled avalanche rectifiers

BYW54 to BYW56

FEATURES

- Glass passivated
- High maximum operating temperature
- Low leakage current
- Excellent stability
- Guaranteed avalanche energy absorption capability
- Available in ammo-pack.

DESCRIPTION

Rugged glass package, using a high temperature alloyed construction.

This package is hermetically sealed and fatigue free as coefficients of expansion of all used parts are matched.

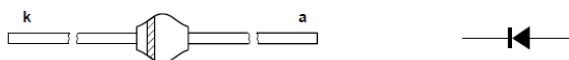


Fig.1 Simplified outline (SOD57) and symbol.

LIMITING VALUES

In accordance with the Absolute Maximum Rating System (IEC 134).

| SYMBOL | PARAMETER | CONDITIONS | MIN. | MAX. | UNIT |
|-------------|----------------------------------------------|-----------------------------------------------------------------------------------------------------------|------|------|------|
| V_{RRM} | repetitive peak reverse voltage | | – | 600 | V |
| | BYW54 | | | 800 | V |
| | BYW55 | | | 1000 | V |
| V_{RWM} | crest working reverse voltage | | – | 600 | V |
| | BYW54 | | | 800 | V |
| | BYW55 | | | 1000 | V |
| V_R | continuous reverse voltage | | – | 600 | V |
| | BYW54 | | | 800 | V |
| | BYW55 | | | 1000 | V |
| $I_{F(AV)}$ | average forward current | $T_{tp} = 45^\circ\text{C}$; lead length = 10 mm; averaged over any 20 ms period; see Figs 2 and 4 | – | 2.0 | A |
| | | $T_{amb} = 80^\circ\text{C}$; PCB mounting (see Fig.9); averaged over any 20 ms period; see Figs 3 and 4 | – | 0.8 | A |
| I_{FSM} | non-repetitive peak forward current | $t = 10$ ms half sinewave | – | 50 | A |
| E_{RSM} | non-repetitive peak reverse avalanche energy | $L = 120$ mH; $T_j = T_{j\max}$ prior to surge; inductive load switched off | – | 20 | mJ |
| T_{stg} | storage temperature | | -65 | +175 | °C |
| T_j | junction temperature | see Fig.5 | -65 | +175 | °C |